# “Enhancing PARP inhibition mediated DNA Damage and leveraging inherent anti-apoptotic dependencies in acute myeloid leukemia”

**Dissertation**

zur Erlangung des Grades

Doktor der Naturwissenschaften

Am Fachbereich Biologie

der Johannes-Gutenberg-Universität Mainz

vorgelegt von

**Viral Virendra Shah**

geb. am 16.10.1989 in Mumbai, Indien

Mainz, 2020

Tag der mündlichen Prüfung: 30th Oktober, 2020

# 1. Summary

The Poly (ADP-ribose) polymerase protein family plays an important role in genome maintenance, with a major function in the correction of single strand breaks (SSB) via the base excision repair pathway. The significance of PARP inhibition and its potential for achieving synthetic lethality have been extensively characterized for cancers with germline *BRCA* mutations. The knowledge incurred from these cancer models has already been applied to various other cancer models such as glioblastoma, prostrate, and ovarian cancers. Although BRCA mutations are not amongst the major cluster of driver mutations, some reports have shown a hypermethylation of BRCA in acute myeloid leukemia (AML) patient samples suggesting dysfunctional DNA repair remains an untapped territory in targeting vulnerabilities of cancer cells.

AML is characterized by an increased cell proliferation, blocked differentiation, and aberrant self-renewal capabilities. In this project, we raised the hypothesis that further induction of replicative stress / DNA damage mediated by PARP inhibition in already highly proliferating cells potentiates the dependency on anti-apoptotic proteins and that a specific inhibition of anti-apoptotic pathways will cause cell death.

Preliminary data showed that mono-treatment with a PARP 1/2 inhibitor (Olaparib) induced a dose- and time dependent accumulation of gH2AX foci. Olaparib neither affected the survival of the cells nor cell cycle progression. We next investigated if the damage was cell cycle specific. To this end, we used high-content screening approach quantifying the DNA damage within each phase of the cell cycle. DNA damage accumulation was elevated in S/G2 phase, but cells managed to overcome this stress and continued cycling. Interestingly, the increase in DNA damage was accompanied by a dose-dependent increase in the anti-apoptotic protein B-cell lymphoma 2 (BCL2). We performed unsupervised hierarchal clustering of endogenous transcriptomic profiles of genes involved in DNA damage response pathways of various AML cell lines with distinct genetic background and correlated these profiles with the mutational status of major regulators of DNA damage. We observed that cell lines with wild type (wt) TP53 expression clustered together, and a subgroup of the cluster had FLT3 mutations.

Consistently, when we combined PARP inhibition together with BCL2 inhibitor (Venetoclax) in a *TP53*$^{wt}$ *FLT3*$^{mut}$ background, cells underwent synergistic apoptotic death. Of note, although the combined treatment was most effective in cells with low or even undetectable BRCA1 or BRCA2 protein expression, cell lines with BRCA1 and BRCA2 expression also showed promising responses.

Our data indicate that inhibition of DNA damage repair in combination with inhibition of antiapoptotic pathways may provide a novel treatment strategy in highly proliferative cancers.

# 2. Zusammenfassung

Die Proteinfamilie der Poly(ADP-Ribose)-Polymerasen spielt eine wichtige Rolle in der Aufrechterhaltung der genomischen Integrität. Eine Hauptfunktion der Mitglieder dieser Familie liegt in der Reparatur von Einzelstrangbrüchen (SSB) mittels Basenexzisionsreparatur (BER).

Die Bedeutung der PARP-Hemmung zur Induktion synthetischer Letalität wurde erstmals für Patienten mit Mammakarzinom mit Keimbahnmutationen in den BRCA-Genen bzw. für HER2-negative Mas gezeigt. Die in diesen Krebsmodellen gewonnenen Erkenntnisse wurden bereits erfolgreich auf andere Tumorentitäten, wie z.B. Glioblastome, Prostatakarzinom sowie Eierstockkrebs übertragen. Obwohl BRCA-Mutationen nicht zu den hauptursächlichen Treibermutationen in der akuten myeloischen Leukämie (AML) gehören, wurde bei einigen Patienten eine Hypermethylierung der BRCA-Gene beschrieben. Dies legt den Schluss nahe, dass es bei diesen Patienten zu einer Deregulation der DNA-Reparatur (DDR) kommen kann. Dies eröffnet neue, bisher nicht angewandte Therapieoptionen in der Behandlung der AML.

Die AML ist charakterisiert durch eine erhöhte Proliferationsrate, sowie einen Differenzierungsblock und der deregulierten Fähigkeit zur Selbsterneuerung myeloischer Zellen. In dieser Arbeit stellen wir daher die Frage, inwieweit eine weitere Erhöhung des replikativen Stresses sowie der DNA-Schäden durch PARP Inhibition in bereits stark proliferierenden Zellen die Anhängigkeit dieser von anti-apoptotischen Proteinen erhöht. Des Weiteren wollen wir feststellen, ob spezifische Inhibition von anti-apoptotischen Signalwegen Zelltod auslösen kann.

Erste Daten haben gezeigt, dass die Monobehandlung mit dem PARP1/2 Inhibitor Olaparib eine dosis- und zeitabhängige Anhäufung von gH2AX-Foci zu dem Folgen hat. Olaparib hat keinen Effekt auf das Überleben der Zellen sowie den Zellzyklus. Im Weiteren stellten wir die Frage, ob die DNA-Schädigung zellzyklusspezifisch ist. Zu diesem Zweck verwendeten wir „High-content screening“ um die DNA-Schädigung zellzyklusabhängig zu quantifizieren. Wir konnten eine Akkumulation der DNA-Schäden in der S/G2-Phase beobachten; diese Schädigung konnte allerdings von den Zellen

überwunden und eine Rückkehr zum normalen Zellzyklus beobachtet werden. Interessanterweise wurden erhöhte DNA-Schäden von einer erhöhten, dosis-abhängigen Expression des anti-apoptotischen Proteins „protein B-cell lymphoma 2“ (BCL2) begleitet. Wir haben „Unsupervised Hierarchal-clustering von endogenen Transkriptomprofilen verschiedener, in der DDR involvierten Gene mehrerer AML Zelllinien durchgeführt, die sich durch verschiedene genetische Hintergründe auszeichnen. Anschließend wurden die jeweiligen Profile mit dem Mutationsstatus verschiedener DDR-Regulatorgene korreliert. Wir konnten zeigen, dass Zelllinien mit wildtypischem (wt) TP53 ein Cluster bilden, sowie auch Zellen mit FLT3-Mutation eine Untergruppe. Wurden Zellen mit TP53wt FLT3mut Status mit einer Kombinationstherapie aus PARP-Inhibitor und BCL2-Inhibitor (Venetoclax) behandelt, konnte in dieser Apoptose ausgelöst werden. Dieser Zelltod basierte auf der synergistischen Wirkung beider Inhibitoren. Von Interesse ist die Tatsache, dass, obwohl die Kombinationsbehandlung am effektivsten in Zellen mit geringer oder keiner BRCA1 oder BRCA2 Expression waren, auch in Zellen mit BRCA1 oder BRCA2 Expression vielversprechende Ergebnisse gewonnen werden konnten.

Unsere Daten zeigen, dass die gezielte Inhibition von DANN-Reparaturwegen in Kombination mit der Hemmung von anti-apoptototischen Signalwegen eine neue Therapieoption in hochproliferativen Krebszellen darstellen kann. Derzeit untersuchen wir die kombinatorischen Effekte dieser Therapie in primären AML Proben und beschäftigen uns mit den Mechanismen mittels derer AML Zellen DANN-Schäden begegnen.

# 3. List of abbreviations

| | |
|---|---|
| % (v/v) | Percentage by volume |
| % (w/v) | Percentage by weight |
| 53BP1 | p53 binding protein 1 |
| 7-AAD | 7-Aminoactinomycin D |
| A. dest | distilled water |
| AIF | Apoptosis inducing factor |
| AKT/PKB | Protein kinase B |
| alt-NHEJ | Alternative non-homologous end joining |
| AML | Acute myeloid leukemia |
| APS | Ammonium persulfate |
| ATCC | American Type Culture Collection |
| ATM | Ataxia teleangiectasia mutated |
| ATP | Adenosine triphosphate |
| ATR | Ataxia teleangiectasia and RAD3 related |
| ATRA | All-trans retinoic acid |
| BAK | Bcl-2 homologous antagonist/killer |
| BAX | Bcl-2-associated X protein |
| BER | Base excision repair |
| BLISS | Bliss independence model |
| BM | bone marrow |
| BRCA | Breast cancer |
| BSA | Bovine serum albumin |
| CBP | CREB-binding protein |
| CCLE | Cancer Cell Line Encyclopedia |
| CD11b | Cluster of differentiation 11 b |
| CDK | Cyclin dependent kinase |
| CLP | common lymphoid progenitor |
| CMP | common myeloid progenitor |
| cNHEJ | classical Non-homologous end joining |
| COSMIC | Catalogue of Somatic Mutation in Cancer |
| DAPI | 4',6-Diamidino-2-phenylindole |
| DMSO | Dimethylsulfoxide |
| DNA | Desoxyribonucleic acid |
| DNA-PK | DNA-dependent protein kinase |
| DNA-PK | DNA dependent protein kinases |
| DSB | Double strand break |
| DSB | double strand break |
| DSMZ | German Cancer Cell Line Depository |
| ECL | Enhanced chemiluminescence |
| EDTA | Ethylenediaminetetraacetic acid |

| | |
|---|---|
| ELP | early lymphoid progenitor |
| FACS | Fluorescence-activated cell sorting |
| FBS | Fetal bovine serum |
| FLT3 | FMS-like tyrosine kinase 3 |
| FSC | Forward scatter |
| g | Gram |
| HCS | High content screening |
| HPC | hematopoietic progenitor cell |
| HR | Homology based recombination |
| hr | Hour |
| HSA | Highest single agent |
| HSC | hematopoietic stem cell |
| HSCT | Allogenic hematopoietic stem cell transplantation |
| HTS | High throughput screening |
| ITD | Internal tandem duplication |
| L-Glu | L-Glutamine |
| LIG3 | DNA Ligase 3 |
| LMPP | lymphoid-primed multipotent progenitor |
| MDM2 | Murine double minute 2 |
| MDM2 | Murine double minute 2 |
| MEK | MAP-kinase-ERK-kinase |
| min | minute |
| MLL | Mixed lineage leukemia |
| MPP | multipotent progenitor |
| MRE11 | Meiotic recombination 11 |
| MRE11 | meiotic recombination 11 |
| mTOR | Mechanistic Target of Rapamycin |
| MTT | 3-(4,5-dimethylthiazol-2-yl)-2,5-diphenyltetrazolium bromide |
| NAD+ | Nicotinamide adenine dinucleotide |
| NBS | Nijmegen breakage syndrome protein 1 |
| NER | Nucleotide excision repair |
| NHEJ | Non-homologous end joining |
| NPM1 | Nucleophosmin |
| Ola | Olaparib |
| p53mut | Mutated p53 |
| p53wt | Wild type p53 |
| PAGE | Polyacrylamide gel electrophoresis |
| PAR | Poly-ADP ribose |
| PAR | poly(ADP-ribose) chains |
| PARG | poly(ADP-ribose) glycohydrolase |
| PARP | poly(ADP-ribose) polymerase |

| | |
|---|---|
| PBS | Phosphate-buffered saline |
| PBST | PBS-Tween20 |
| PCNA | Proliferating cell nuclear antigen |
| PFA | Paraformaldehyde |
| pH | Potentia hydrogenii |
| PI | Propidium iodide |
| PI3K | Phosphatidyl-inositide 3 kinase |
| pRPA | phospho-replication protein A |
| PUMA | P53 upregulated modulator of apoptosis |
| RING | Really interesting new gene |
| ROS | Reactive oxygen species |
| RPA | replication protein A |
| rpm | Rounds per minute |
| RT | Room temperature |
| SDS | Sodium dodecyl sulfate |
| SIRT1 | Sirtuin-1 |
| SSB | Single strand break |
| SSC | Side scatter |
| TEMED | N,N,N',N'-Tetramethylethane-1,2-diamine |
| TKD | Tyrosine kinase domain |
| TKD | tyrosine kinase domain |
| Tris | Tris(hydroxymethyl)aminomethane |
| UV | Ultraviolet |
| WHO | World health organization |
| XRCC1 | X-ray repair cross-complementing protein 1 |
| XRCC4 | Xray repair cross-complementing protein 4 |
| ZIP | zero interaction potency |
| γH2AX/gH2AX | Phospho-histone 2AX |

# Table of Contents

# 4. Introduction

## 4.1 Hematopoiesis

Hematopoiesis is the process in which cellular components of blood are constantly being replaced and replenished with newer cells. Blood constitutes of various cell types with distinct and specialized functions, from oxygen transport to immune response (Pelayo, Dorantes-Acosta, Vadillo, & Fuentes-P, 2012; Pinho & Frenette, 2019). The continuous production of cells for maintaining homeostasis is a complex and highly regulated process, wherein the hematopoietic stem cells (HSC) take the topmost position in a hierarchical tree of generating different cell types (Ceredig, Rolink, & Brown, 2009).

Maintenance and replenishment of the differentiated blood cells is essential throughout the life span of an individual. Failure in replenishment of any of these differentiated cell types causes life threatening conditions, such as anemia (due to loss of erythrocytic mass), bleeding (due to loss of platelets) and infections (due to loss of myeloid and lymphoid cells). Differentiated cells are produced through the maturation of their lineage restricted hematopoietic progenitors (HPC); meanwhile, most HSCs are maintained as a continuous supply pool (Pelayo et al., 2012).

HSCs arise from an early stage of embryonic development. Primitive hematopoiesis occurs in the yolk sac, while definitive hematopoiesis establishes after the primitive stage and takes place in various niches of the fetal tissue (Ceredig et al., 2009). In adults, HSCs are majorly localized in the bone marrow, but may however expand to other tissues in diverse conditions of stress or disease such as primary myelofibrosis, bone marrow irradiation or recovery from chemotherapy (Crane, Jeffery, & Morrison, 2017).

HSCs are quiescent in the normal state of homeostasis, while the majority of the cells circulating are generated from the lineage specific multipotent progenitors as shown in Figure 1A (Ceredig et al., 2009; Pelayo et al., 2012). Hematopoietic progenitor cells (HPCs) in the bone marrow are restricted to a cellular compartment that expresses

CD34. Hence the subset of these multipotent progenitors can be characterized as Lin-CD34+CD38-/$^{lo}$CD10-CD45RA-. Multipotent early progenitors (MPP) progenitors differentiate from HSCs into lineage-committed progenitors such as common lymphoid progenitors (CLP) or common myeloid progenitors (CMP). CLPs give rise to cells in lymphoid lineage upon further differentiating into B-cells, T-cells, and natural killer (NK) cells, but CLP do not have the potential to differentiate into mature cells from myeloid lineage. Similarly, CMP may generate erythrocytes, megakaryocytes, granulocytes, and monocytes. Some studies have demonstrated the existence of a lymphoid-primed multipotent progenitor (LMPP) (Ceredig et al., 2009; Pelayo et al., 2012). LMPPs express high levels of SCA1 (stem cell antigen 1), KIT and FLT3 (FSM-like tyrosine kinase receptor 3) but lack differentiated cell specific markers and thus show a specific marker constellation - Lin–SCA1$^{hi}$KIT$^{hi}$FlT3$^{hi}$ (Crane et al., 2017). Hence these cells can differentiate into lymphoid lineage specific cell types but do not loose their potential to give rise to cells from myeloid lineage.

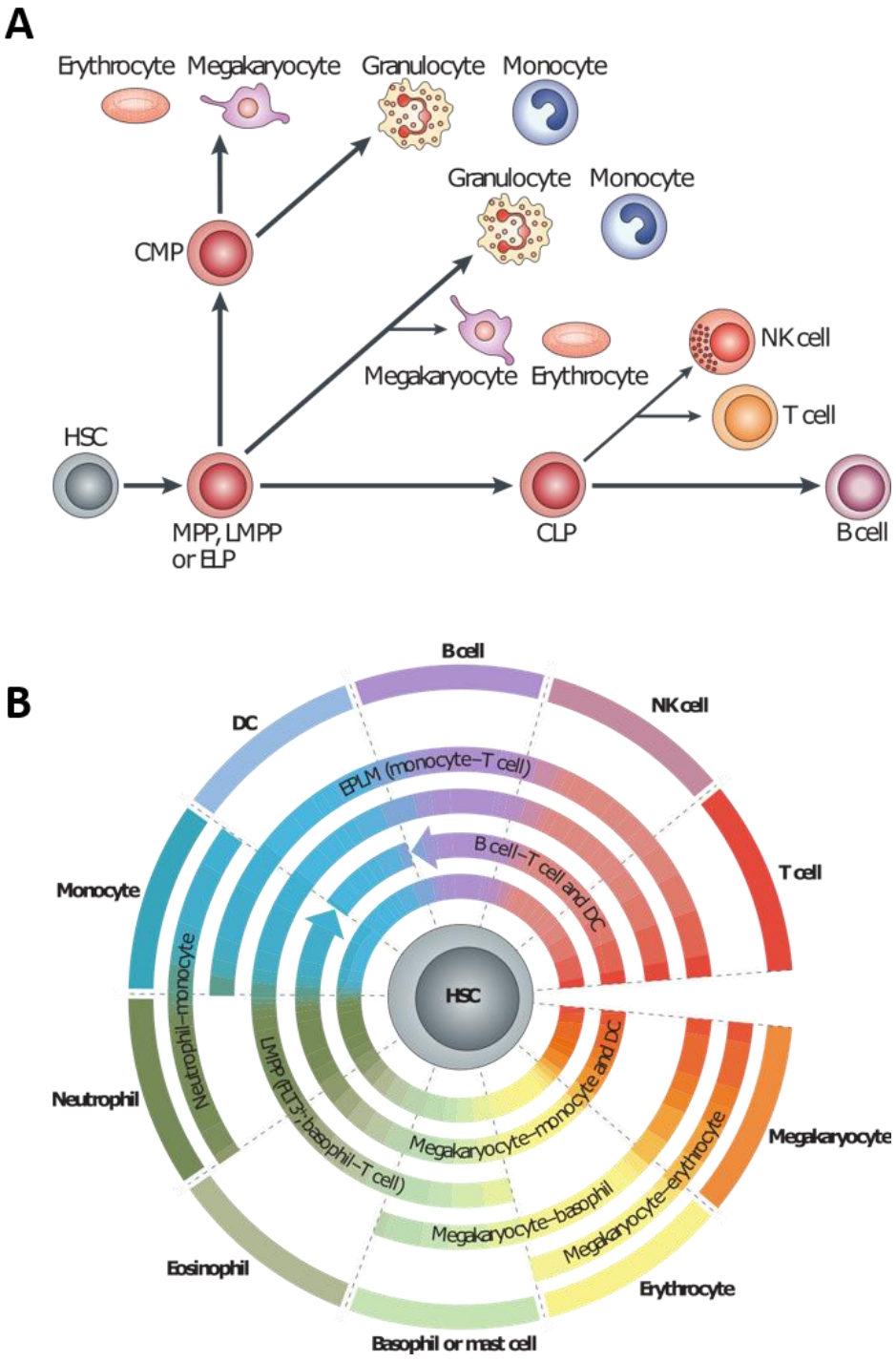


***Figure 1: Models of hematopoiesis***

*(A) Hierarchical tree models of hematopoiesis indicate individual branches from hematopoietic stem cells differentiate into multipotent progenitor and further differentiate into megakaryocytes, erythroid cells, and myeloid cells, as well as for natural killer (NK) cells, T cells and B cells. (B) Pairwise relationships model of*

*hematopoiesis indicates a direct and continuous connection between hematopoietic stem cells and their oligopotent progeny. This model makes no assumptions about branching that defines a specific outcome upon differentiation. Arcs indicate the known oligopotent progenitor cells and a particular cell fate could be achieved through more than one type of progenitor cell. CLP, common lymphoid progenitor; CMP, common myeloid progenitor; ELP, early lymphoid progenitor; GMP, granulocyte–monocyte progenitor; HSC, hematopoietic stem cell; LMPP, lymphoid-primed multipotent progenitor; MBP, myeloid–B-cell progenitor; MEP, myeloid–erythroid progenitor; MPP, multipotent progenitor; MTP, myeloid–T-cell progenitor. This figure was modified from (Ceredig et al., 2009).*

This classical hierarchical differentiation tree was functionally demonstrated by means of cell transplantations in mice and *in vitro* differentiation assays. However, newer single-cell gene expression studies are beginning to challenge this model, using a pairwise relationship model to depict a developmental relationship between HSCs and the differentiated cells generated from it. In this model, the cell fate can be determined from the intrinsic expression profiles of the cells depicted as broken circles around the HSCs as shown in Figure 1B (Ceredig et al., 2009). HSCs developing into to immune cell, progress towards their cellular fate (as shown from the inner most arc, as HSCs can generate all the cell types) and further into intermediate stages depicted by the outer arcs (as potential progenitor cells that can generate several but not all cell types). These cells finally progress into a committed stage as depicted in the outermost arcs (that potentially loses capability to transform into cell from different lineage). To summarize, these findings gradually document that hematopoietic cells might have the plasticity in lineage choice until the most developed stage of cell fate finally loses its potential to form all cell types.

### 4.1.1 Defects in hematopoiesis and development of blood malignancies

HSCs are commonly used stem cells obtained from bone marrow, cord blood and mobilized peripheral blood transplants and are the basis for stem cell transplantation therapy. Cells from bone marrow and HSCs serve a curative potential in clinical settings, such as disorders in bone marrow development causing Fanconi anemia, hematopoietic malignancies such as leukemias or lymphomas, and hematopoietic disorders such as

immunodeficiencies and sickle cell anemia (Crane et al., 2017; Krause & Van Etten, 2007). Before transplantation of HSCs from the donor to the recipient, bone marrow of the recipient patient is ablated using conditioning regimen in order to eliminate the existing hematopoietic process in the bone marrow and enables the engraftment of HSCs. Allogenic transplantation of HSCs based therapy for blood malignancies associates with increased risk of graft versus host disease, atypical infections, and long-term hospitalization. However, the success rate of transplantation-based therapies has gradually improved with better strategies towards engraftment success while minimizing toxicity from conditioning regimens (Crane et al., 2017; Krause & Van Etten, 2007).

Leukemia is a blood malignancy characterized by uncontrolled generation of hematopoietic progenitors that either remain immature causing acute leukemia or still manage to differentiate into peripheral leukocytes causing chronic leukemia. Leukemias can also be sub-categorized depending on their origin: myeloid leukemias are cells from cells of granulocyte, monocyte, erythroid or megakaryocytic lineage., while lymphoid leukemias occur from lymphoid progenitors (Krause & Van Etten, 2007).

## 4.2 Acute myeloid Leukemia

Acute myeloid leukemia (AML) is a clonal disease of the hematopoietic stem or progenitor cell (HSPC) and is characterized by intense proliferation, blocked differentiation of primitive hematopoietic cells and aberrant self-renewal activity (De Kouchkovsky & Abdul-Hay, 2016; Krause & Van Etten, 2007). Quiescent cells that survive conventional chemotherapy upon relapse or refractory AML cases, could be ascribed to leukemic stem cells (LSC) resistant to the treatment as shown in Figure 2.

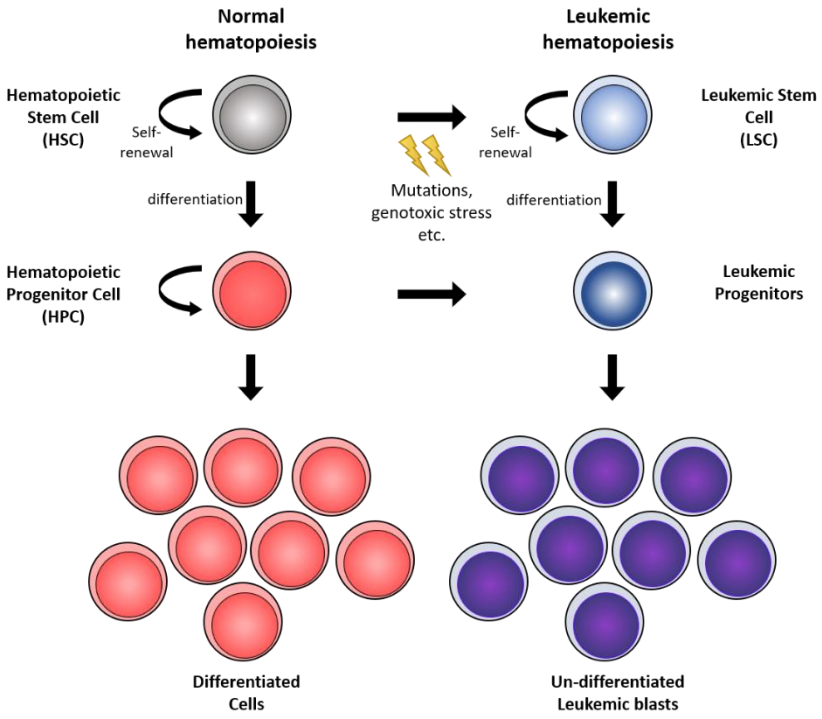


***Figure 2: Defects in hematopoiesis and leukemic stem cells***

*Normal hematopoietic stem cells (HSC) differentiate into progenitors and mature blood cells within the bone marrow, but accumulation of mutations or exposure to genotoxic agents could transform HSC into leukemic stem cell (LSC). These LSCs maintain growth potential and can generate leukemic progenitor and blast cells. Modified from (Pelayo et al., 2012).*

AML can be cured in about 30-40 % of younger adult patients (18-60 years), while only 5-15 % of patients older than 60 years can be cured (Dohner, Weisdorf, & Bloomfield, 2015; Papaemmanuil et al., 2016). Recently, a vast number of targeted therapies has been approved for AML treatment; however, conventional chemotherapy remains the major treatment option along with allogenic hematopoietic cell transplant for cure. Conventional chemotherapy leads to remission in about 70% of patients (in which bone-marrow morphology and cytogenetics are normal and blasts comprise <5% of marrow cells) but the majority of patients do relapse within 5 years (Crane et al., 2017; De Kouchkovsky & Abdul-Hay, 2016; Krause & Van Etten, 2007).

Older patients are affected considerably, as they are unfit for standard intensive therapies or often are refractory to treatment and eventually succumb to the disease with a median survival of only 5-10 months (Crane et al., 2017; Krause & Van Etten, 2007; Schmid et al., 2015; Stein & Tallman, 2016). Hence, it is essential to develop treatment options with reduced toxicity that can limit the progression of AML.

### 4.2.1 Classification and risk stratification

Classification strategies for AML have been established as early as in 1976 using the French-British-American (FAB) system. The FAB classification categorizes AML in eight sub-types from M0 to M7 depending upon morphological and cyto-chemical characteristics of the leukemic cells (Crane et al., 2017; De Kouchkovsky & Abdul-Hay, 2016; Krause & Van Etten, 2007). However, with fast-paced advances in AML genetics, the FAB classification became insufficient to guide treatment and prognosis. Therefore, the World Health Organization (WHO) introduced an updated classification of AML incorporating genetic information with morphological, phenotypical, and clinical outcome. The WHO classification of AML can be categorized in six different sub-types; AML with recurrent genetic abnormalities; AML with myelodysplasia-related features; therapy-related AML; AML not otherwise specified; myeloid sarcoma; and myeloid proliferation related to Down syndrome (Krause & Van Etten, 2007).

Besides the FAB and WHO classifications of AML, risk of relapse/death classifications are crucial to assess prognosis and guide treatment. The most commonly used risk classification is the so-called European LeukemiaNet (ELN) classification (Papaemmanuil et al., 2016), which integrates cytogenetic and genetic data of commonly AML-associated driver mutations and stratify AML cases into favorable, intermediate, and adverse risk groups (Figure 3).

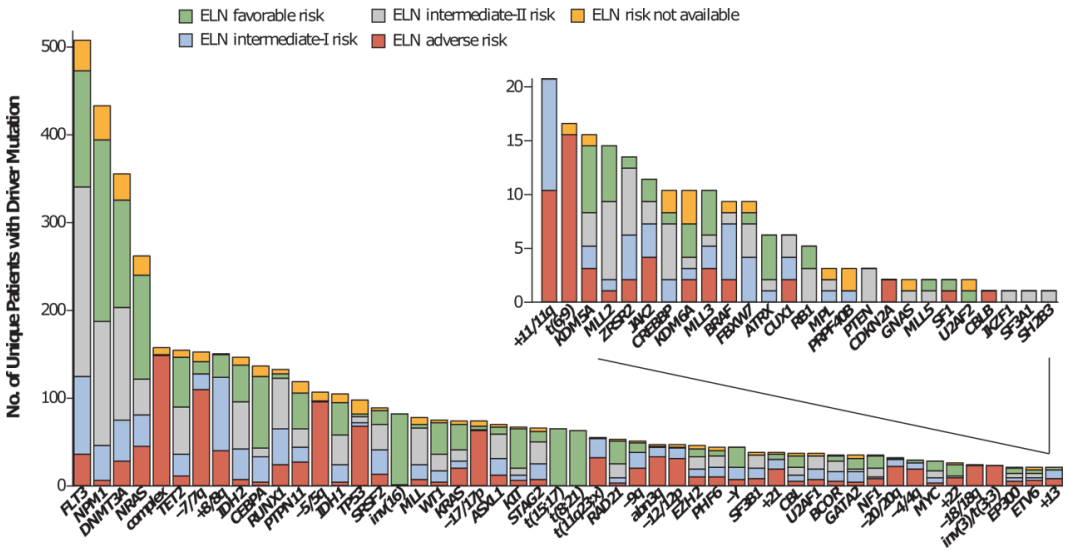


***Figure 3: Risk stratification in CN-AML***

*Driver mutation panel of 1540 AML patients. Each bar denoting commonly altered driver lesions which include gene mutations, chromosomal aneuploidies, fusion genes, and complex karyotypes. Molecular risk is classified according to the European LeukemiaNet (ELN) classification. Modified from (Papaemmanuil et al., 2016).*

Chromosomal rearrangements such as t(8;21), t(15;17) or inv(16) are categorized into the favorable risk group with overall survival rates of 66% in younger patients (<60 years) and 33% in elderly (>60 years). On the other hand, the appearance of a complex karyotype (defined as three or more chromosomal abnormalities), a monosomy 5 or 7, t(6;9) or chromosomal alterations involving the MECOM transcription factor (inversion(3) or t(3;3)) are categorized into the high risk group with significant lower chances of survival. The third group, categorized as an intermediate prognostic risk group, mainly comprises patients with normal cytogenetics (CN-AML) (Papaemmanuil et al., 2016; Schmid et al., 2015).

CN-AML represents a genetically heterogeneous group within all AML cases and accounts for up to 50% (Dohner et al., 2015; Schmid et al., 2015). Next-generation sequencing (NGS) has allowed us to discover and characterize several genetic mutations involved in the development and progression of AML (Garg et al., 2015; Papaemmanuil et al., 2016; Shouval et al., 2020). FMS-like tyrosine kinase 3 (*FLT3*) is one of the most commonly mutated genes affecting about 30% of CN-AML cases. FLT3-internal tandem

duplication (*FLT3-ITD*) mutations are associated with poor overall survival and are an independent prognostic factor for relapse. In *FLT3-ITD*, a short DNA sequence is copied and inserted directly in front of the original sequence, normally seen within the juxta-membrane domain resulting in constitutive activation of FLT3 followed by uncontrolled activation of downstream signaling pathways and subsequently uncontrolled proliferation and resistance to apoptotic cell death as shown in Figure 4 (Dohner et al., 2015).

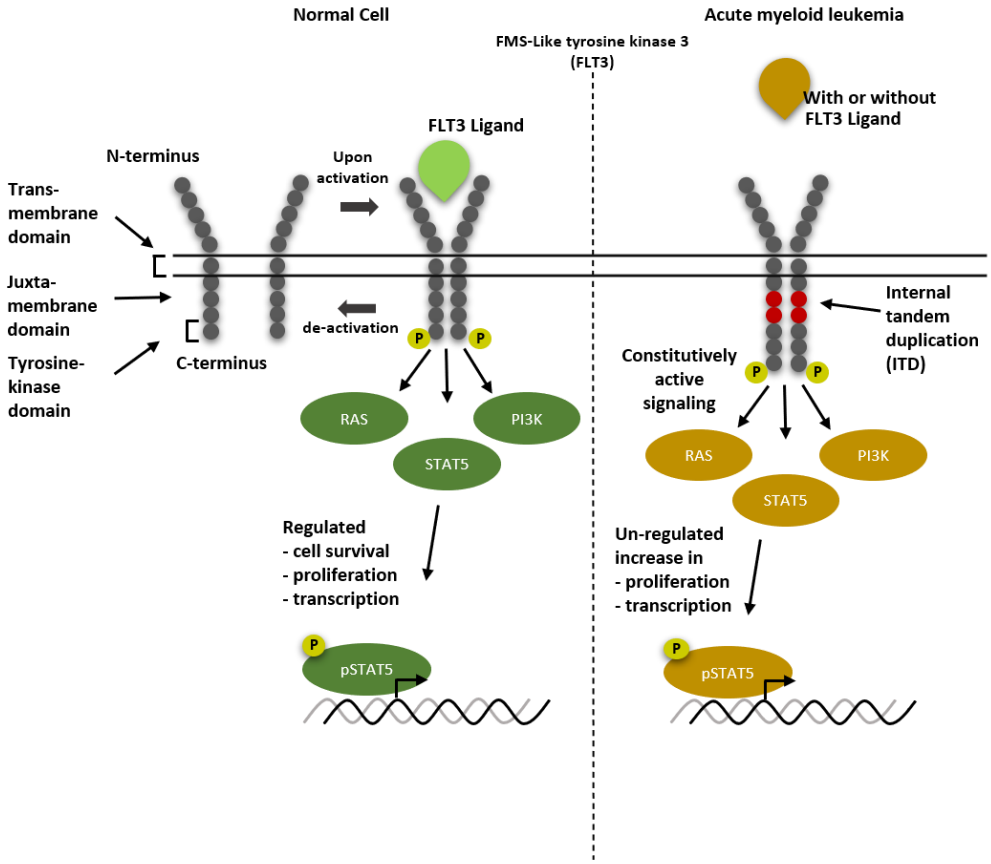


***Figure 4: FLT3 mutation in AML***

*A schematic representation of FMS-like tyrosine kinase 3 mutation in AML. In FLT3-internal tandem duplication (FLT3-ITD), a short DNA sequence is copied and inserted directly in front of the original sequence, normally seen within the juxta-membrane domain resulting in constitutive activation of FLT3 followed by uncontrolled activation of downstream signaling pathways and subsequently uncontrolled proliferation and resistance to apoptotic cell death.*

NGS has further revealed recurrent mutations in the epigenetic regulators such as DNA methyltransferase (*DNMT3A*) and Ten-Eleven Translocation-2 (*TET2*) (REF). *DNMT3A* mutations can be detected in about 23% of AML cases and are usually associated with poor outcome (Dohner et al., 2015). Interestingly, simultaneous expression of *FLT3-ITD* and mutant *TET2* in a murine leukemia model resulted in an aberrant DNA methylation profiles completely different compared to the expression of each mutation alone (Daver et al., 2015; Dohner et al., 2015; Garg et al., 2015; Papaemmanuil et al., 2016).

Another mutation observed in CN-AML is a frame shift mutation in the *NPM1* gene. Although *NPM1* mutations are associated with good prognosis, concurrent mutations within *FLT3* or *DNMT3A* significantly worsens outcome (Daver et al., 2015; Dohner et al., 2015). Moreover, *TP53* is mutated in about 2-8 % of all the AML cases, in particular with unfavorable cytogenetics and complex karyotype; detection of *TP53* mutation is associated with very poor prognosis (Daver et al., 2015; Dellomo, Baer, & Rassool, 2019; Garg et al., 2015; Papaemmanuil et al., 2016). MLL-rearranged leukemias (partial tandem duplications of *KMT2A*), produce fusion proteins (such as MLL-AF9, MLL-AF6 etc.) encoding a histone methyltransferase, which is associated with worse prognosis (Daver et al., 2015; Papaemmanuil et al., 2016). Also, mutations in myeloid transcription factors such as *RUNX1* lead to transcriptional deregulation and an overall poor prognosis and cause impaired hematopoietic differentiation (De Kouchkovsky & Abdul-Hay, 2016; Dohner et al., 2015). Hence the need for developing biomarkers to enhance risk stratification in biologically and clinically heterogenous AML cases can improve the better predictability and OS rate for AML patients.

### 4.2.2 Current treatment options and emerging therapies

#### 4.2.2.1 Current therapy

The current chemotherapeutic approach in AML has not changed for more than 30 years. It consists of a so-called induction treatment with Cytarabine (AraC) and anthracycline (Idarubicine or Daunorubicine), followed by various cycles of high-dose AraC or, depending on the risk criteria, allogeneic stem cell transplant. Aim of the

induction therapy is to achieve a complete remission (CR; defined as less than 5% of blasts in the bone marrow); this is reached in around 60-80% patients with *de novo* AML. Failing to reach CR after induction treatment is commonly treated with a second, high-dose AraC- and anthracycline- based salvage cycle (De Kouchkovsky & Abdul-Hay, 2016; Dohner et al., 2015; Krause & Van Etten, 2007; Lowenberg & Rowe, 2016). However, this treatment commonly associates with high toxicity and increased treatment-related mortality.

Recently, several novel treatment approaches have been developed in the treatment of various AML subtypes – these are referred as targetable lesions. For instance, patients with acute promyelocytic leukemia (APL) defined by the PML-RARa fusion protein and a t(15;17) translocation demonstrate significant response when treated with all-trans retinoic acid and arsen trioxide (Dohner et al., 2015; Papaemmanuil et al., 2016). Other examples of targetable lesions include FLT3 mutations, IDH1 and IDH2 mutations or AML with the BCR-ABL fusion product (De Kouchkovsky & Abdul-Hay, 2016).

#### 4.2.2.2 New therapies

FLT3-ITD inhibitors

Recent advances in AML treatment allow targeting of mutant FLT3. FLT3 inhibitors can be classified into first and second generation as well as type I and type II. First generation inhibitors such as midostaurin (PKC 412) are multi tyrosine kinase inhibitors (TKI) and were developed for other purposes, but later discovered to be inhibiting FLT3 (Krause & Van Etten, 2007; Shouval et al., 2020). Second generation inhibitors such as quizartinib and gilteritinib, are more potent and specific FLT3 inhibitors. On the other hand, type I inhibitors such as midostaurin and gilteritinib bind to receptor in its active conformation, while type II inhibitors bind to the inactive conformation as well.

In CML, targeting BCR-ABL fusion gene encoding a constitutively active receptor tyrosine kinase represents a promising strategy. Single agent treatment with the BCR-ABL inhibitors imatinib mesylate has proven to be highly effective in achieving CR and long-term disease control (Krause & Van Etten, 2007). Although, the development of

FLT3 inhibitors for AML was based on the success in BCR-ABL inhibitors for CML, the clinical responses for single agent FLT3 inhibitors has not shown a similar success in AML (Daver et al., 2015; Shouval et al., 2020; Stein & Tallman, 2016). This has driven research to combine FLT3 inhibitors with other agents. For instance, midostaurin with cytarabine and daunorubicin chemotherapy led to significantly improved outcomes, and subsequently received regulatory approval in combination with first-line chemotherapy for AML with FLT3 mutations since 2017 (Daver, Schlenk, Russell, & Levis, 2019; Dellomo et al., 2019; Garg et al., 2015; Shouval et al., 2020; Tyner et al., 2018). This led to an outburst of several combination strategies which are currently tested in clinical trials and also the design and synthesis of new molecules.

IDH inhibitors

Around 20% of *de novo* AML cases harbor *IDH1/IDH2* gain of function mutation (Dohner et al., 2015; Papaemmanuil et al., 2016). Inhibitors such as AGI-6780 and AG-221 are available to specifically target and deregulate these functions and have shown remarkable potential in *in vitro* and *in vivo* models (Tyner et al., 2018).

## 4.3 Synthetic lethality and targeted approaches

The concept of synthetic lethality has been established around 100 years ago. It describes a compensatory mechanism between two genes, such as repression or mutation of one of the gene, leads to no significant outcome, as the second gene compensates for the loss. In doing so, making cells immensely dependent on the second gene. In this context, strategically targeting the second gene followed by cell death is termed as synthetic lethality. This concept was extensively studied for understanding of compensatory mechanisms in developmental biology (Li et al., 2019; Lord & Ashworth, 2013; Lord, Tutt, & Ashworth, 2015). With consistent improvements in sequencing and functional study in cancer models, the concept of synthetic lethality has gained attention as a putative targeting strategy for cancer therapeutics.

Synthetic lethality can be illustrated as a context-dependent vulnerability, in which genetic alterations or mutations in tumor suppressor genes in cancer cells induce higher

essentiality for cell survival in other, secondary genes. Inhibition or functional inactivation of the secondary gene thus become synthetically lethal for the cancer cells, while rendering non-cancerous cells unaffected. In 2005, research labs (Bryant et al., 2005; Farmer et al., 2005) discovered this concept and utilized it to selectively target ovarian cancer cells harboring germline *BRCA* mutations and was approved by Food and Drug Administration (FDA) for a targeted approach in treating breast cancer with germline *BRCA* mutation with PARP inhibitors (Sarah E. Caulfield, Christine C. Davis, & Kristina F. Byers, 2019).

## 4.4 Targeting DNA damage repair

Cells are constantly exposed to endogenous and exogenous genotoxic stress that can cause DNA damage accumulation. Endogenous factors such as reactive oxygen species (ROS) generated from the metabolic pathways in the cell can lead to oxidation and alkylation of DNA (Hoeijmakers, 2009). Mistakes during cellular processes such as replication and transcription can also contribute to DNA damage accumulation. Similarly, exogenous factors such as the exposure to chemotherapeutic drugs (Dellomo et al., 2019; Pant, Maitra, & Yap, 2019; Sachdev, Tabatabai, Roy, Rimel, & Mita, 2019) (e.g. Etoposide and platinum-based drugs) can rapidly induce DNA damage. Exposure to ionizing radiation (IR) and ultraviolet light (UV) are known exogenous factors responsible for inducing DNA damage.

Cells mitigate accumulated DNA damage elegantly by activating lesion-specific DNA damage response (DDR) pathways. Most commonly studied DDR pathways are base-excision repair (BER), mismatch repair (MMR), nucleotide-excision repair (NER), double-strand break (DSB) repair. Additionally, cells can bypass accumulated damage and/or lesion in S-Phase and continue replication process and cell cycle using translesion synthesis (TLS) pathway as shown in Figure 5A.

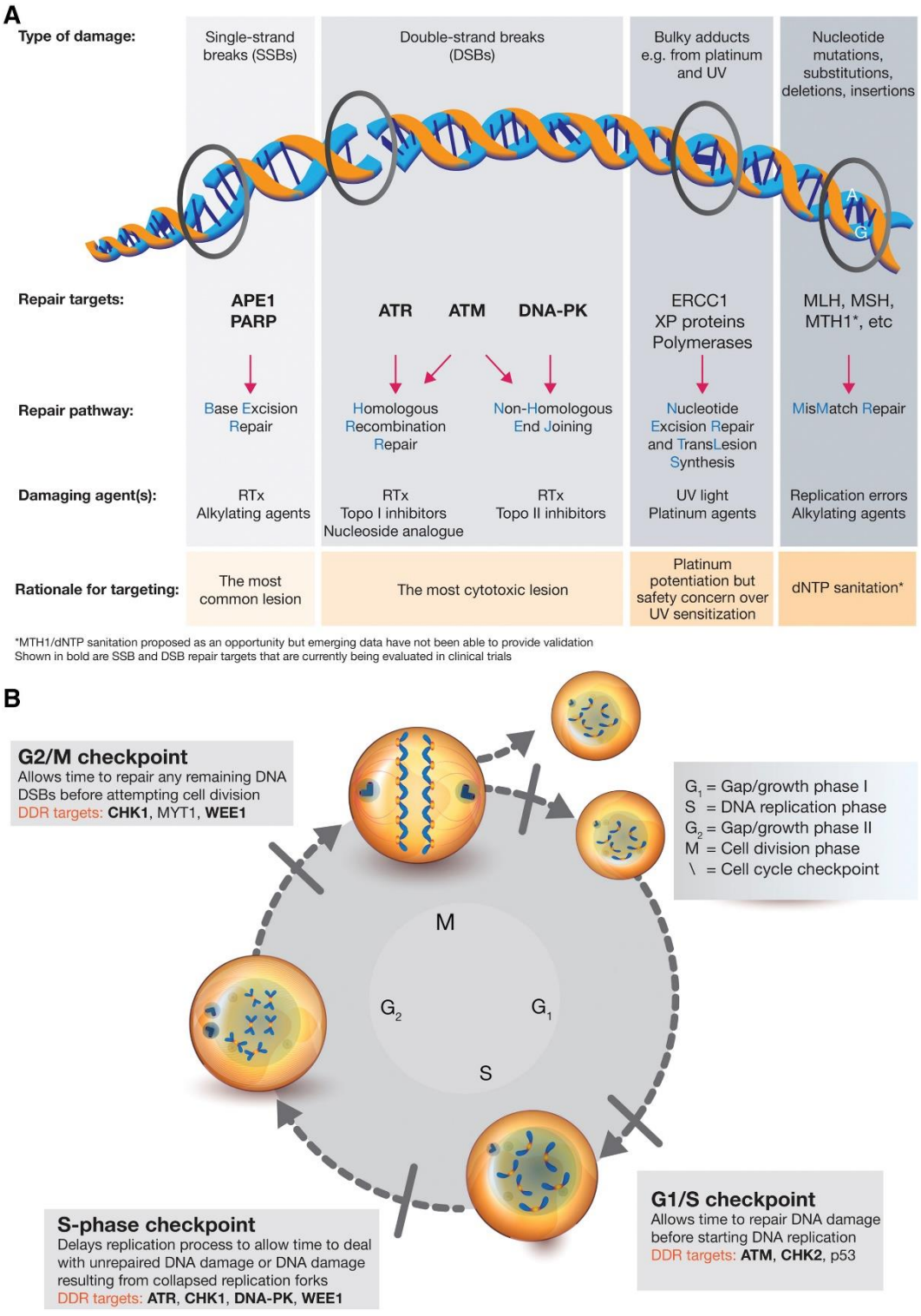


***Figure 5: DNA damage repair pathways and cell cycle checkpoints***

*(A) A schematic representation of different DNA damage repair (DDR) pathways based on the type of accumulated damage, such as single strand breaks (SSB), double strand breaks (DSB), bulky adducts or mutations and a rationale for targeting these pathways. (B) Cell cycle checkpoints allowing various DDR pathways to repair damage before moving further to the next checkpoint or proceeding towards the mitotic phase. These*

*cell cycle checkpoints can be targeted as shown in bold are currently evaluated targets in clinical trials. APE1, AP endonuclease 1; ATM, ataxia-telangiectasia mutated; ATR, ataxia-telangiectasia and Rad3-related; DNA-PK, DNA-dependent protein kinase; PARP, poly(ADP-ribose) polymerase; RTx, radiotherapy; Topo, topoisomerase. This figure was modified from (O'Connor, 2015).*

BER caused by DNA oxidation, deamination, or alkylation (Maynard, Schurman, Harboe, de Souza-Pinto, & Bohr, 2009) detects and repairs these lesions using DNA polymerase beta (POLB) by replacing the excised nucleotide and using LIG1-XRCC1 (Xray repair cross-complementing protein 1) complex to ligate and patch the lesion. NER recognizes DNA bulky lesions such as photoproducts caused by UV-light irradiation or cisplatin (Gong, Fahy, Liu, Wang, & Smerdon, 2008). Similar to BER, NER repairs the lesion using endonuclease mediated repair. MMR removes errors during DNA replication and can recognize DNA lesions induced by exogenous agents, such as cisplatin (Jiricny, 2006; Polo & Jackson, 2011). DSBs can be repaired primarily by two main pathways, a classical error prone non-homologous end joining (NHEJ) and homology-based recombination (HR). Both HR and NHEJ act as complementary mechanisms in repairing DSBs. HR is mainly predominant in S and G2 phases of cell cycle, as its essential step in repair requires the availability of intact DNA template. In contrast, classical NHEJ does not require an intact DNA template to mediate DSB repair, hence its predominantly active in G1 phase of cell cycle where intact DNA template is not available as shown in Figure 5B.

### 4.4.1 Role of PARP in DNA damage repair pathways

One of the key proteins of interest that regulates DDR is the PARP family proteins. PARP family members comprise 17 members based on the homology shared with the PARP1 (Poly(ADP-ribose) polymerase 1), but not all of the members are enzymatically active. In fact, only four of the PARP family members, PARP1, PARP2, PARP5a, and PARP5b are enzymatically active, possessing intrinsic polymerase activity (Gogola, Rottenberg, & Jonkers, 2019; Hottiger, Hassa, Lüscher, Schüler, & Koch-Nolte, 2010). PARP proteins are known to transfer negatively charged ADP-ribose groups donor NAD+ onto target

proteins in a process defines as poly-ADP-ribosylation (PARylation) (Ray Chaudhuri & Nussenzweig, 2017) as shown in Figure 6.

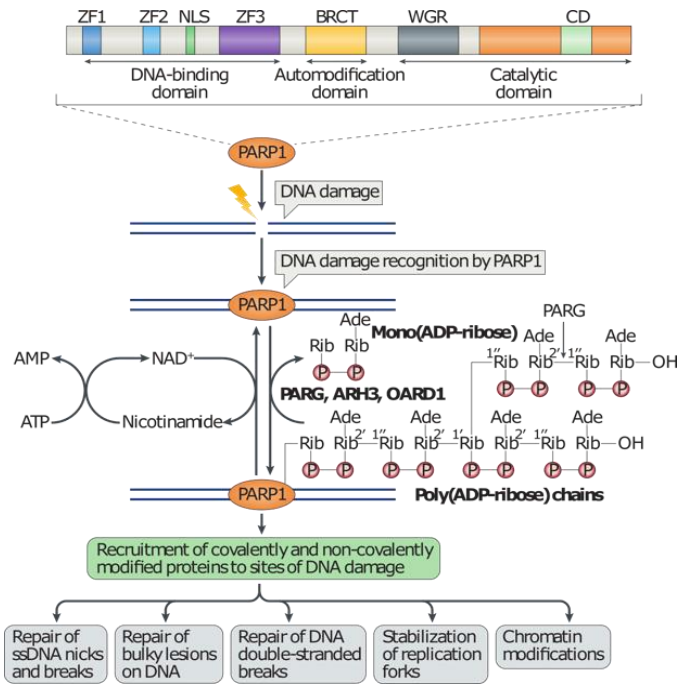


***Figure 6: PARP and PARylation***

*Multiple poly(ADP-ribose) polymerase 1 (PARP1) domains are shown and the conserved domain (CD) contains the active site that binds to NAD+ and also to the Trp-Gly-Arg (WGR) domain. PARP1 detects DNA damage through its DNA-binding domain (DBD) and synthesizes poly(ADP-ribose) (PAR) chains. PAR chains are rapidly catabolized by PAR glycohydrolase (PARG). Poly(ADP)ribosylation (PARylation) of PARP1 itself and other target proteins results in the recruitment of DNA damage repair proteins. Ade, adenosine; P, phosphate residue; Rib, ribose moiety; ssDNA, single-stranded DNA. This figure was modified from (Ray Chaudhuri & Nussenzweig, 2017).*

Both PARP1 and PARP2 can repair DNA lesions, but the majority of cellular PAR activity is attributed to PARP1 (Kim, Zhang, & Kraus, 2005; Luo & Kraus, 2012). PARylation is a post-translational modification and is implicated in various processes within the cell. PARylation is a transient and reversible modification, as its turnover is rapidly mediated by poly(ADP-ribose) glycohydrolase (PARG). The eviction of PARP1 from DNA damage sites is additionally regulated by the E3 ubiquitin ligase CHFR, which ubiquitinates PARylated but not un-PARylated PARP1, suggesting that there are several mechanisms

that control PARP1 activity upon DNA damage (Gogola et al., 2019; Jachimowicz, Goergens, & Reinhardt, 2019).

PARP1 serves as a sensor and recognizes DNA breaks early on. Its activity is primarily focused on recruiting factors essential in SSB and DSB repair mechanism. As shown in recent data, PARP1 deficiency can cause delayed activation of factors and proteins involved in DDR pathways such as phosphorylated histone 2A (gH2AX, surrogate for DSBs) (Faraoni et al., 2015), p53 or structural maintenance of chromosomes protein 1 (SMC1) (O'Connor, 2015; Ray Chaudhuri & Nussenzweig, 2017).

PARP1 is required at different stages and plays essential roles in SSB repair mechanisms. PARP1 recruits XRCC1 to the site of SSBs and further enables recruitment of polynucleotide kinase 3‘- phosphatase (PNKP), aprataxin (APTX) and DNA ligase 3 (LIG3) to the SSBs, eventually enabling gap filling by POLB and the DNA damage is resolved (Ray Chaudhuri & Nussenzweig, 2017).

Considering its role in SSBs, PARP inhibition (PARPi) was initially considered to cause accumulation of unresolved SSBs, which were then converted to DSBs during replication (Kim et al., 2005; Luo & Kraus, 2012; Ray Chaudhuri & Nussenzweig, 2017). Recent studies suggest that some of the PARP inhibitors induce PARP mediated lesions on the DNA by trapping PARP1 at the site of damage and by blocking its auto-PARylation activity as shown in Figure 7. This trapped PARP1 on the DNA is the relevant toxic equivalent reminiscent of topoisomerase II inhibitors, such as etoposide, which also “trap” their target enzyme on the DNA (Michelena et al., 2018; Shen, Aoyagi-Scharber, & Wang, 2015; H. R. Singh et al., 2017).

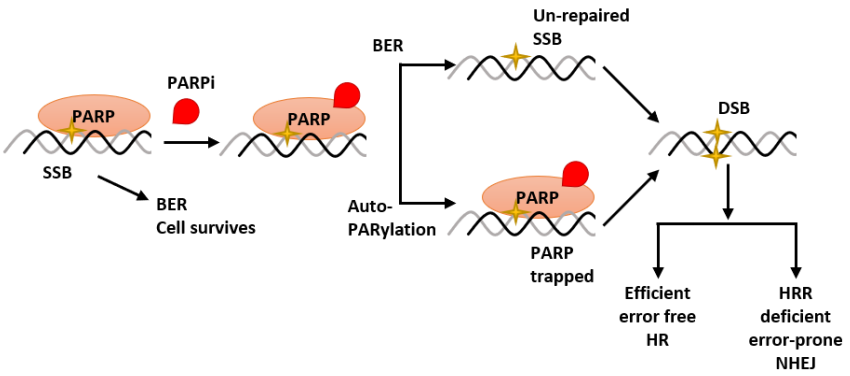


***Figure 7: PARP inhibition mediated repair pathways activation***

*PARP inhibition impairs single strain break (SSB) repair such as base excision repair (BER) and causes PARP1 to be trapped by inhibiting its auto-PARylation activity resulting in unresolved DNA double strand breaks that require homologous recombination (HR) repair pathways to mediate damage. Cell deficient in proteins involved in HR-mediated repair lead to cell death. This figure was modified from (Mateo et al., 2019).*

In normal condition, PARP mediates the recruitment of protein to sites of damage and activates DNA repair pathways. Upon completion, PARP PARylates these proteins and itself (auto-PARylation) followed by release from the DNA lesion and restart of the stalled replication fork. Upon inhibition of PARP, PARP's ability to auto-PARylate is affected causing PARP trapping at the lesion site, stalling of the ongoing replication fork and a S and G2-phase arrest (Jachimowicz et al., 2019). It is in these stages where cells would have access to error free HR pathways to repair DNA lesions and restore replication.

PARP1 plays a pivotal role in recruiting DSB sensors like meiotic recombination 11 (MRE11) and Nijmegen breakage syndrome protein 1 (NBS1) to the site of damage. By recruiting MER11 and NBS1, PARP1 enables the formation of the MRN complex (MER11, RAD50 and NBS1) at the site of DSBs and mediates repair via HR pathway. Proteins involved in DDR can be classified based upon their function in mitigating DSBs as shown in Figure 8.

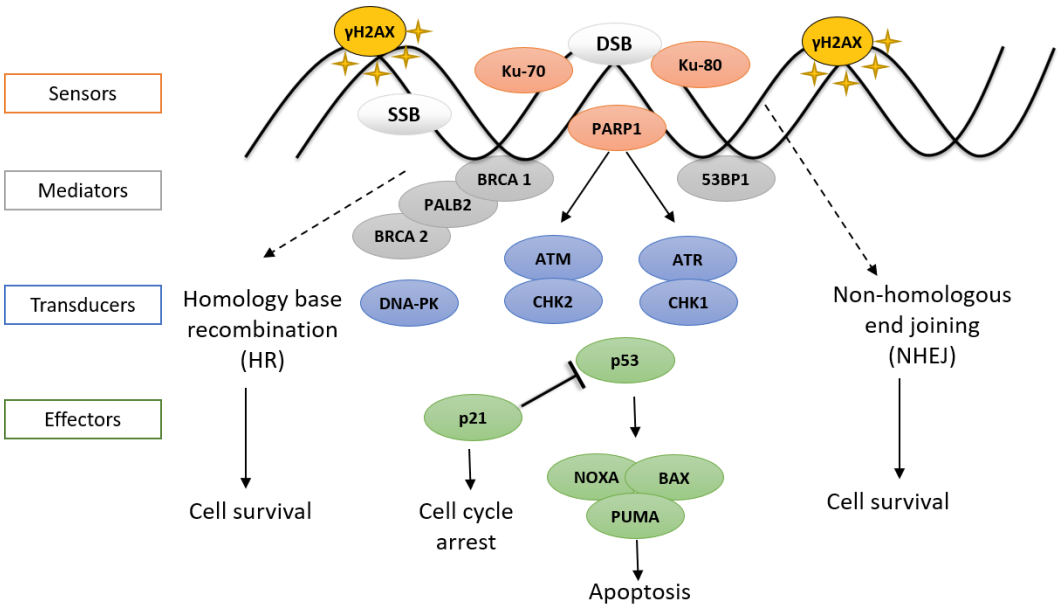


***Figure 8: Overview of DNA damage response***

*A schematic representation of DNA damage response (DDR), which consists of various proteins that can be categorized based on the activity as sensor of DNA damage, mediator, transducers, and effectors. This figure was modified from (Arai et al., 2018).*

The initial step of HR-mediated DNA damage repair is resection of DSBs by endo- and exonucleases such as MRE11, DNA2 and EXO1. Recruitment of MER11 by PARP1 to the site of DSBs could determine DNA repair-pathway choice by channeling the repair of DSBs towards HR (Branzei & Foiani, 2008; Chao et al., 2017; Diamant et al., 2012). Endonuclease incision by MER11, followed by its exonuclease activity digesting 3'-5' toward the DNA end, coupled with CtIP (CtBP-interacting protein) and EXO1, carries out the resection of DNA into a single stranded DNA (ssDNA). This ssDNA is coated by RPA (Binz, Lao, Lowry, & Wold, 2003), which is subsequently replaced by RAD51 in a BRCA2-dependent manner. RAD51 nucleoprotein filaments mediate strand invasion on the homologous sister chromatid (Ciccarone, Zampieri, & Caiafa, 2017; Costanzo, 2011; Ray Chaudhuri & Nussenzweig, 2017).

During NHEJ, PARP1 enables the recruitment of non-catalytic subunits Ku70 and Ku80 to free ends of DNA and allows recruitment of DNA-PKs (DNA dependent protein kinases) to the site of damage. If the ends of the break are not aligned, the ends can be trimmed to form compatible ends. Upon activation, DNA-PKs mediate the binding of

XRCC4 and DNA ligase IV (LIG4) to the damage site eventually joining the ends. Hence, this method of DSB repair is template DNA independent, but error prone. PARP1 is an important regulator in DDR pathways mediated by alternative NHEJ (alt-NHEJ). The major difference between classical NHEJ and alt-NHEJ is the binding of Ku-proteins (Ku-70 and Ku-80) to the DNA ends at the DSB, which promote classical NHEJ, whereas PARP1 binding itself in the absence of Ku-proteins promotes alt-NHEJ. Alt-NHEJ is more error prone than classical NHEJ resulting in a higher number of translocations, delayed end-joining and larger DNA deletions (Chang, Pannunzio, Adachi, & Lieber, 2017; Chao et al., 2017).

PAPR1 is also involved in regulation of cellular processes other than regulation of DDR pathways. PARP1 can bind directly to histones H1, H2A and H2B, thereby coordinating chromatin condensation (heterochromatin) whereas auto-PARylating of PARP1 from these histone marks enables open chromatin regions (euchromatin) (Ciccarone et al., 2017; H. R. Singh et al., 2017). Upon DNA damage, PARP1 can bind to histone tails and enable chromatin relaxation, histone eviction and repression of transcription allowing binding of various chromatin modulators to the site of damage to further relax the DNA structure and enable repair (Ciccarone et al., 2017).

PARP1 is also known to regulate cellular fates by PARylating p53 and blocking its cytosolic export, thereby enhancing p53 mediated transcription of DDR network genes (Cuella-Martin et al., 2016; Lashgari, Fauteux, Marechal, & Gaudreau, 2018). This indicates that PARP1 can act as stress sensor via the p53-p21 pathway. Interestingly, activation of caspase also cleaves PARP-1 during intrinsic apoptosis, thereby potentially regulating a balance between apoptosis and cell survival (Le Pen et al., 2016).

### 4.4.2 Clinical applications with PARP inhibitors

DNA damage is a double-edged sword, on the one hand essential to survive, on the other hand an important mediator of clonal evolution (Swindall, Stanley, & Yang, 2013). Aberrant DNA damage repair or dependencies on defined pathways might render cancer cells vulnerable to DNA damage repair pathway inhibition.

The first DDR-targeting approach that was approved for anticancer therapy are inhibitors of PARP in *BRCA1*- or *BRCA2*- mutant cells (Jachimowicz et al., 2019). BRCA1 and BRCA2 are essential proteins in the regulation of HR-mediated DSB repair and deficient or mutant cells demonstrated a marked sensitivity to PARP inhibitors. This inherent dependency on PARP for survival and marked success in clinical trials has led to the approval of PARP inhibitors Olaparib, Rucaparib, and Talazoparib in BRCA-deficient breast and ovarian cancers by the FDA and EMA (Lee & Konstantinopoulos, 2019; Sachdev et al., 2019). Deficiency in BRCA is currently being explored in other cancer entities like prostate cancer (Gogola et al., 2019), pancreatic cancer (Pant et al., 2019), and glioblastoma (Rasmussen et al., 2016). Sensitivity to PARP inhibitors in BRCA-deficient cancer models has shed light to a bigger picture, suggesting that deficiencies in other proteins involved in HR, such as RAD51, RPA1, ATM, CHK2, TOPBP1 and others confer sensitivity to PARP inhibition (Brown, O'Carrigan, Jackson, & Yap, 2017; Gogola et al., 2019). This loss of functionality was termed as 'BRCAness' as it shared a phenotype reminiscent of BRCA-deficient cancer models. Various studies are underway to extend the efficacy of PARP inhibitors in cancer models displaying a BRCAness phenotype (Dellomo et al., 2019; Lord & Ashworth, 2016; Severson et al., 2017).

Preclinical studies have shown therapeutic potential for PARP inhibitors like Olaparib and talazoparib in AML resulting in several ongoing clinical trials (attached table in supplements). PARP inhibitors are currently investigated in AML with FLT3-ITD mutations (Maifrede et al., 2018). The goal behind this combination is to a FLT3 signaling induced BRCAness-like phenotype. In addition, PARP inhibitors might also target upregulated error-prone Alt-NHEJ pathway, thereby decreasing genomic instability and development of resistance to therapy (Dellomo et al., 2019).

PARP inhibitors are also investigated in combination with epigenetic drugs, such as DNMT1 inhibitors to induce synergistic cytotoxicity in AML (Muvarak et al., 2016). PARP inhibition traps PARP1 to the site of damage. The combination with DNMT1 inhibitors (like decitabine or azacytidine) resulted in large DNMT1-PARP1 complexes trapped to DNA break site. These bulky adducts causes substantial toxicity in AML cells finally leading to increased rates of cell death. This has led to Phase I clinical trial, investigating

the efficacy of the combination of the DNMT inhibitor decitabine with PARP inhibitor Talazoparib (Clinical trial ID: NCT02878785). PARP inhibitors are also explored in combination with histone deacetylase (HDAC) inhibitors and have shown similar responses as DNMT inhibitors. HDAC inhibitors also inhibit NHEJ by acetylation of Ku70, Ku80, and PARP in AML cell lines and AML patient samples. PARP acetylation is associated with relaxing the chromatin, thereby increased binding, and subsequent trapping to DSBs causing eventual cell death (Dellomo et al., 2019).

PARP inhibitors are explored in combination with immune checkpoint blockade therapy. The rationale behind this combination is to induce PARP inhibition-mediated DNA damage, and accumulation of damage leads to abundant neoantigen due to chromosomal rearrangements, which enhances tumor immunogenicity. The effectiveness of immune therapy is based on upregulation of neoantigens in tumor immune microenvironment, for instance PD-L1 levels. Hence PARP inhibition could sensitize patients to immune therapy by upregulation of PD-L1, and subsequently enhance its effectiveness in patients (Li et al., 2019).

## 4.5 Targeting apoptosis

Apoptosis is an evolutionary mechanism to induce programmed cell death in undesirable and potentially harmful cells. This mechanism was first characterized in early 1970 in mammalian tissue sections, where the dying cells displayed a nuclear condensation and cellular fragmentation. These cellular fragments were termed apoptotic bodies and were phagocytosed by nearby white blood cells (Montero & Letai, 2018). The apoptotic pathways can be divided in two main categories: extrinsic pathway and intrinsic pathway. Both of these pathways merge by activation of caspase 3 and caspase 7 eventually causing caspase-mediated cell death (Bock & Tait, 2020).

### 4.5.1 Extrinsic apoptotic pathway

The extrinsic apoptotic pathway is dependent on activation of plasma membrane receptors (also known as death receptor) such as TNFR, FAS (CD95) and DR3/ WSL.

Specific ligand binding to the receptor induces intracellular changes, promotes activation of death-inducing signaling such as the formation of caspase 8. Active caspase 8 activates BH3-interacting domain death agonist and propagates apoptosis by cleaving pro-caspase 3 and pro-caspase 7 into their active conformation and orchestrates programmed cell death as shown in Figure 9 (Bock & Tait, 2020; Cassier, Castets, Belhabri, & Vey, 2017).

### 4.5.2 Intrinsic apoptotic pathway

Intrinsic apoptotic pathway (also known as mitochondrial apoptotic pathways) is activated by various factors such as cellular stress, DNA damage and genotoxic agents (REF). Major tumor suppressor pathways such as retinoblastoma protein (RB)-mediated and p53-mediated activation of proapoptotic signal converge on the mitochondrial outer membrane permeabilization (MOMP) (Le Pen et al., 2016). Evading apoptotic signals is a pivotal stage in cancer development, and hence characterized as one of the hallmarks of cancer (Hanahan & Weinberg, 2011). The BCL2 (B-cell lymphoma/leukemia 2) family of proteins regulates the MOMP and subsequent activation of apoptosis. Intracellular signals such as DNA damage causes the activation of BCL2 homology domain 3 (BH3)-only members of the BCL2 family of proteins. These BH3-only proteins inhibit anti-apoptotic proteins such as BCL2 and promote MOMP, leading to the release of the intramembrane space protein, cytochrome c (cyto-c) into the cytosol of the cells. In the cytosol, cyto-c binds to apoptotic peptidase activating factor 1 (APAF1) forming the apoptosome. This complex recruits and activates caspase 9, which leads to further activation of caspase 3- andcaspase 7-mediated induction of apoptosis (Bock & Tait, 2020; Cassier et al., 2017; Konopleva & Letai, 2018; Radha & Raghavan, 2017) as shown in Figure 9 (REF).

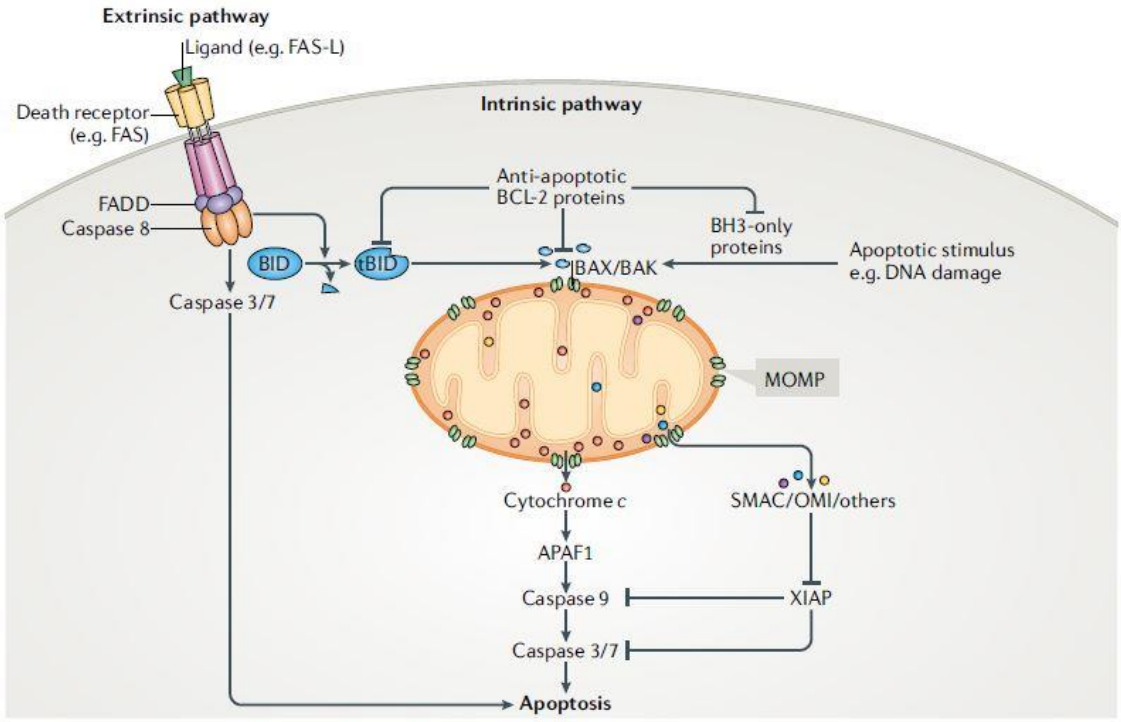


***Figure 9: Extrinsic and Intrinsic apoptosis***

*The extrinsic (also known as death receptor) apoptotic pathway involves the binding of a death receptor ligand to death receptors (members of the tumor necrosis receptor superfamily) upon external signals and activates apoptosis. The intrinsic apoptotic pathway is induced by various means such as, DNA damage, growth factor withdrawal and mitotic arrest. This leads to activation of BH3-only members of the B cell lymphoma 2 (BCL-2) protein family. BH3-only proteins inhibit anti-apoptotic BCL-2 proteins and activate mitochondrial outer membrane permeabilization (MOMP) via activation of BCL2-associated X protein (BAX) and BCL2 antagonist/killer 1 (BAK). This leads to release of cytochrome-c into to the cytoplasm and activates Caspases-mediated programmed cells death. This figure was modified from (Bock & Tait, 2020).*

BCL2 family of proteins are the key regulators of the intrinsic apoptosis pathway. BCL2 was discovered as a part of the t(14;18) chromosomal translocation, which was commonly found in follicular B-cell lymphomas as an apoptotic regulator (Pentimalli, 2017). All the members of BCL-2 family share one or more BH domains from BH1 to BH4 and can be categorized based on their structure (BH domains) and the role they play in regulating apoptosis. Apoptosis is initiated by pro-apoptotic, BH3-only proteins containing a single BH domain, in this case, BH3. Commitment to undergo apoptosis is regulated by BH3-only 'activator' proteins, such as, BCL-2-interacting mediator of cell

death (BIM), encoded by *BCL2L11*; BH3-interacting domain death agonist , encoded by *BID*; p53-upregulated modulator of apoptosis (PUMA), encoded by *BBC3*, and NOXA, also known as PMA- induced protein 1, encoded by *PMAIP1*. These proteins bind and activate pro- apoptotic membrane permeabilizing proteins such as BCL-2-associated X protein (BAX), encoded by *BAX*, or BCL-2 antagonist/killer (BAK), encoded by *BAK1*. The activation of BAX or BAK at the mitochondrial surface results in oligomerization and subsequently macropore formation in this membrane, causing MOMP (Bock & Tait, 2020; Cassier et al., 2017; Konopleva & Letai, 2018).

On the other hand, pro-apoptotic events are countered by the pro-survival (anti-apoptotic) BCL-2 family proteins such as, BCL-2, encoded by *BCL2*; B cell lymphoma extra-large (BCL- xL), encoded by *BCL2L1*; B cell lymphoma W (BCL-w), encoded by *BCL2L2*; BCL-2-related isolated from fetal liver 1 (BFL1), encoded by *BCL2A1*; and myeloid cell leukemia 1 (MCL1), encoded by *MCL1*. These proteins contain all BH domains (BH1–BH4) and can block apoptosis by binding and blocking monomeric BAX or BAK or BH3-only activator (Radha & Raghavan, 2017). These interactions are mediated by binding of the hydrophobic face of the BH3 domain into a hydrophobic groove formed by the BH1–BH3 domains on the anti-apoptotic protein. Apoptosis occurs when pro-survival proteins are overwhelmed by BH3-only activators or sensitizers and activation of BAX and/or BAK leads into MOMP.

### 4.5.3 Regulation of intrinsic apoptosis

Diverse stimuli can trigger intrinsic apoptosis such as damage to cellular organelles causing endoplasmic reticulum stress (ER stress); mitochondrial damage or oncogene-induced cell death, for instance activation of MYC Proto-Oncogene (MYC) for cell growth and proliferation; genotoxic agents such as ionizing radiation, cytotoxic chemotherapy. Genotoxic drugs induce apoptosis by activating p53 and p53-mediated transcription of its target genes such as BAX, PUMA and NOXA (Konopleva & Letai, 2018; R. Singh, Letai, & Sarosiek, 2019) as shown in Figure 10.

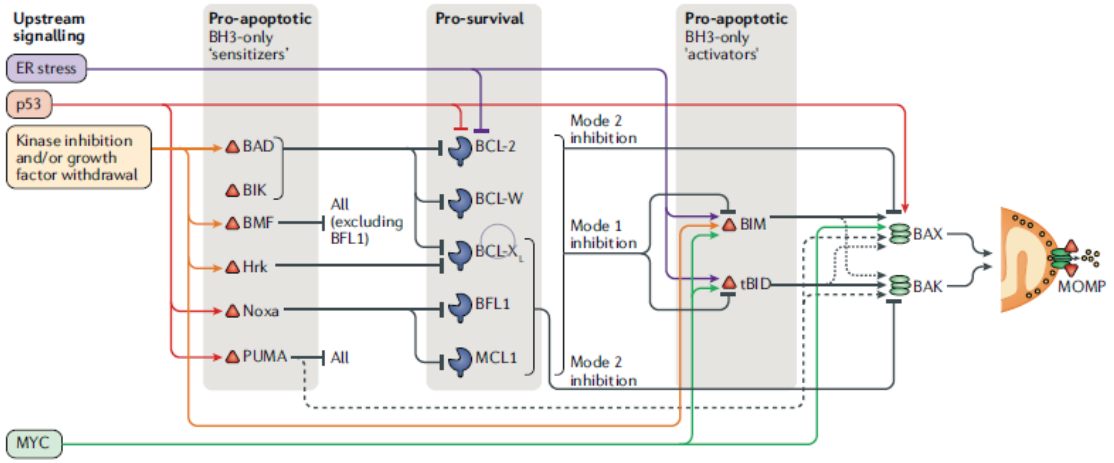


***Figure 10: Interactions between BCL2 family proteins in regulation of apoptosis***

*BCL-2 family proteins interact with each other in various ways regulating apoptosis. BH3-only 'activator' proteins (BCL-2-interacting mediator of cell death (BIM), truncated and active form of the BH3-interacting domain death agonist (tBID) and, p53-upregulated modulator of apoptosis (PUMA) (dashed lines)) can activate BCL-2-associated X protein (BAX) and/or BCL-2 antagonist/killer (BAK) to result in mitochondrial permeabilization. On the other hand, BH3-only 'sensitizer' proteins can bind and inactivate specific anti-apoptotic proteins directly and mediate the release of any BH3-only activators that are actively being blacked. Finally, anti-apoptotic proteins can also bind and block BAX or BAK directly via Mode 2 inhibition, preventing their oligomerization. Genotoxic stress and DNA damage can activate protein 53 (p53) and trigger apoptosis by modulating BH3-only 'sensitizer' such as PUMA and/or PMA-Induced Protein 1 (NOXA) or by regulating expression levels via MYC Proto-Oncogene (MYC) activity or activity of anti-apoptotic proteins like BCL2. This figure was modified from (R. Singh et al., 2019).*

These intricated redundancies in apoptosis pathway maintain a balance between pro-survival and pro-apoptotic proteins, which is essential for normal cells (non-cancerous) to evade apoptosis and sustain internal and/or external stress. On the other hand, anti-apoptotic proteins like BCL2, MCL1, BCL-xL are often highly expressed in cancer cells to maintain consistent survival by blocking pro-apoptotic proteins and subsequently evading apoptosis. These anti-apoptotic proteins are established targets for cancer drug development. Several approaches have been evaluated such as suppressing BCL2 expression, usage of natural products to enhance pro-apoptotic activity and development of small molecule inhibitors competitively targeting anti-apoptotic

proteins (also known as BH3 mimetics) to induce apoptosis specifically in cancer cells with minimal toxicity to normal somatic cells (Pullarkat & Newman, 2016; R. Singh et al., 2019). BH3 mimetics based small molecules have shown the most promising and advanced results with many ongoing clinical trials to evaluate its efficacy (Pentimalli, 2017; Reed, 2017). The rationale behind small molecules targeting anti-apoptotic proteins is that these inhibitors can permeabilize cell membranes and bind to the hydrophobic domains of specific anti-apoptotic proteins. For examples, Venetoclax (ABT-199) is a highly specific BCL2 inhibitor, which binds to the hydrophobic groove of BCL2 and actively competes with BH3-only activators and/or sensitizers in triggering apoptosis as shown in Figure 11

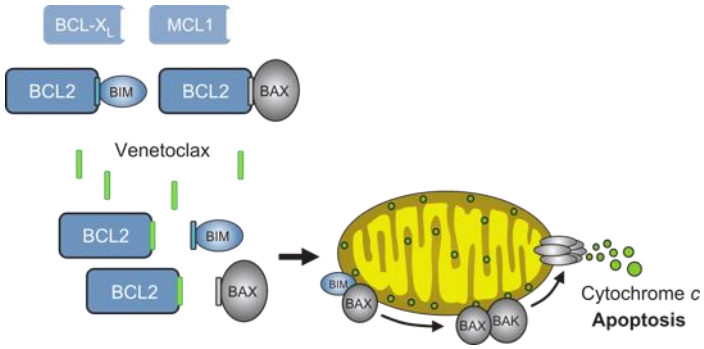


***Figure 11: Mode of action of BH3 mimetic inhibitor; Venetoclax***

*Venetoclax is a BH3-minetic and a specific inhibitor of BCL2. It competitively binds to BCL2 and releases pro-apoptotic proteins such as BCL-2-interacting mediator of cell death (BIM), BCL2-like 11; BAX, BCL2-associated X protein; BAK, BCL2 antagonist/killer 1 leading to release of cytochrome-c into to the cytoplasm and activating Caspases mediated programmed cells death. This figure was modified from (Konopleva et al., 2016).*

### 4.5.4 BCL2 dependency

Development of specific inhibitors for anti-apoptotic proteins as potential therapeutic targets has enhanced the mechanistic understanding and appreciates the complexity in apoptotic pathways. Many cancer cells express high levels of anti-apoptotic proteins,

for example BCL2. However, only expression of one anti-apoptotic proteins does not seem to be a good predictor to BCL2 inhibition, also the quantity of BCL2-blocking, pro-apoptotic proteins such as BIM or BAX seem to identify cells “primed for cell death”. (Konopleva & Letai, 2018; Leverson et al., 2017; Montero & Letai, 2018).

Another strategy is to measure expression levels of more than one anti-apoptotic BCL2 members and calculate a ratio, for instance, the *BCL2/MCL1* mRNA ratio is a better predictor of Venetoclax sensitivity (Leverson et al., 2017; R. Singh et al., 2019). These ratios could assist in evaluating the potential for backup anti-apoptotic proteins that could block the remaining pro-apoptotic proteins and subsequently evade apoptosis (Leverson et al., 2017).

In order to empirically determine anti-apoptotic dependency in a given cell population a “dynamic BH3 profiling” technique was developed. This technique was established in 2006 (Certo et al., 2006; Fraser, Ryan, & Sarosiek, 2019; Ryan & Letai, 2013), by determining specific anti-apoptotic proteins a cancer cell might depend on and is based on the pattern of the mitochondrial sensitivity using MOMP as a predictive marker (Bock & Tait, 2020; Fraser et al., 2019). A panel of BH3 peptides with characterized binding affinity profiles is used to predict not only the response of cancer cells upon chemotherapeutic drug treatment but also other agents that are capable of priming cells for apoptosis (Certo et al., 2006).

Another way to define anti-apoptotic dependency represents the use of small molecule inhibitors specific for a given anti-apoptotic proteins instead of BH3 peptides. These BH3-mimetics such as Venetoclax (BCL2 inhibitor), S63485 (MCL1 inhibitor) and WEHI-576 (BCL-xL inhibitor), are cell-permeable and dose response curves can be used to determine any specific dependencies within of group of cells or any given cancer types(Konopleva & Letai, 2018; Konopleva et al., 2016; Kotschy et al., 2016; Leverson et al., 2017; Montero & Letai, 2018).

### 4.5.5 Ongoing clinical trials

#### 4.5.5.1 CLL and other cancers

Amongst the B-cell malignancies, CLL was the first one to be sensitive to ABT-737 (BCL2 and BCL-xL inhibitor) and Navitoclax (pan-BCL2 inhibitor; BCL2, BCL-xL and BCL-w), even though CLL did not exhibit amplified BCL2 expression nor translocations (Konopleva & Letai, 2018). Later, Venetoclax was specifically designed as a BCL2-selective inhibitor (100-fold higher specific to BCL1 than BCL-xL). A single dose of Venetoclax caused extensive reductions in tumor burden and showed effectiveness at all administered doses (150-1200 mg per day) (Cassier et al., 2017; Konopleva & Letai, 2018). Venetoclax monotherapy in a phase II open-label study showed promising activity in CLL patients with relapsed/refractory del(17p) chromosome alteration (Roberts et al., 2016). These promising results resulted in a Breakthrough Therapy Designation by the FDA for patients with relapsed/refractory CLL with del(17p), who have received one prior therapy (Cassier et al., 2017; Leverson et al., 2017; Radha & Raghavan, 2017). Various inhibitors for monotherapy are under investigation for CLL patients, but also major strides in establishing efficient combination therapies with Venetoclax are currently being explored. Similar responses were initially seen in Non-Hodgkin lymphoma (NHL). Results from Venetoclax monotherapy and in combination therapy showed some potential in a phase I trial, but the specificity of Venetoclax for t(14;18) translocation-positive NHL was not sufficient to predict response (Leverson et al., 2017; Radha & Raghavan, 2017; Reed, 2017). One of the potential factors responsible for this phenotype was the expression of the anti-apoptotic MCL1, which was frequently co-expressed with BCL2 in cell lines and patient samples suggesting a compensatory mechanism. The combination of Venetoclax with MCL1 modulators such as Dinacicilib, a cyclin-dependent kinase 9 (CDK9) inhibitor showed a potent anti-tumor activity and promising combination strategy (Leverson et al., 2017).

#### 4.5.5.2 AML

AML is a particularly aggressive leukemia and granting the high rate of CR with standard and induction chemotherapy, only 30% for patients achieve long-term disease-free survival. In addition, AML remains largely a disease of elderly, many of whom remain ineligible for chemotherapy-based induction, better options for targeted approaches are required (De Kouchkovsky & Abdul-Hay, 2016). ABT-737 has shown to effectively kill AML derived cell lines, primary AML blasts, progenitors and stem cells, while sparing normal hematopoietic cells. Further analysis using BH3 profiling revealed the differences in mitochondrial priming of myeloblasts and normal hematopoietic stem cells, suggesting its selective efficacy (Konopleva & Letai, 2018; Radha & Raghavan, 2017).

#### 4.5.5.3 Mutational background in BCL2 sensitivity

Based on these preliminary data from ABT-737, BCL2 inhibition was further explored. Two studies reported selective sensitivity to Venetoclax in AML cell lines and murine primary xenograft models, one of them were AML cells with an APL phenotype (Leverson et al., 2017) and the other harboring MLL fusion genes (Pan et al., 2014). In addition, AML cells with *IDH1/2* mutations displayed marked sensitivity to Venetoclax treatment, as mutated IDH1/2 proteins catalyze the production of oncometabolite (R)-2-hydroxygluterate, which can dysregulate mitochondrial functions and induce BCL2 dependency in AML (Papaemmanuil et al., 2016).

In a clinical phase II study launched in 2014, Venetoclax monotherapy was evaluated in patients with relapse/refractory AML. A daily ramp up Venetoclax dosage was administered to achieve as target dose of 800 mg. A total of 32 patients were enrolled with administration of Venetoclax until disease progression or cytotoxicity reached unacceptable levels. A moderate response of 19% CR with a median progression-free survival of 2.5 months was achieved. Response rates were higher in the *IDH1/2* mutation group with about 33% CR, but the response was short-lived (Konopleva et al., 2016).

#### 4.5.5.4 Combination strategies in AML

Although these data clearly indicate the tolerability and relevance of BCL2 inhibition in AML, monotherapy responses with Venetoclax showed limited and short-lived outcomes. This prompted the exploration of combination approaches with currently approved therapies. One of the most promising combination strategies of Venetoclax was performed with hypomethylating agents such as 5-azacytidine (5-aza). 5-aza demonstrated reduction of MCL1 on the protein level, providing a rationale as a good candidate for combination and is approved for the treatment of myelodysplastic syndrome (MDS) and AML for elderly and ineligible patients to standard induction therapy (Konopleva & Letai, 2018). In a phase II study of Venetoclax with 5-aza or decitabine, 145 elderly patients with newly diagnosed AML and who are unfit for standard induction therapy were treated with these combinations. The toxicity profile of the combination was similar to that of HMA agents alone (used as induction therapy). The combination was highly effective with a composite CR rate of 67%, overall survival rate of 83% and median overall survival of 17.5 months. Hence this combination received a FDA Breakthrough Designation in 2017 (Jonas & Pollyea, 2019). In line with the preclinical data, genetic alteration like *TP53* wild-type and *IDH1/2* mutations showed better response (Lin et al., 2020).

Combination of low dose cytarabine with Venetoclax is currently under investigation (NCT03069352) in randomized phase III trial elderly patients with newly diagnosed AML and ineligible for standard induction therapy. Preliminary results from phase II showed a CR rate of 62% and overall survival of 11.4 months (Konopleva et al., 2016). Response was higher in patients from intermediate-risk group compared to adverse-risk group or *TP53* mutations.

Amongst the targeted approaches, combination of Venetoclax with MDM2 inhibitor (Idasanutlin) has shown promising results in a currently ongoing phase Ib trial for relapsed/refractory AML in elderly patients (Cassier et al., 2017). This combination is based on the preclinical work demonstrating that the activation of p53 upon MDM2 inhibition causes subsequent reduction of Ras/Raf/MEK/ERK pathway and proteasomal

degradation of MCL1 in a p53-dependent manner (Pan et al., 2017). An attractive combination in preclinical studies is the combination of BCL1 and MCL1 inhibition, as both act as reciprocal resistance factors for each other, specific potent inhibitors are in pipeline yet to be evaluated clinically.

# 5. Aim of the project

Our hypothesis in the project is to evaluate if AML cells are dependent on anti-apoptotic programs to maintain their high proliferating state. At this stage, when treated with mild dosages of PARPi, cells accumulate DNA damage and become more dependent on anti-apoptotic proteins such as BCL2. Combining PARPi with BCL2i would therefore synergistically induce apoptosis in AML cells.

# 6. Methods

## 6.1 Cell lines and mutational background

In order to address the variability of major driver mutations in AML towards its sensitivity to PARP inhibitors, we used different, well-characterized AML cell lines, established from AML patients. These cell lines have been sequenced for their mutational background and are freely available at online repositories such as, the Catalogue of Somatic Mutation in Cancer (COSMIC database, Cell line project) (Tate et al., 2019), and CCLE database (Broad Institute Cancer Cell Line Encyclopedia) (Barretina et al., 2012). The cell lines used in this project are shown in Table 1. All cell lines were obtained from DSMZ (German Cancer Cell Line Depository), authenticated by Multiplexion (Heidelberg) and regularly monitored for mycoplasma contamination using the Vendor® GeM classic kit (Miverva Biolabs). All the buffer recipes, antibodies and machine used for measurement are list in the Appendix (13).

| Cell lines | FLT3 | TP53 | MLL-fusion | BRCA-2 |
|---|---|---|---|---|
| **HL-60** | wt | mut | wt | wt |
| **THP-1** | wt | mut | MLL-AF9 | wt |
| **NOMO-1** | wt | mut | MLL-AF9 | wt |
| **OCI-AML-2** | TKD | wt | wt | wt |
| **MV4-11** | ITD | wt | MLL-AF4 | wt |
| **MOLM-13** | ITD | wt | MLL-AF9 | Mut |
| **OCI-AML-3** | wt | wt | wt | wt |

***Table 1: AML cell lines with mutational background.***

## 6.2 Cell lines culture conditions

For long term storage cells were kept in liquid nitrogen in a freezing mix solution composed of fetal bovine serum (FBS) with 10% DMSO. For cell culture, aliquots were thawed in a water bath at 37°C for 2-3 minutes and cells were transferred into 15 mL falcon tubes and diluted into fresh media. Cells were then spun down in a centrifuge at 1400 rpm (rotation per minute) for 5 minutes. Remaining supernatant was discarded and the pellet was resuspended into 5 mL of fresh medium with supplements. Suspension cells were plated in 6-well plates at densities between 0.5 and 2 million/ml and placed in an incubator at 37 °C with 5% $CO_2$. All AML cell lines were split and expanded in 1:5 dilutions every 48 hours. Cell culture was maintained for maximal 5 weeks. HL-60, THP-1, NOMO-1, MV4-11, MOLM-13, OCI-AML-3 cell lines were cultured in Roswell Park Memorial Institute 1640 (RPMI-1640) medium supplemented with 10% FBS, 1% L-Glutamine, and 1% penicillin/ streptomycin. OCI-AML-2 cells were cultured in Dulbecco's Modified Eagle Medium (DMEM) with 20% FBS, 1% L-Glutamine, and 1% penicillin/ streptomycin.

Adherent cell lines HEK-293T (293T) and Phoenix (modified 293T cells for retroviral transduction) were cultured in 10 cm culture plates in DMEM with 10% FBS, 1% L-Glutamine, and 1% penicillin/streptomycin. Adherent cells were sub-cultured by decanting culture medium, washing with sterile PBS (phosphate-buffered saline) and incubated with 2 mL of Trypsin-EDTA solution for 3-5 minutes in the incubator. To stop the trypsin reaction 8 mL of fresh medium was added to the culture and cells were counted for re-plating. One million cells were then seeded per 10 cm culture plate and pipetted gently on the bottom of the plate to avoid cell aggregation and clumping. When the cells were 70-80 % confluent, they were subcultured at 1:5 dilution.

## 6.3 Cell line characterization

### 6.3.1 Cell proliferation using Trypan Blue dye exclusion assay

AML cell lines were seeded in a 6-well plate with a density of 10^6 cells per well in a final volume of 5 mL. Every 24 hr cells were resuspended and consecutively 20 µL of cell suspension were mixed in a fresh sterilized reaction tube with 20 µL of Trypan Blue stain (0.04 % final concentration) to a dilution factor of 2. Ten µL of the mixed suspension was added between the cover glass and hemocytometer and all four corners chambers were counted. Trypan blue dye was used to measure proliferation rate, as this assay allows differentiating between live and dead cells; live cells with intact membranes do not absorb non-membrane permeable dyes (such as trypan blue), while dead cells absorb it. Counted average (avg.) number of cells was plugged into the Equation 1 to obtain the number of trypan blue unstained cells (viable cells) per mL of solution. This was repeated for the time points 24, 48, 72 and 96 hrs. For longer time proliferation analysis, cells were split in 1:2 or 1:4 dilution every 3 days depending upon doubling time of cells lines, which differ from each other.

$$\left\{Viable\ \frac{cells}{mL} = Avg.viable\ cells\ \times Dilution\ factor \times 10\text{^}4\right\} \qquad (1)$$

### 6.3.2 Cellular toxicity assay using MTT based metabolic assay

The MTT (3-(4,5-dimethylthiazol-2-yl)-2,5-diphenyltetrazolium bromide) tetrazolium reduction assay measures cellular metabolic activity in the presence of NADPH and reduces yellow tetrazolium salt MTT into purple formazan crystals (Prabst, Engelhardt, Ringgeler, & Hubner, 2017; Vega-Avila & Pugsley, 2011). These insoluble formazan crystals are dissolved using a solubilization buffer and are measured at 570 nanometer absorbance using a multi-well spectrophotometer. The number of viable and metabolically active cells is directly proportional to formation of formazan crystals. In order to measure the effect of inhibitors on the cellular metabolic activity and subsequently measure the cell viability, cells were seeded in density of 0.15x10^6

cells/mL (30,000 cells per well) in a final volume of 200 µL in a flat bottom (F-bottom) 96-well plate. Cells were treated with appropriate concentration of inhibitors and equivalent vehicle control (veh. ctrl) to normalize the response and cell viability was measured for 24, 48, 72 and 96-hour time points. For each time point, 90 µL of seeded cells were transferred into a new F-bottom plate and supplemented with 10 µL of MTT reagent (buffer recipe as described in 13.1.4) and incubated in an incubator maintained at 37 °C with 5% $CO_2$ for 4 hr. Formazan crystals formed during this incubations period were dissolved using 100 µL solubilization buffer and further incubated at 37 °C overnight or 16 hours and measured at 570 nm using multi-well spectrophotometer. Intensity responses from the treated samples were normalized to the veh. ctrl samples to obtain percent viable cells.

### 6.3.3 Cell viability using CellTiter Glo 2.0

CellTiter-Glo® 2.0 (Promega) is an ATP-based cell viability detection kit. It measures the amount of ATP present upon cell lysis and is directly proportional to the luminescence produced upon converting luciferin into oxyluciferin. The ready-to-use reagent contains a mix that lysis the cells and the ATP released from the living cells can be used to measure luminescence using a plate reader without interfering with culture medium or serum. Cells were seeded as described in the earlier section or in a 96 Well Microplates, µClear® (Greiner BioOne) with a final volume of 100 µL and incubated for 72 h unless mentioned otherwise and after incubation 100 µL of CellTiter-Glo solution is added to the wells and incubated in dark at RT for 10 min and measured for luminescence. Alternatively, cells were seeded in 12 or 6-well plates for various time point measurement, and 100 µL of cell suspension was added to 96 Well Microplates followed by equal volume of CellTiter-Glo and measured.

### 6.3.4 High throughput screening (HTS) based cell viability assay measurement

An automated high throughput screening (HTS) was set up using a BD FACS Canto II™ flow cytometry machine . Cells were seeded in a U-bottom 96-well plate at a density of

0.15x10^6 cells/mL (30,000 cells per well) in a final volume of 200 µL. Cells were supplemented with Veh. Ctrl (DMSO at the same final concentration as the amount of DMSO present in inhibitor solutions). Inhibitor stock solutions were prepared in DMSO, and further diluted in PBS and/or culture medium, with a final DMSO concentration below 0.1% in order to avoid adverse effect of DMSO on the cells. The outer wells of the plate were filled with PBS and placed inside the incubator for different time points. In order to measure proliferation using the HTS FACS units, a HTS-measuring plate were prepared with 20 µL of seeded cells in a new U-bottom 96-well plate and supplemented with 180 µL of HTS-buffer (PBS, 2.2mM EDTA, 1 µg/mL DAPI; conceptually similar to trypan blue dye exclusion assay as explained in 6.3.1) to achieve a final volume of 200 µL. HTS-FACS measurement protocol was programmed to mix three times within each well and collect 25 µL from each well for analysis in an automated program to measure all the wells assigned in the software. The output data was processed using FlowJo software (version 10.6.1) with a gating scheme as shown in Figure 12.

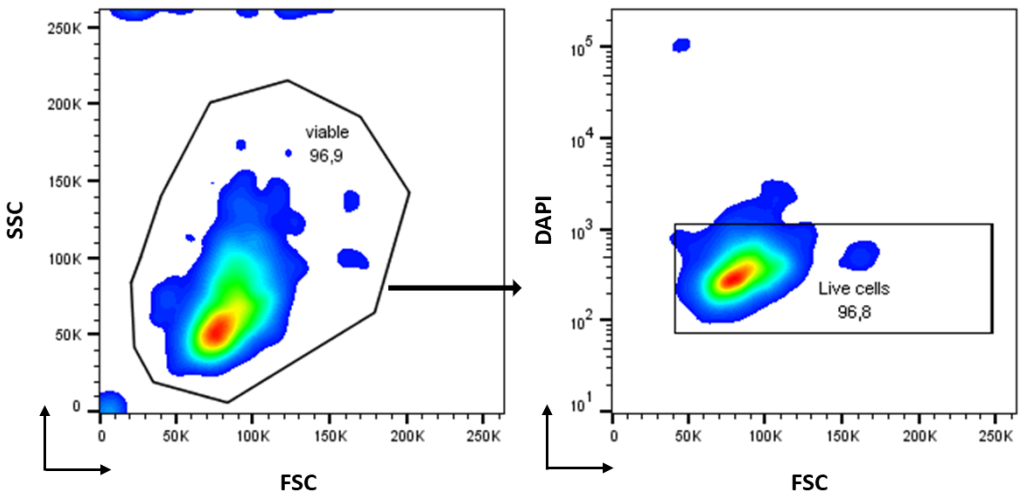


***Figure 12: Cell viability gating scheme for automated HTS analysis. Flow cytometry mediated cell cycle analysis.***

*Flow cytometry plots showing the gating strategy to analyze living cells. The first gating was size selection using Forward Scatter (FCS) and Side Scatter (SSC). A polygon selection area denoting 'Viable cells' were further verified for its DAPI based fluorescence. DAPI negative population of cells denoted as 'Live cells' were quantified as the population of Live cells form the total number of cells measured. The Living cells from the absolute cell number per sample was analyzed using FLOWJO software (version 10.6.1).*

### 6.3.5 Cell cycle analysis

Five hundred thousand cells from each condition either with/without treatments were transferred in a FACS tube and spun down at 1400 rpm and supernatant was carefully discarded. Pellets were washed twice with cold PBS maintained at 4°C, and fixed with 500 µL of cold 70% ethanol and placed in the fridge for 30 min. After incubation, remnant of ethanol was washed out twice with cold PBS and then the cells were permeabilized and stained simultaneously using cell cycle staining buffer (PBS, 0.1% Triton-X, 10µg/mL DAPI) for 30 min in a dark cabinet. Cells were then spun down and washed with PBS and replenished with FACS buffer (PBS, 2mM EDTA and 2% FCS). At this stage, samples can be stored at 4°C for 2-3 hours or measured immediately using a BD FACS Canto II. For each condition 10,000 events were measured. FACS raw files were then gated as 'Viable' population to remove debris from the analysis and cell counts relative to the amount of DAPI incorporation was determined as shown in Figure 13 to plot cell cycle profiles with and without treatment.

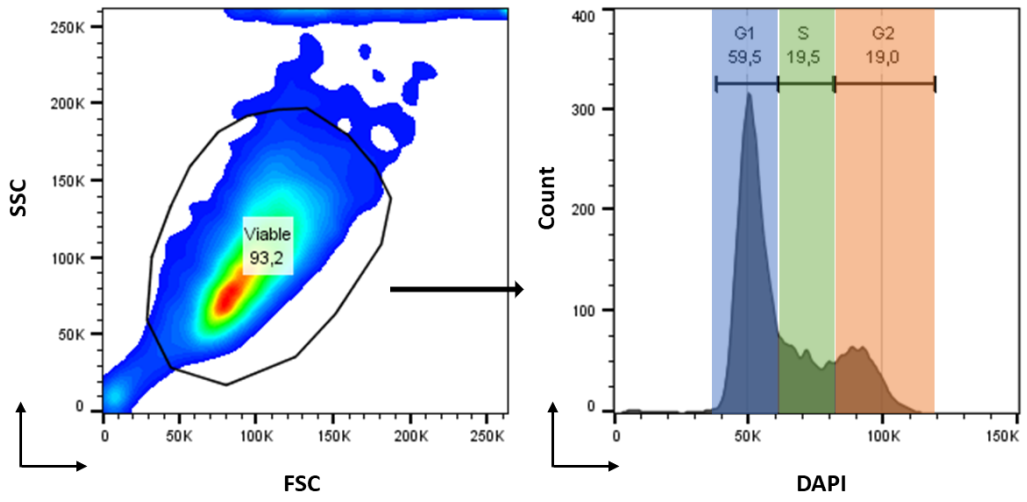


***Figure 13: Cell cycle gating strategy.***

*Flow cytometry plots showing gating strategy for analyzing cell cycle phases. The first gating was size selection using Forward Scatter (FCS) and Side Scatter (SSC). A polygon selection area denoting 'Viable cells' were plotted against their DAPI intensity in order to segregate cells in different cell cycle phases. As these cells were fixed and permeabilized, the amount of DNA content in each cell would be directly proportional to DAPI intensity, thereby enabling cell cycle phase selection.*

## 6.4 Inhibitor dilutions and combination strategies

AML cell lines were seeded in 96-well plates with a density of 0.15x10^6 cells/mL (30,000 cells per well) in a final volume of 200 µL, as specified in earlier sections. In order to define the "effective dose range" of inhibitors for each cell line, cells were seeded with a maximum final concentration of 10 µM and diluted in a 1:2 ratio in the plate itself using a multi-channel pipette (Gilson). Plates seeded with cells were incubated for 24, 48, 72, and 96 hours Proliferation and cell death was analyzed using the DAPI exclusion HTS method and MTT assay as described in the sections above. This information was used to determine inhibition of cell growth relative to untreated controls using Equation (*2)* and/or to extrapolate the fifty percent lethal concertation does (IC50) for each inhibitor with respect to individual cell lines.

$$\%\, Inhibition = 100 \times \left(\frac{1 - (X - MIN)}{(MAX - MIN)}\right) \qquad (2)$$

If X is the response at any given drug concentration, MAX is the concentration with 100 % inhibition and MIN is the concentration with 0 % inhibition. Estimation of effective dose range for each inhibitor is essential in order to find the best combination dosages and to demonstrate synergistic responses but also to eliminate a potential overkill scenario that ends up becoming toxic combinations.

### 6.4.1 Drug combination strategies

Study of bypass mechanisms has given rise to targeted drug combination strategies, that can potentially reduce the toxic effects of either inhibitors alone, while enhancing response compared to single inhibitor treatment (Al-Lazikani, Banerji, & Workman, 2012; Malyutina et al., 2019). This necessitates the validation of combination strategies with respect to synergistic, additive or antagonistic response.

To explore combinatorial responses, effective doses within the IC50 range for each of the inhibitors were used. Dose ranges for each inhibitor starting from twice the IC50

value and diluted 1:2 for each inhibitor and were plated in a combination matrix as shown in Figure 14A. Each experiment was performed in triplicates with a technical duplicate and measured at various time points ranging from 24 to 96 hours.

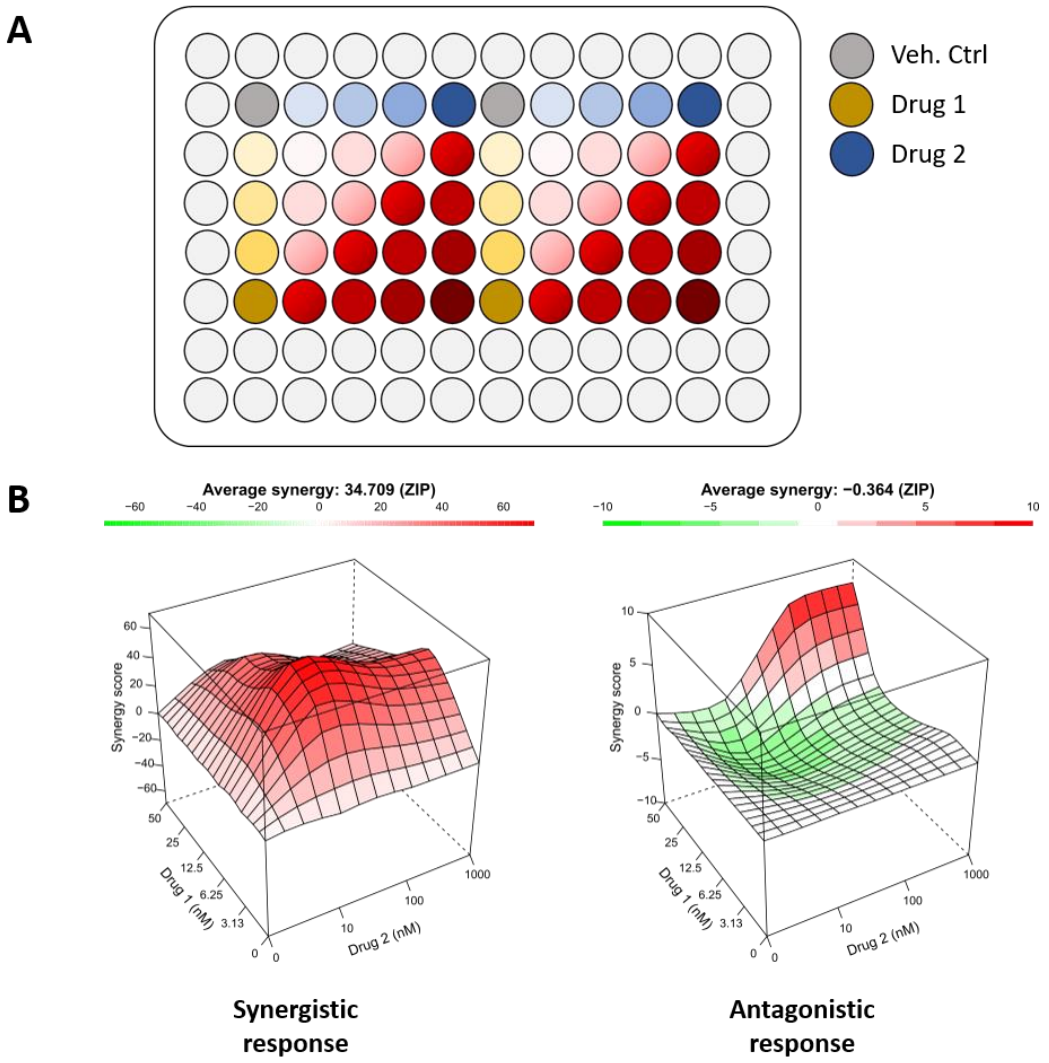


***Figure 14: Drug combination plating strategy and synergy evaluation.***

*(A) Shown is a 96-well plating workflow with single dose response of Drug 1 (yellow) and Drug 2 (Blue) and combination dose matrix (red). Increase in color intensity corresponds to higher drug concentrations. Each of the responses was measured by using either MTT assays or HTS DAPI exclusion assays. The response of single treatment and combinations were normalized to vehicle control (grey; Veh. Ctrl.) to obtain viability or inhibition rates relative to controls. (B) Relative inhibition of growth was further utilized to compute three-dimensional surface plots in order to visualize overall synergy (red) or antagonistic effects upon drug combination using Zero interaction Potency (ZIP) statistical model as described in 8.4.2.*

Upon seeding the cells in a 96-well plate with inhibitors response was measured using HTS-based cell viability and/or MTT assay as described in the earlier section 6.3.

### 6.4.2 Synergy scoring methods and rationale

Data were analyzed with four classical synergy response models: i) Highest Single Agent model (He et al., 2018): expected effect $Y_e$ is the highest monotherapy effect as shown in Equation (*3)*; ii) Loewe Additive model (Loewe, 1953): expected effect $Y_e$ would be when combined with itself as shown in Equation (*4)*; iii) Bliss Independence model : expected effect $Y_e$ would be achieved if the 2 drugs are acting independently of each other as shown in Equation (*5)*; and iv) Zero interaction Potency (ZIP) model : expected effect (BLISS, 1939; Chou, 2006; He et al., 2018; Ianevski, He, Aittokallio, & Tang, 2017; Loewe, 1953).

$$y_e = \max(y_1, y_2) \quad (3)$$

$$y_e = y_1(x_1 + x_2) = y_2(x_1 + x_2) \quad (4)$$

$$y_e = y_1 + y_2 - y_1 y_2 \quad (5)$$

Each of these synergy models computes the degree of which the actual response has deviated from the estimated or expected response based on the core assumption described in the respective equations. For a given drug combination, drug1 at dose $X_1$ and drug2 at dose $X_2$, the effect $Y_c$ of the combination is compared to singe treatment $Y_1(X_1)$ and $Y_2(X_2)$. Normalized responses were then evaluated for synergistic, additive, or no-interaction scenario upon drug combinations based on the deviation in response of a combination pair compared to the expected response $Y_e$ i.e. no-interaction (null hypothesis). Most of the combination plots as represented in Figure 14B were analyzed using ZIP model as the expected value $Y_e$ for such a model would be achieved, if both the drugs do not potentiate each other thereby, substantiating the hypothesis of both Loewe and Bliss models (He et al., 2018).

A workflow of high throughput drug combination was established using 96-well U-bottom plates and cell viability and toxicity assays were performed. This approach could be easily scaled for 384-well plates for multiple combinatorial drug screens not only for cell lines but also primary AML patient samples.

## 6.5 DNA damage quantification

### 6.5.1 Immunofluorescence based DNA damage quantification

Prior to harvesting of treated and control cells, coverslips, slides and fixation reagents were prepared and placed at 4°C. Coverslips (22 mm square coverslips with 1.5 mm thickness) were placed in a 6-well plate and treated with 70% ethanol (Sigma) for 5 min at RT in order to eliminate any contaminants and washed 3X with PBS. Then plates were coated with 1 mL of 1X solution of Poly-L-Lysine (1:10 dilutions from stock, Sigma) for 30 min at RT, washed 3X with PBS and allowed to airdry for 5-10 min. In the meantime, 1X10^6 of cells were transferred into 1.5 mL tubes, washed with cold PBS and resuspended in 100 µL PBS. Fifty microliter of cell suspension were gently dropped on the coated coverslip and incubated at RT for 5 min. Plates were tilted to remove the excess fluid and in order to fix cells, 1 mL of cold 4% PFA (RnD Systems) was added to each of the well and incubated for 10 min at RT. After fixation, coverslips were washed 3X with PBS and permeabilized by adding 1.5 mL of PBS with Triton-X (0.1%) and incubated at RT for 10 min, washed 3X with PBS and blocked with blocking buffer (PBS with 1% BSA,) either 2 hr at RT or overnight at 4°C.

Primary antibodies directed against gH2AX (Cell Signaling, concentrations are shown in Appendix), was diluted in blocking buffer, and adjusted to 100 µL per coverslip/sample. Then 100 µL of primary antibody in blocking buffer was placed as a droplet on each coverslip. After overnight blocking, blocking buffer was discarded and the coverslips were incubated with primary antibody in a humidity chamber at 37°C. After 1 hr coverslips were placed back in the 6-well plates, washed 3X with PBST (PBS with 0.1% Tween-20) and incubated with Alexa 488 secondary antibody (Invitrogen, dilutions as

shown in Appendix) along with Hoechst (1:1000 in blocking solution, Invitrogen, 33342) to counter stain the cell nucleus in the humidity chamber at 37°C for 1 hr. Coverslips were again washed 3X with PBST in 6-well plates and prepared for mounting the slides. A droplet/15 µL of ProLong™ Gold Antifade mounting medium (Thermo Scientific) was used to mount the coverslips on the slides, incubated in dark for 1-2 hr. Slides were stored in dark for 1 week in a slide storage box.

Mounted coverslips were sealed with nail polish before measurement. Images were acquired using Zeiss LSM 710 confocal microscope (Carl Zeiss MircoImaging GmbH.) with a 63X oil objective. Images were acquired by sequential scanning of 405 nm, 488 nm and 561 nm laser stimulation, with a frame size of 512X512 pixels and scanned in a 4X4 tiles and a constant pin hole of 1 AU (airy units) unless mentioned otherwise using a ZEN™ software (Zeiss) to navigate the microscope and save images. Acquired images were processed for foci quantification using Fiji software (Schindelin et al., 2012) and visualized using GraphPad Prism (version 8.01) with each column representing data from 500 cells. Boxplots were used to depict number of cells with more than 5 foci per cell. One-way ANOVA and Student's t-test were performed to measure statistical significance.

### 6.5.2 High Content screening (HCS) – cell cycle mediated multiple staining

For the high content screening, cells were treated in a 6-well plate as described in section 6.3.1, transferred to 15 mL falcons and washed 2X with PBS. Prior to seeding cells in 96-well plates (Pelkin Elmer, CellCarrier-96 Black), wells were coated with Poly-L-Lysine for 30 min and RT and washed 2X with PBS. Cell density was adjusted to 10^6 cells/mL and 100 µL were transferred into the pre-coated wells. The plate was centrifuged in a gentle pulse for 20 sec at 500-800 rpm. Equal volume of 8% PFA was gently added to the wells using a multi-channel pipet (Glison), fixed for 10 min at RT and washed 3X with PBS. Fixed cells were permeabilized by adding 100 µL of PBS with Triton-100 (0.1%) into the wells and incubated for 30 min at RT and washed 2X with PBS and further blocked for 30 min with cold PBS with 3% BSA (blocking solution). After incubation, the blocking solution was discarded, and cells were incubated with 100 µL

of primary antibody prepared in blocking solution (primary antibodies and dilutions as described in Appendix) overnight at 4°C. For overnight incubation, plates were sealed with paraffin strips to minimize vapor formation within the plates. Next day, primary antibody was gently removed with a multi-channel pipet, washed 2X with 200 µL of PBS-T (0.1% Tween-20) with a 3 min incubation period between each washing step. Then cells were incubated with 100 µL of secondary antibodies (dilutions as described in Appendix) prepared in blocking solution for 1 hr at RT in dark. Secondary antibodies were discarded after incubation, cells were washed 3X with PSB-T and incubated with Hoechst staining solution (1:2000 in PBS, Invitrogen, 33342) for 20 min at RT in dark in order to stain the cell nucleus and measure differences between cell cycle phases. After incubation, staining solution was discarded, and cells were washed 2X with PBS and left suspended in PBS until analysis using Opera Phenix™ High Content Screening system. An overview of the workflow is shown in Figure 15.

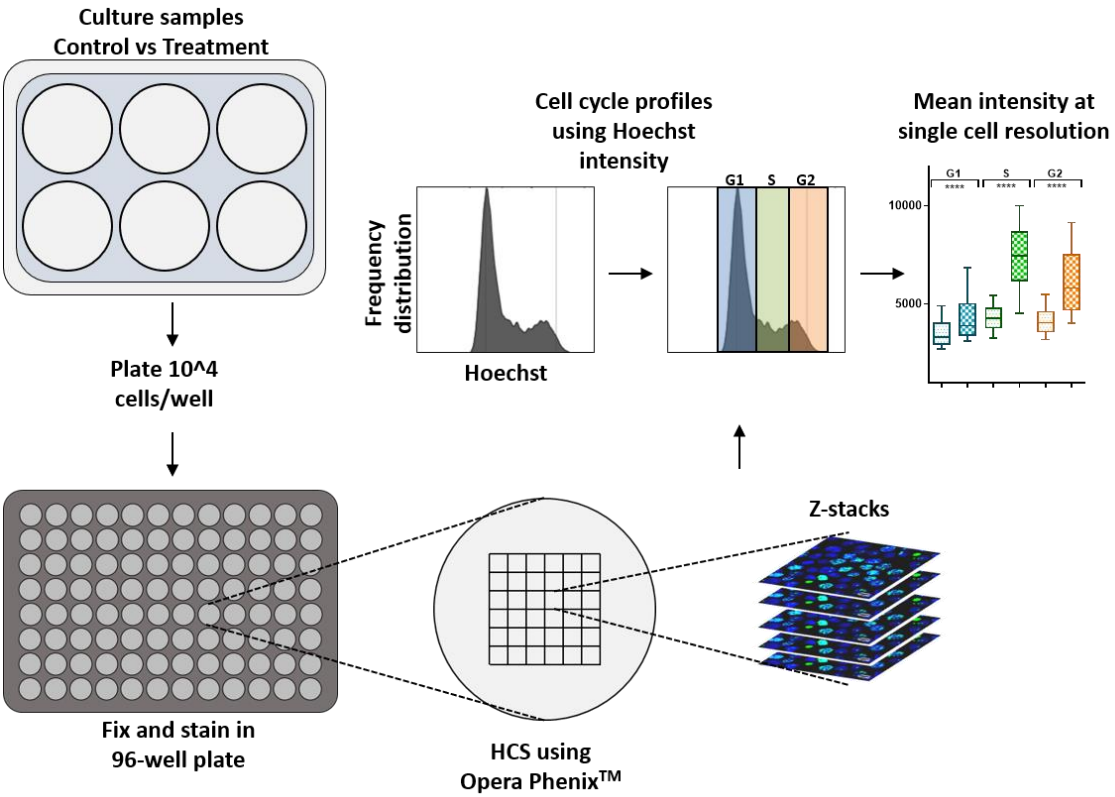


***Figure 15: High Content screening workflow.***

*A schematic representation of High content screening (HCS) using OperaPhenixTM. Cells were cultured and treated in 6-well plates. Ten thousand cells were seeded in each well, fixed and stained with specific antibodies against specific markers e.g. gH2AX or 53BP1. After secondary antibody incubation, cells were incubated with Hoechst stain for 20 min at RT. Plates were placed for measurement into OperaPhenix™ machine and different cell profiles were established for each cell line, for instance, region of interest , channel intensities, Z-stack range, etc. After measurement, data were analyzed using Harmony software (Pelkin Elmer) using a frequency distribution plot and cells were annotated based on their cell cycle phases. Expression of defined markers like gH2AX can further be quantified in a cell cycle dependent manner.*

Images were acquired and pre-processed using Harmony High Content Imaging and Analysis Software (version 4.4, PerkinElmer). Images were acquired using a 20X air objective to measure differences in a cell cycle-dependent manner based on measured fluorescence intensity obtained from Hoechst staining. On the other hand, a 40X objective was used to quantify foci using spot detection within the selected region of interest marking nuclei of the cells. Around 20-30 regions were selected from each well excluding the peripheral regions of the well. Images acquired in 3-5 Z-stacks from each region, which were superimposed into a projected image for each region after analysis.

Cells in the periphery of the projected images were excluded from the analysis and flat-field correction was applied to correct the illuminations from non-flat cells. Mean and sum of measured fluorescence intensities from each of the images in a single cell resolution were exported from Harmony to be further processed using GraphPad Prism (version 8.3). To visualize the cell cycle-depended changes in DNA damage (for example gH2AX) in a single cell resolution, a scatterplot was used with X-axis values as sum intensity of Hoechst/DAPI and Y-axis values of mean intensity of gH2AX as shown in Figure 15 (Michelena & Altmeyer, 2017; Roukos, Pegoraro, Voss, & Misteli, 2015). To quantify the changes within each cell cycle phase upon treatment, 5,000 cells in each condition were plotted in boxplot displaying interquartile ranges with medians and whiskers of each column were represented as 5-95% or 10-90% of the total population on the plot, but included in the analysis for One-Way ANOVA, Students T-test and Tukey test for statistical significance.

### 6.5.3 Neutral Comet assay

To measure DNA damage accumulation within each cell, neutral comet assay was performed. Cells were seeded in a 6-well plate as described earlier at different time-points. For the assay, cells were collected in 15 mL falcons and washed 2X with cold PBS, resuspended in PBS, counted, and adjusted to a cell density of 2X10^5 cells/mL concentration in a 1.5 mL eppendorf and placed on ice. In the meantime, 1% Low Melting Point (LMP) agarose was prepared in PBS and aliquoted in 1.5 mL eppendorf tubes and placed on a heating block at 50°C to avoid re-solidifying of agarose. Empty 1.5 mL tubes were pre-warmed in a heating block before adding 70 µL of 1.5% LMP and 70 µL of cell suspension in tubes and were gently mixed using a pipet tip without vortexing the tubes. A glass plate was placed on ice and microscopy slides were cooled on top of the glass plate. Once the samples are mixed in LMP solution, 120 µL of the suspension solution with cells were dropped carefully on the pre-cooled slides and long coverslips (24X50 mm, Melzer) were carefully placed on top of the LMP-cell suspension and cooled at 4°C for 5 min. The coverslip was carefully removed without disturbing the solidified LMP-cell suspension layer and then 100 µL of 0.5% LMP solution was added

on top and coverslip was placed on top again to embed the cells in final 0.5% LMP agarose layer and cooled at 4°C for 10 min. After both layers were solidified the coverslips were removed and the slides were placed in an agarose gel electrophoresis chamber with an overnight pre-cooled Lysis Buffer (recipe in Appendix) for 2 hr. This and all following steps were performed in a cold room in a light sensitive manner. After 2 hr of incubation, slides were transferred in a slide jar with Neutral Electrophoresis Buffer for 30 min and then placed on a paper towel, Meanwhile the electrophoresis unit was prepared by adding 1X Neutral Electrophoresis Buffer just enough to immerse the slides. Electrophoresis was run with a standard condition of 1 V of constant voltage for 45 min unless mentioned otherwise. Slides were then briefly dried on a paper towel and placed in a glass slide jar with DNA Precipitation Buffer (recipe in Appendix) at RT for 30 min and washed once in dd$H_2O$ and then fixed in 100% methanol at RT for 20 min. Once fixed, the slides were placed on a paper towel and allowed to dry at RT for 2 hr in the dark. Air-dried slides were finally stained using 45 µL of PI-staining solution and long coverslips were placed on top. Slides at this stage were either stored in a slide box for a week or analyzed immediately using a Zeiss 710 confocal microscope.

Images were acquired using a 25X objective lens upon 561 nm laser excitation, with a frame size of 512X512 pixels scanned in 4X4 tiles and a max. pin hole size using a ZEN™ software (Zeiss) to navigate the microscope and save images. Acquired images were processed for comet tail length using ImageJ software (version 1.52) and visualized as barplots and dotplots using GraphPad Prism (version 8.3) with each column representing tail lengths of 100 cells depicting the overall accumulation of damage.

## 6.6 Stable cell line generations and validation

### 6.6.1 Short-hairpin RNA (shRNA) plasmid preparation

#### 6.6.1.1 shRNA design and selection

Stable knock-down of a gene of interest was carried out using the shRNA approach. The shRNA sequences required in this project were obtained from Genetic Perturbation Platform (GPP) web portal and cross-referenced for the specificity of the target

sequence by uploading the sequence to ENSEMBL genome browser (Hunt et al., 2018). Target sequences were aligned to Genome reference Consortium Human build 38 (GRch38) using the BLAST tool to evaluate the potential off-target alignments of the sequence. Alternatively, new primers were designed using NCBI Primer Design guidelines (Ye et al., 2012) and highest scoring target sequences were ordered (Biomers GmbH.) for cloning them into plasmid vectors. The shRNA sequences used in this project are listed in Appendix 13.1.6.

#### 6.6.1.2 shRNA sequence assembly and plasmid preparation

The target shRNA sequences were cloned in pLKO-TET-ON vector (gift from Dmitri Wiederschain, Addgene plasmid #21915), which is a doxycycline (DOX)-inducible vector system and along with packaging and envelop vectors stable lentiviral particles can be produced (as described in Transfection and transduction section). The pLKO-TET vector was first linearized by digesting with AgeI (40 Units, NEB) and EcoRI (40 Units, NEB) restriction enzymes generating sticky ends with non-complementary overhangs. A mixture of 4 µg of pLKO-TET vector in 1X NEB Buffer (Buffer 2.1) in a final volume of 100 µL in a 1.5 mL eppendorf tube and incubated for 2 hr at 37°C in a heating block. Agar gel loading dye (NEB) with EDTA was added to the reaction mixture to stop the enzymatic reaction and was loaded onto a 1% (weight/volume) agarose gel prepared in TAE buffer using an agarose gel electrophoresis units and filled up with 1X TAE buffer. The reaction was run for 1 hr at 130 V to separate undigested vector from the linearized vector and the restriction digested product. The gel was run in reference to agarose gel running ladder and control reaction without restriction enzymes to differentiate between digested and non-digested vectors.

After running the gel, a piece of agarose gel at 10 kb (kilobase) containing the digested vector was transferred into a 1.5 mL reaction tube and the digested product was recovered using Agar Gel Extraction kit (Qiagen).

In parallel, shRNA target sequence both sense and anti-sense sequences were prepared for an annealing step. The ordered sequence in lyophilized powder was suspended in a

nuclease-free $H_2O$ to obtain a final concentration of 100 pmol/µL (100 µM) stocks and 10 µL of each sense and anti-sense sequences were mixed in a PCR tube and placed in a Thermocycler for the annealing step as shown in Table 2.

| Cycle step | Temperature | Ramp rate | Time |
|---|---|---|---|
| **Initial denaturation** | 95°C | | 5 min |
| **Annealing** | 95-85°C | -2°C/sec | |
| | 85-25°C | -0.1°C/sec | |
| **Hold** | 4°C | | |

***Table 2: shRNA annealing step using ramp setup in a thermocycle***

After the annealing step, sequences were diluted 1:50 in nuclease-free $H_2O$. Annealed sequences were designed to create overhangs complementary to AgeI and EcoRI digestion pLKO-TET vector and were immediately used for the ligation step using the TAKARA kit (TAKARA Bio Inc.). Two µL of annealed sequences were mixed with 20 ng of digested vector in a fresh PCR tube and 5 volumes of Reagent A and 1 volume of Reagent B was added to the mixture and incubated either 1 hr at RT or overnight at 16°C. The total ligation mixture was used to transform the DH5α bacteria strain (Invitrogen) for mass production of the vector with its target sequence, plated on agar plates with ampicillin (Carl Roth) for positive selection of transformed bacteria and incubated at 30-32°C in a bacterial incubator overnight. Single clones were carefully picked from the plate and pre-cultured in 5 mL of LB medium with ampicillin at 32°C in a bacterial incubator at 250-300 rpm for 2 hr, expanded to a final volume of 25 mL and continued incubation overnight. After the overnight expansion, 100 µL of bacterial culture was mixed with 100 µL of 87% Glycerol (Sigma) and stored at -80°C for backup and the rest of the culture was pelleted and vector was extracted from the bacteria using MIDI-preparation kit (Qiagen) as per the recommended instructions.

### 6.6.2 Transfection and transduction

#### 6.6.2.1 Transfection

In order to produce virus supernatants for an efficient and stable expression of shRNA in AML cell lines, 293T cells were transfected using TransIL-LT1 reagent (Mirus). 293T were seeded in 10 cm petri-plates with a seeding density of 10^5 cells/mL, 30 hours prior transfection to achieve 60-70% confluence. Four hours prior transfection, the culture medium was gently removed from the plate and carefully replenish with 6 mL of fresh culturing medium without antibiotics (penicillin/streptomycin). For transfection, TransIL-LT1 transfection reagent was diluted in OptiMEM™ (GIBCO) and 20 µL of reagent was added to 280 µL of OptiMEM per 10 cm culture plate in an eppendorf tube and incubated at RT for 5 min. In the meantime, the plasmid mixture was prepared in a new eppendorf tube as shown in **Table** 3.

| **Reagents** | **concentration per 10 cm plate** |
|---|---|
| **Packaging plasmid (pSPAX.2)** | 1.8 µg |
| **Envelope plasmid (pMD2.G)** | 300 ng |
| **Expression vector (shRNA)** | 3 µg |
| **OptiMEM™** | 20 µL |

***Table 3: Plasmid mixture for transfecting 293T cells***

After 5 min incubation, the plasmid mixture was added to the transfection reagent mixture and incubated at RT for 20 min. The whole mixture pipetted into the 10 cm plate with 293T cells, gently shaken and placed back into the incubator for 16 hr. After 16 hr/overnight incubation, the medium was carefully removed from the plates and replenished with 4 mL of fresh medium with 30% FCS without antibiotics and incubated in the incubator for 30 hr. After 30 hr incubation, the supernatant was collected from the plates in a 15 mL falcon and cells were discarded. After spinning down the supernatant, the virus supernatants were aliquoted in 1 mL per NUNC tubes and store

at -80°C for later use. Alternatively, supernatants were used immediately for AML cell transduction.

#### 6.6.2.2 Lentiviral transduction of AML cell lines

Prior initiating transduction, AML cell lines were split 1-2 days before in a 1:2 to 1:5 dilution to get them in proliferating phase. On the day of transduction, 10^6 cells were seeded in a 6-well plate (Starstedt) with a final volume of 3 mL. One milliliter of frozen or freshly collected virus supernatant was added to the respective wells along with polybrene (Sigma) at a final concentration of 8 mg/mL (check-conc). 6-well plates were sealed with micro-permeable membrane tape to avoid contamination and placed in the centrifuge for spinfection at 2,500 rpm for 1 hr 45 min at 25°C. After the spin down, plates were placed back in the incubator and maintained at 37°C for 16-20 hr/overnight. After overnight incubation with virus supernatant, cells were spun down in a 15 mL falcon at 1,400 rpm for 5min and the supernatant was replaced with fresh medium supplemented with Puromycin (Sigma, 1 µg/mL final concentration) and placed back in the incubator for 2-5 days for selection of positively transduced cells. Non-transduced cells served as a positive control for selection efficacy. Selection time for the positive population was based on complete cell death of control cells. Depending on the time of selection and efficiency of positive clones, virus titer for dilution was determined and optimized for each of the cell lines.

### 6.6.3 Real time quantitative polymerase chain reaction (RT-qPCR)

Total RNA from cells was collected using High Pure RNA Isolation kit™ (Roche) as per the manufacture's recommendations. Complementary DNA (cDNA) was synthesized from total RNA extracted using RevertAid™ H Minus cDNA synthesis kit (Thermo Scientific) as per the manufacture's recommendations. Concentration of extracted RNA was measured using NanoDrop™ after thawing on ice or freshly extracted and used immediately, but always placed on ice until used. Samples were prepared for cDNA synthesis in a nuclease-free PCR grade 500 µL eppendorf tubes as shown in Table 4.

| **Step 1** | |
|---|---|
| **Template RNA** | 500 ng |
| **Oligo(dT)$_{18}$ primer** | 1 µL |
| **Nuclease-free water** | Up to 12 µL |
| **Total Volume** | 12 µL |
| **Step 2** | |
| **5X Reaction buffer** | 4 µL |
| **RiboLock™ RNase inhibitor (20 U/µL)** | 1 µL |
| **10 mM dNTP Mix** | 2 µL |
| **RevertAid™ reverse transcriptase (200 U/µL)** | 1µL |
| **Total Volume** | 20 µL |

***Table 4: Total RNA template preparation***

Samples prepared as shown in Step 1 were placed in a Thermocycler for incubation at 65°C for 5 min and cooled back on ice. A master mix of reagents from Step 2 was prepared and added to tubes, mixed gently, centrifuged and placed back in the thermocycler and incubated at 42°C for 1hr, followed by 70°C for 5 min to terminate the reaction. The resulting first strand cDNA synthesized was diluted 1:5 (80 µL of nuclease-free water to 20 µL of synthesized cDNA) and either stored at -20°C for later use or immediately used for PCR or qPCR reactions.

To validate shRNA-mediated knockdown efficiency of the gene of interest and/or changes in the expression of transcript levels upon drug treatments, a reaction mixture was prepared as shown in Table 5 using the LightCycler® 480 SYBR Green I Master mix kit (Roche) plated in qPCR-optimized microplates and run in a qPCR thermocycler. Cycle condition for the initial denaturation step used were 95°C for 10 min to activate the reaction, followed by 40 cycles at 95°C for 15 sec as a denaturing step and 60°C for 1 min as an annealing/extension step as shown in Table 5.

| Reagents | Volume |
|---|---|
| **Forward Primer (10 µM)** | 1 µL |
| **Reverse Primer (10 µM)** | 1 µL |
| **Synthesized cDNA template (1:5 diluted)** | 5 µL |
| **Lightcycler® 480 SYBR Green I master mix (2X)** | 10 µL |
| **Nuclease-free water** | 3 µL |
| **Total Volume** | 20 µL |

***Table 5: Components for RT-qPCR reaction***

Forward and reverse primers were designed as described in (Livak & Schmittgen, 2001) for the gene of interest. GAPDH was used as reference gene and normalization of expression levels of the gene of interest amongst the treated samples or control samples in case of knockdown efficiency. The fold change of expression of the gene of interest compared to the reference gene was evaluated based on the threshold cycle ($C_T$) value obtained and normalized using Equation (*6)* .

$$R = 2^{\Delta C_t} = 2^{(C_T Sample - C_T reference\ gene)} \qquad (6)$$

### 6.6.4 Western immunoblotting

#### 6.6.4.1 Preparation of whole cell lysates

For validation of shRNA-mediated knockdown efficiency or verification of the effects drug treatments, 1-5x10^6 cells from each condition were collected, washed twice with cold PBS and resuspended in 100 µL of RIPA buffer (recipe as shown in Appendix). Cells were transferred into a 1.5 mL reaction tube and placed on ice to lyse cells for 15-20 min. RIPA buffer was supplemented with a cocktail of protease and phosphatase inhibitors (1:25 of Complete™ protease inhibitor, 1mM of $Na_3VO_4$, 5 mM of NaF and 5 mM of ß-glycerophosphate). After incubation, whole cell lysates were collected by spinning down the cell debris in a benchtop centrifuge maintained at 4°C at 13,000 rpm for 20 min and the supernatants were transferred into a new eppendorf . Whole cell

lysates were directly used for immunoblots, immunoprecipitation assays or shock-frozen by immersing carefully into liquid nitrogen (N2) and stored at -80°C.

#### 6.6.4.2 Bradford assay for protein concentration measurement

Protein concentration was measured prior to loading the samples on the SDS-polyacrylamide gel and separating them according to their molecular weight. Bradford assay was used to measure colorimetric changes when protein molecules in whole cell lysates bind to Comassie Brilliant Blue stain under an acidic condition, converting red colored stain into blue. A colorimetric photometer was used to measure absorbance at 595 nm. One microliter of lysate was added to 800 µL of dd$H_2O$ and 200 µL of Bradford solution in a cuvette, gently vortexed and incubated at RT for 5 min. The absorbance measured was normalized against a standard curve to obtain protein concentration in µg of total protein per µL of protein lysate.

#### 6.6.4.3 SDS-PAGE gel preparation and running

SDS-PAGE gels were generated in two stages with the bottom section representing the resolving gel and the top section the stacking gel. The difference in the gel composition allows to initially condense the lysates at the start of the gel run and once the proteins enter the resolving gel, they proteins are further separated based on the charge and size/molecular weight of the proteins . The pore size of the resolving gel was adjusted to optimize segregation of the protein of interest (POI): 6-8% of SDS gels for segregating heavier proteins, e.g. 150-300 kDa (kilodalton) and 12-15% gels for lighter proteins, e.g. 10-30 kDa. As a standard a 10% resolving gels was used unless mentioned otherwise.

Once the concentration of proteins was adjusted amongst the samples of interest using the Bradford assay, sample volumes equating to 70 µg were heated in 4xLaemili buffer supplemented with ß-mercaptoethanol (20%) or DTT (1mM) at 95°C for 5min. Samples were loaded on a 10% SDS gel, placed into the electrophoresis unit filled with running buffer and run at 100-150 V for 2hr.

After the electrophoresis, the gel was removed from the glass cassette and transferred on a bed consisting of a sponge and 3 layers of whatman filter paper and put in a tray

in transfer buffer. A nitrocellulose membrane was placed on top of the gel, followed by a similar layer of 3 whatman filter paper and a sponge at the top, making sure to avoid bubble formation at each step. This whole construction was then placed in the transferring unit filled with transfer buffer and run at 20 V for 16-20 hr or overnight.

#### 6.6.4.4 Membrane blocking and development

After overnight transfer the nitrocellulose membrane was washed in 1xPBS on a membrane shaker unit at 50 rpm for 5 min at RT, in order to remove any traces of methanol of the transfer buffer. To check for equal loading and to stabilize the membrane-protein binding, the membrane was stained with Ponceau solution (concentration). Ponceau stained membranes were washed with dd$H_2O$ until the staining solution was removed. Then the membrane was blocked with PBS-T in milk buffer (Tween20™ reagent, 0.1% and milk, 5% weight/volume) on the shaker for 1 hr, washed trice with PBS-T on a shaker for 5 min each round, followed by a second round of blocking with NET-G buffer (recipe as shown in Appendix) for 1 hr on the shaker. After membrane blocking, the membrane was incubated with primary antibody directed against the POI either for 1 hr at RT or overnight at 4°C. Primary antibodies were diluted in NET-G buffer as per the manufacture's recommended dilutions unless mentioned otherwise (an antibody list along with working dilutions are shown in the Appendix). Membranes were washed trice with PBS-T on a shaker and incubated with a secondary antibody conjugated with horseradish peroxidase, diluted in PBS-T for 1hr at RT. After incubation, the membrane was washed trice with PBS-T to remove the excess of un-specifically bound secondary antibody and briefly treated with enhanced chemiluminescence (ECL™, ThermoFischer Scienfitic) substrate solution followed by measuring the signal using a chemiluminescence Imager. The signal of the POI was normalized to the signal of the housekeeping proteins such as GAPDH or ß-Actin.

## 6.7 Cell apoptosis and differentiation measurement

### 6.7.1 Apoptosis

The efficacy of drug effects on cell lines was measured by cell viability and cytotoxicity assays as described in the earlier sections. These assays were extremely proficient in differentiating dead cells against viable cells and hence highly essential for performing high-throughput analyses. On the other hand, these assays lack detecting dying cells, that can be mainly divided in two stages, early apoptotic and late apoptotic stages. Early apoptotic cells flip their phosphatidylserine of the plasma membrane from the inner membrane to the outside and expose it to the surface. Annexin-V protein that specifically binds to phosphatidylserine in presence on $Ca^{2+}$ can be used as a biomarker for cell in the early apoptotic stage. In order to measure the percentage of cells entering apoptosis, an Apoptosis Detection Kit™ (BD Biosciences) was used. Co-staining with Annexin-V and 7-AAD was used to quantitatively measure the fraction of cells entering into early stage (Annexin-V positive, 7-AAD negative) versus late stage apoptotic cell deaht (Annexin-V positive, 7-AAD positive) cells as shown in Figure 16.

AML cell lines and primary samples were treated in 6-well plates with a final cell density of 2x10^5 cells/ mL. 500 µL of cell suspension was transferred into a FACS tube and washed with PBS twice and resuspended in 1x Binding buffer with Annexin-V staining antibody coupled with PE and 7-AAD (1:100 dilution) provided within the detection kit. Cells were gently vortexed and incubated at RT in dark for 15 min. After incubation, 300 µL of 1x Binding buffer was added to tubes and measured using BD FACS Canto II™.

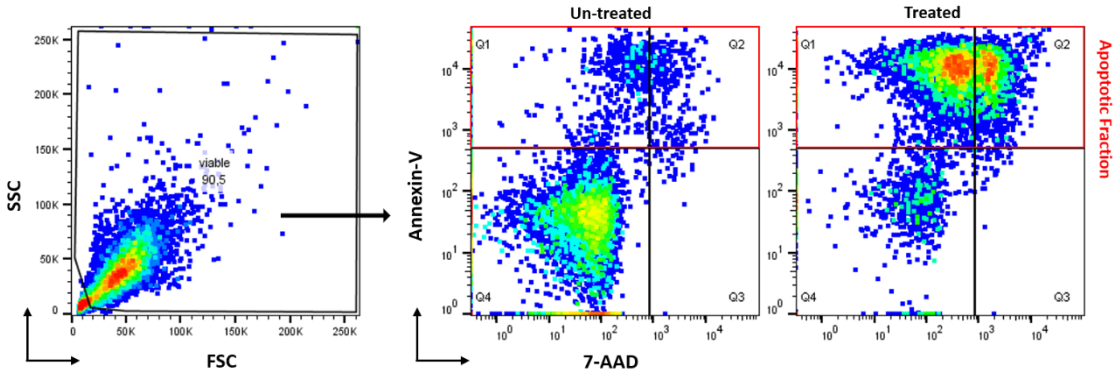


***Figure 16: Gating strategy for measuring apoptotic cells.***

*Flow cytometry plots showing gating strategies for measuring Annexin-V expression and 7-AAD staining. Cells were gated using FCS against SSC. Upon exclusion of cell debris, Annexin-V conjugated with PE stain and 7AAD staining was analyzed. Cells positive for Annexin-V-PE were considered as early apoptotic cells and cells double positive for Annexin-V-PE and 7AAD as late apoptotic. Both fractions together were annotated as 'Apoptotic Fraction'. Percent of apoptotic cells was quantified and further compared to sample control using FlowJo software.*

The population with Annexin-V positive and 7-AAD positive were added up to obtain the 'Apoptotic Fraction' of the total population. Percent apoptosis was calculated by normalizing the apoptotic fraction in treated conditions compared to the control condition.

### 6.7.2 Myeloid-monocytic differentiation measurement

CD11b is a cell surface marker of myeloid-monocytic differentiation (J. Fang et al., 2017). A CD11b surface-marker staining antibody (Biolegend) was used to determine differentiation upon treatment with different drugs. Cells were seeded in the same manner as described in 2.7.1. 500 µL of cells were collected in a FACS tube and washed twice with PBS, resuspended with PBS containing the CD11b-PE antibody (1:100 dilution) and incubated in dark for 20 min. After incubation, cells were spun down and resuspended in PBS and measured using the gating strategy depicted in Figure 17. Percent of differentiated cells were calculated in the same manners as described above for apoptotic cell death.

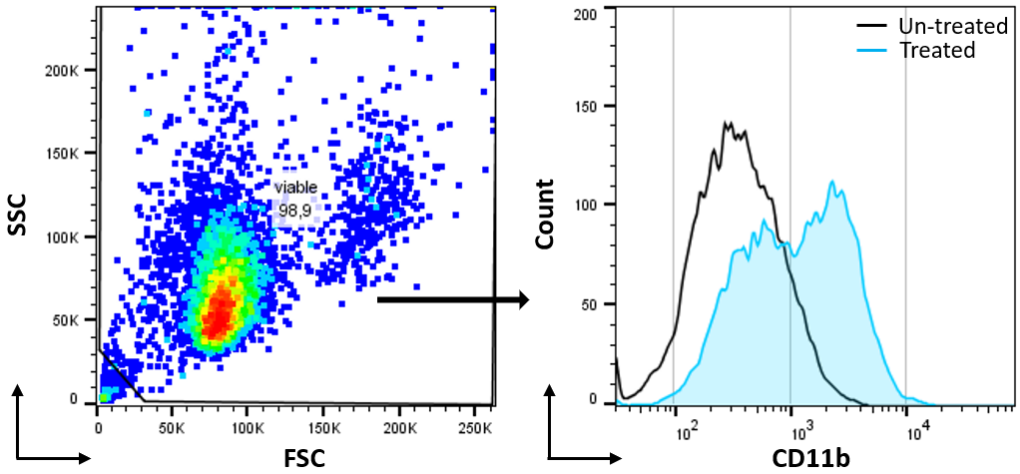


***Figure 17: Gating strategy for measuring cell differentiation.***

*Flow cytometry plots showing the gating strategy to measure the expression of the cell differentiation marker Cluster of differentiation (CD11b) conjugated with APC and percent of differentiation was analyzed using FlowJo software.*

Cells entering differentiation were also analyzed by May-Grünwald Giemsa staining, in order to visualize the change in morphology. Treated cells were washed once with PBS and 8-10 µL of the cell suspension was resuspended in PBS and spread on a microscopy slide. After air drying at RT for 5-10 min, slides were immersed in a ready to use, May-Grünwald staining solution (Applichem GmbH.) for 10 min at RT. Then, slides were washed 2X with water to remove excess stain from the slides and immersed in a Giemsa staining solution (1:10 diluted in water, Merck GmbH.) and incubated at RT for 15-20 min. Slides were washed once in water, air dried at RT and imaged using a light microscope (Olympus).

## 6.8 Primary sample culturing and combination treatment

To validate drug effects observed in cells lines, primary AML samples with heterogeneous mutation profiles were analyzed. Informed consent was obtained from all patients and the study was performed according to the approval of the ethic committee. The mononuclear cell fraction was extracted using Ficoll-Hypaque™ density gradient cell type separation method (Fuss, Kanof, Smith, & Zola, 2009). Mononuclear cells were carefully isolated, counted, and frozen in cryo-vials and stored in liquid

nitrogen tank for later use. To initiate the combination treatments, respective primary samples were thawed in IMDM (Iscove's modified Dulbecco's medium, GIBCO) medium supplemented with 20 % FBS (Corning) and DNAse I (100 µg/ml). Cells were pelleted with a gentle spin-down at 800 rpm for 10 min and the supernatant was carefully discarded. Cell pellet was washed once with PBS and resuspended in IMDM medium without FSC.

### 6.8.1 Methyl-cellulose based Colony forming unit assay

Colony forming potential of primary cells was evaluated using a methylcellulose-based method. Human Methylcellulose complete media™ supplemented with cytokine (R&D Systems, HSC003) was aliquoted and stored at -20°C. Before use, methylcellulose aliquot was thawed at RT. Primary AML cells were counted and resuspended in Cell Resuspension Medium™ (IMDM medium, 50% FCS) with a density of 30,000-50,000 cells in 100 µL of resuspension medium. cells were then added to 3 mL of methylcellulose using a syringe (16-gauge 1½ inch needle) and gently mixed before seeding 1 mL into wells of 12-well plate or alternatively in a single 30 mm petri-dish. Plates/dishes were then placed in the incubator at 37°C for 7-14 days, with replenishing medium every 4-5 days to avoid excessive evaporation from the plates/dishes. At days 7 and 14, number of colonies were counted using a microscope (Frisch & Calvi, 2014).

### 6.8.2 Liquid culture based primary samples

Primary cells obtained from AML patients were seeded with inhibitors and vehicle control in a 24-well plate (Starsted) with a density of 10^6 cells/mL. Cells were cultured with serum-free medium supplemented with 15% BIT (bovine serum albumin, insulin, transferrin; Stem Cell technologies 09500) along with reagents, inhibitors and cytokines to maintain the leukemic stem cell state as described in Table 6 (Pabst et al., 2014).

| Reagents | working concentration |
|---|---|
| BIT (bovine serum albumin, insulin, transferrin) | 15 % |
| Penicillin/Streptomycin | 1 % |
| ß-Mercaptoethanol | 1 µM |
| StemRegenin 1 (Selleckchem S2858) | 1 µM |
| Human Stem cell factor (h-SCF) | 100 ng/mL |
| Human FLT3-Ligand (h-FLT3-L) | 50 ng/mL |
| Human interleukin 3 (h-IL-3) | 20 ng/mL |
| Human Granulocyte colony-stimulating factor (h-G-SCF) | 20 ng/mL |

***Table 6: Supplement list for primary AML patient samples***

Primary cells were treated with drugs for 3-5 days in the plate and viability was determined using the Cell Titer Glo 2.0 assay (Promega), the Annexin-7AAD apoptosis kit and CD11b expression.

## 6.9 Statistical analysis

Data were presented with mean ± standard deviation. For image analysis, all the images were post-processed in ImageJ software with auto-adjustment of brightness and contrast. Statistical significance between different groups was evaluated using One-way ANOVA and Student's t-test using Welch's correction and Tukey test unless mentioned otherwise. Indicated p-values within the graphs denote as follow, **** indicate p-value <0.0001, *** indicate p-value <0.001, ** indicate p-value <0.01, * indicate p-value <0.05 and 'ns' indicate not significant. Statistical analysis was performed using GraphPad Prism software (version 8.4).

# 7. Results

The success of PARP inhibitors in various cancer models, demonstrated by FDA (Food and drug administration) approval in breast and ovarian cancers in germline BRCA1/2-mutated and/ HER2-negative background (S. E. Caulfield, C. C. Davis, & K. F. Byers, 2019) and many late stage clinical trials in various cancer models, argues to evaluate its relevance also in AML. In homologous deficient cancer, inhibition of PARP causes a phenotype termed “synthetic lethality”. BRCA1 and BRCA2 play an essential role in the repair of DNA double strand breaks (DSB) via homologous recombination. Upon inhibition of PARP base excision pathway (BER) is blocked followed by an accumulation of DNA lesions, conversion into DSBs that BRCA-deficient cells cannot resolve eventually resulting in cell death. Here, we addressed the question, whether targeting PARP might cause similar effects in AML cells.

## 7.1 PARP inhibition causes a heterogenous responses in AML cell lines

We initially analyzed endogenous protein expression levels of BRCA1, BRCA2 and PARP1 in AML cell lines harboring various genetic backgrounds as shown in (Figure 18A). Moreover, we explored endogenous RNA level using TMM (trimmed mean of M values)-normalized RNA-sequencing data (GSE126895) as shown in Figure 18B. Although, we found that BRCA1 and BRCA2 were expressed at RNA level and not mutated corresponding to the CCLE database (except for MOLM-13, heterozygous mutation, shown as dot feature in Figure 18A), expression of BRCA1 and BRCA2 was undetectable in some cell lines. We hypothesize that cell lines with low or no BRCA1/2 expression on protein and RNA levels (OCI-AML2, OCI-AML3, MV4-11 and MOLM-13) might be vulnerable to PARP inhibition. Hence, we treated AML cell lines with the PARP inhibitor Olaparib and measured cell viability after 72 hr of treatment and using the HTS-mediated DAPI exclusion assay as shown in Figure 18C. Surprisingly, all the AML cells with un-detectable BRCA expression tolerated PARP inhibition quite well, but on the other hand, cell lines OCI-AML-2 and THP-1 with relatively high expression of BRCA-1,

were the most sensitive to PARP inhibition, suggesting response to PARP inhibition in AML cell lines dose not corelate with amount of BRCA expression.

In this experiment, AML cells lines were treated with a dose range of 0.5 µM to 2.5 µM of Olaparib. We defined this concentration as the 'effective dose range' as most of the cell lines show marginal to intermediate response in order to potentially capture events that might elucidate the mechanistic background. At higher doses (e.g. 10 µM), most AML cell lines did not survive.

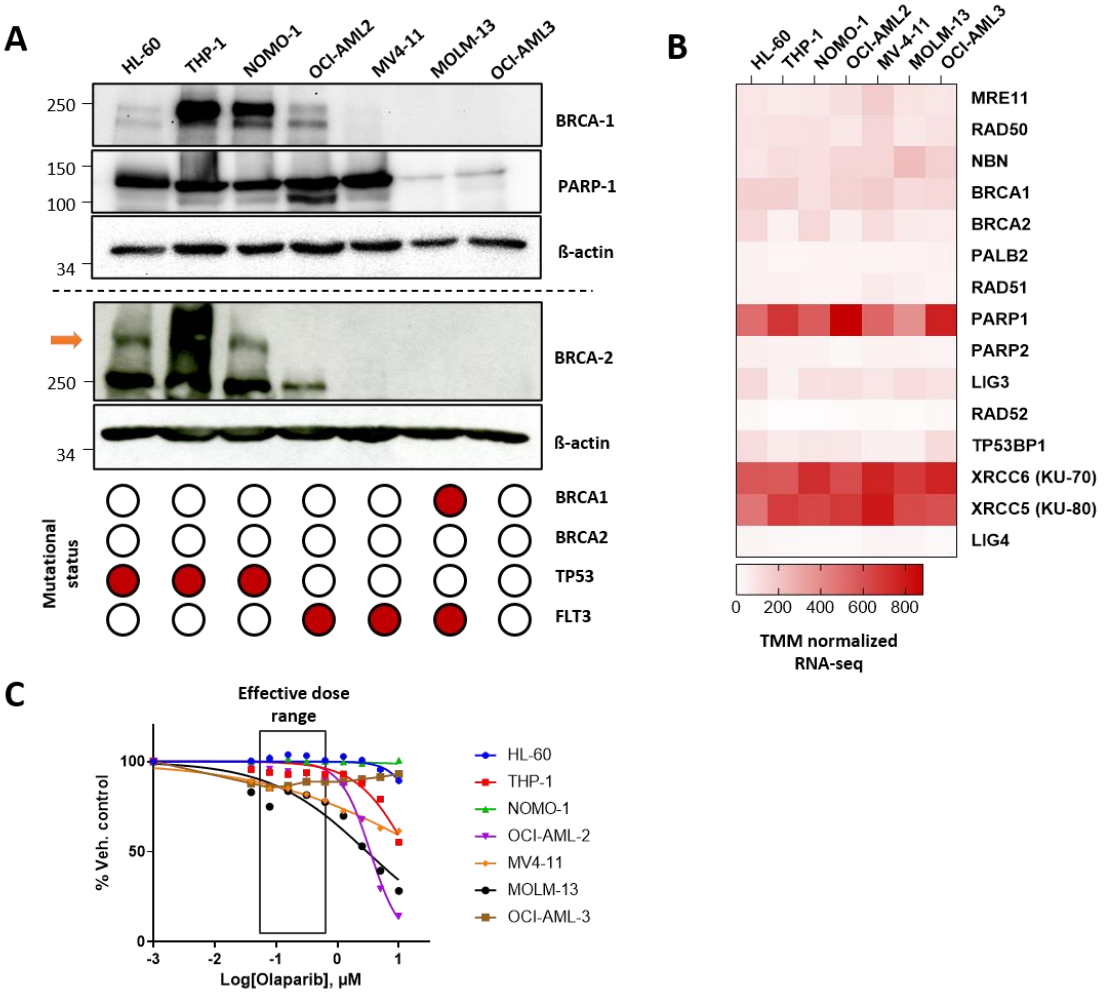


***Figure 18: Response to PARP inhibition in AML cell lines is independent of BRCA expression.***

*(A) Immunoblot analysis of endogenous expression of BRCA1, BRCA2 and PARP1 in 7 AML cell lines. The estimated molecular weight of BRCA2 is around 380 kDa and is indicated by an arrow. Actin was used as a loading control. Mutational status of indicted*

*genes obtained by CCLE and COSMIC databases are overlaid as features with red and white dots for each cell line; red indicates mutated and white indicates wild type status. (B) Heatmap for endogenous RNA transcript levels of key genes involved in DNA damage repair (DDR) as indicated. TMM (trimmed mean of M values) normalized transcript expression data was obtained from (GSE126895). (C) Dose-dependent effect of the PARP inhibitors Olaparib upon treatment for 72 hr in different AML cell lines as indicated.*

## 7.2 PARP inhibition induces DNA damage in AML cell lines

Most of the cells tolerated high dosages of Olaparib, hence we questioned, whether the non-responding cells accumulated PARP inhibition mediated DNA damage, or these cell lines are resistant to PARP inhibition altogether. We used gH2AX foci as a surrogate to measure DSBs.

In order to address this question, we performed neutral comet assay as shown in Figure 19 (quantification as shown in Figure 21A), and immunofluorescence based High Content Screening (HCS) for gH2AX measurement as shown in Figure 20 (quantification as shown in Figure 21B,) of AML cell lines upon Olaparib treatment with 1 µM and 2.5 µM for 72 hr. Accumulation of DNA damage was similar amongst different cell lines. All the cell lines showed an increase in comet tail lengths and gH2AX accumulation in a dose dependent manner upon Olaparib treatment. Moreover, these effects were independent on BRCA1 or BRCA2 expression.

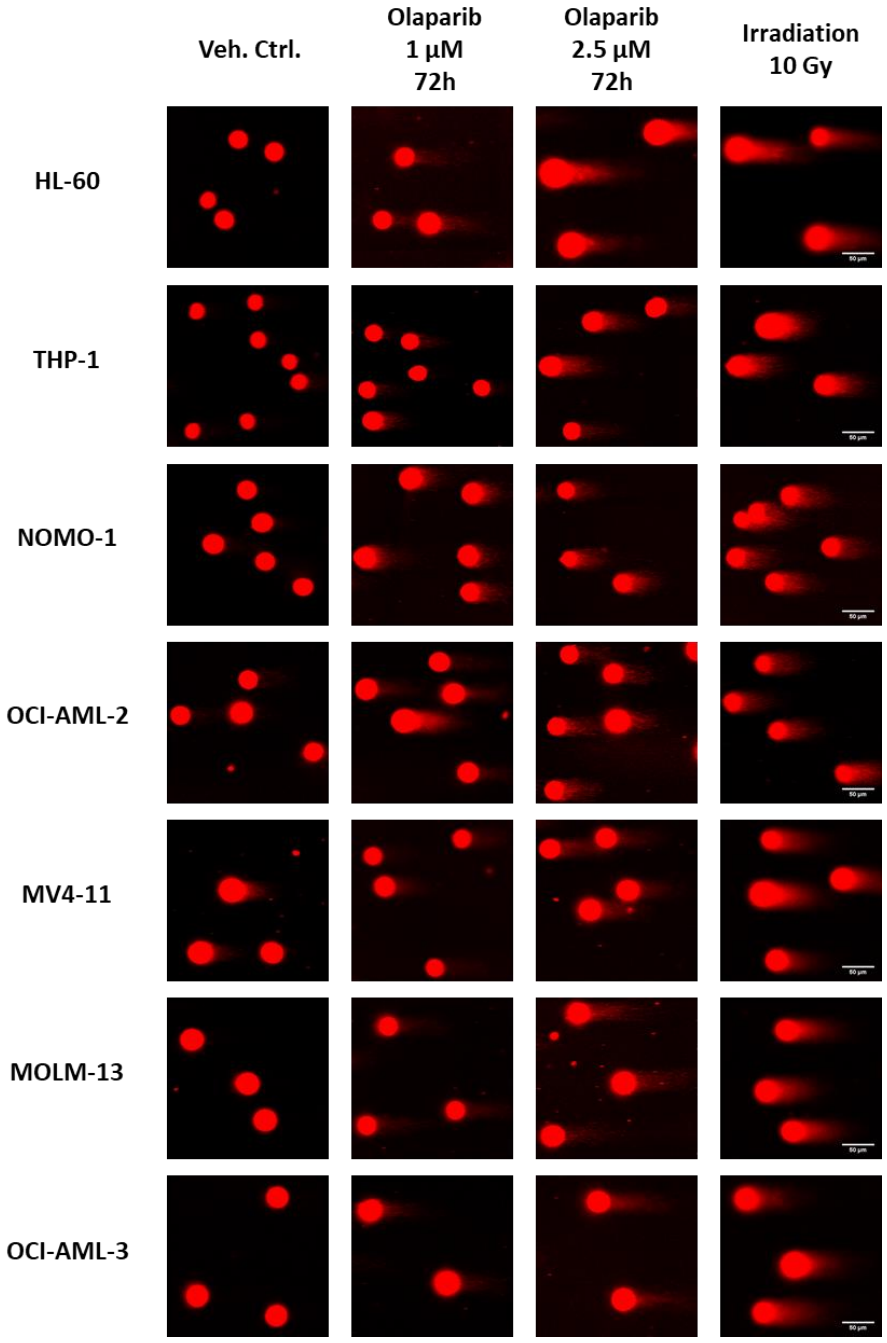


***Figure 19: Neutral comet assay screen in AML cell lines.***

*Neutral comet assay panel in AML cell lines showing dose dependent increase in comet tails upon Olaparib treatment for 72 hr with doses as indicated. Irradiation of 10 Gray (Gy) was used as a positive control for induction of DNA damage.*

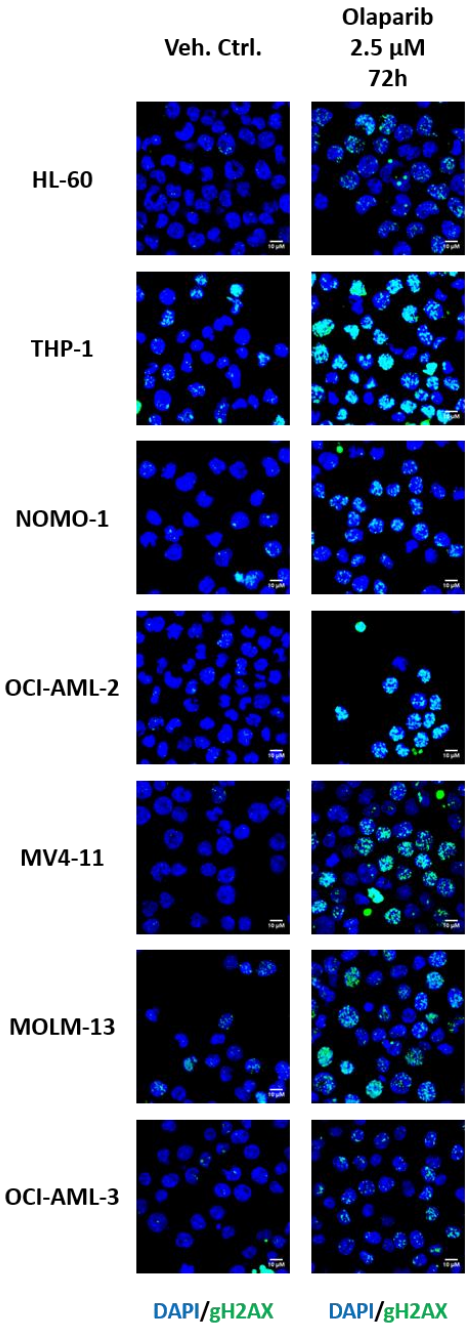


***Figure 20: Immunofluorescence based gH2AX screen in AML cell lines.***

*Immunofluorescence based gH2AX foci formation upon 2.5 µM Olaparib treatment for 72 hr and measured using OperaPhenix™ microscope. Scale bar 10 µm.*

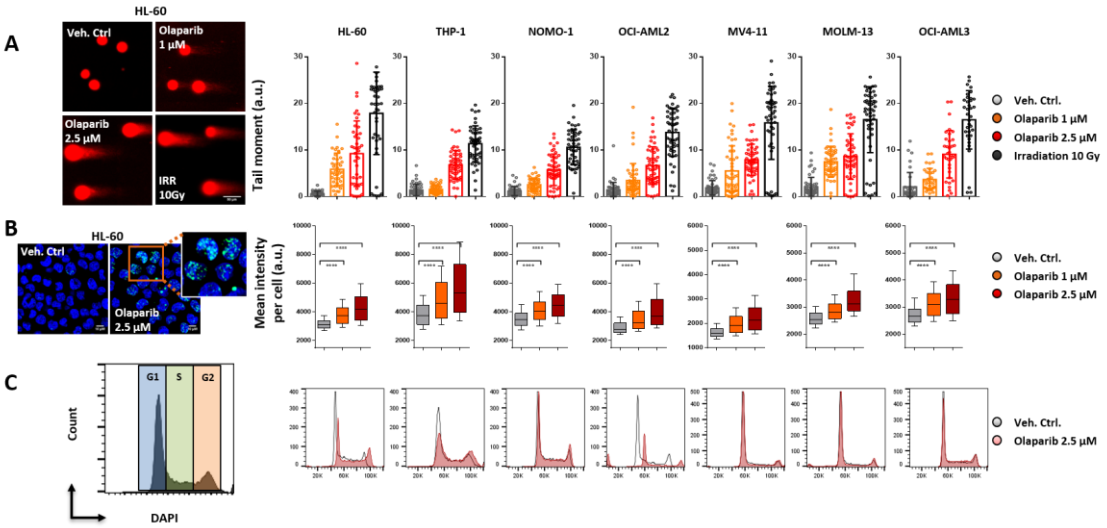


***Figure 21: PARP inhibition induces DNA damage in AML cell lines.***

*An exemplar image for (A) neutral comet assay, scale bar 50 µm (B) immunofluorescence based mean gH2AX (Ser 139) intensity per cell analysis, scale bar 10µm (C) flow cytometry plots showing cell cycle profiles, HL-60 cells were used. AML cell lines were treated with indicated concentrations of Olaparib for 72 hr. and gamma irradiation of 10 Gray (Gy) dose was used as positive control for induction of DNA damage. Scale bar, 10 µm. p-values: **** indicate <0.0001, as assessed by t-test using Welch's correction.*

Furthermore, we were interested to evaluate whether DNA damage accumulation would cause a S/G2 cell cycle arrest, in line with data presented in various other cancer models upon PARP inhibition, e.g. in ovarian cancer (Y. Fang et al., 2019), glioblastoma (Rasmussen et al., 2016). Therefore, we performed cycle profiling using DAPI-based flow cytometry (Figure 21C).

We observed a heterogeneous cell cycle profile in line with survival curves as shown earlier. Upon Olaparib treatment, a large fraction of OCI-AML-2 cells was dead, THP-1, HL-60 and NOMO-1 cells displayed an intermediate to subtle S/G2 arrest. In contrast, MV4-11, MOLM-13, and OCI-AML-3 cells had nearly identical cell cycle profiles upon Olaparib treatment compared to controls. As we observed continuously increasing DNA damage (Comet assay Figure 21A and gH2AX staining Figure 21B, respectively) in the latter cell lines upon Olaparib treatment, we further evaluated genetic background of these cells lines using CCLE database as shown in Table 7. Most of the cell lines harbor

heterozygous missense mutations in genes involved HR-based DNA damage repair, DNA damage response or cell cycle regulation. Interestingly, most of the responding cell lines were *TP53* wild-type and harbored *FLT3*-mutations.

| Cell lines | Mutated genes | Mutation | Type | Database |
|---|---|---|---|---|
| HL-60 | TP53 | c.(?_28)_(*1027_?)del | Deletion | CCLE, COSMIC |
| | DNMT3B | p.R537Q | | CCLE |
| | CDKN2A | p.R80 | Nonsense | CCLE |
| THP-1 | TP53 | p.R174 | Frame shift | CCLE |
| | ATM | p.T9354 | Missense | CCLE |
| | PALB2 | p.E873K | Missense | CCLE |
| NOMO-1 | TP53 | p.C242 | Frame shift | CCLE |
| | PALB2 | p.L961 | Silent | CCLE |
| OCI-AML-2 | FLT3-TKD | p.A680V | Missense | CCLE |
| | NCOR2 | p.Q510-P511 insQQ | Insertion | CCLE |
| MV4-11 | FLT3-ITD | — | | CCLE |
| | NBN | p.K690 | | CCLE |
| MOLM-13 | FLT3-ITD | — | | CCLE |
| | BRCA-2 | p.Q819R | Missense | CCLE |
| OCI-AML-3 | DNMT3A | R882H | | CCLE |
| | NPM1 | | Insertion, Frameshift | CCLE |

***Table 7: Mutation list in DDR genes***

In order to gain more insight into the genetic background and to identify specific gene expression signatures within the heterogeneously responding cell lines, we took advantage of an already established comprehensive list of genes implicated in various DNA damage repair pathways (Wood, Mitchell, & Lindahl, 2005) and performed unsupervised clustering of endogenous expression of these genes as shown in Figure 22.

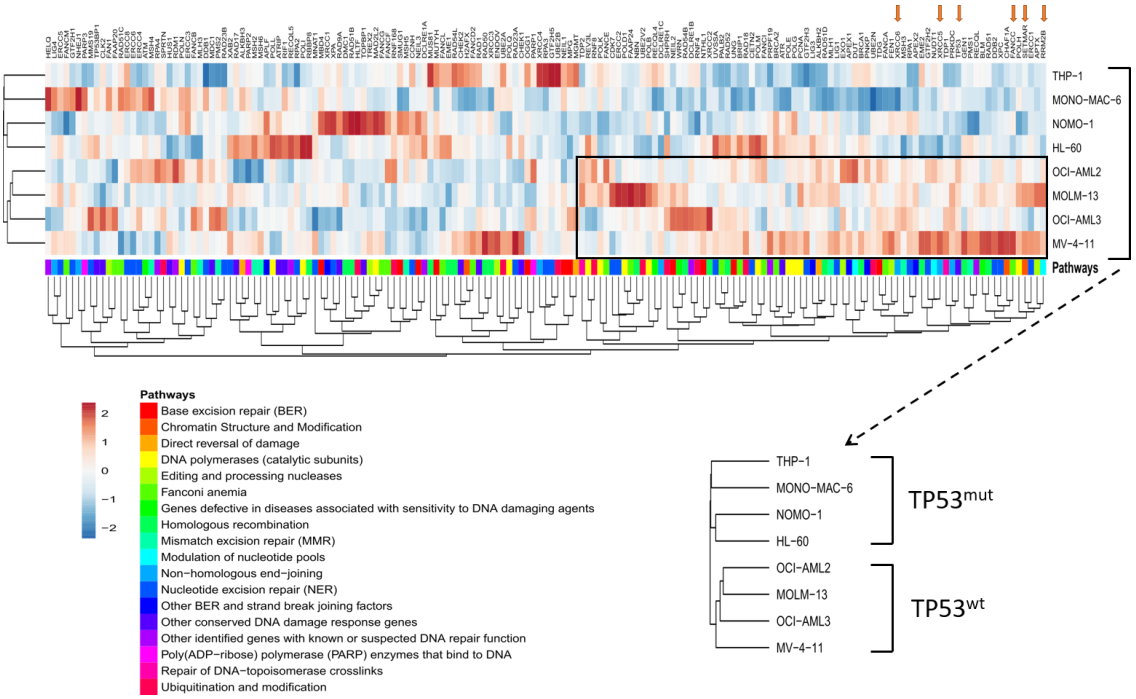


***Figure 22: Heterogenous expression of DNA damage repair genes in AML cell lines cluster based on TP53 mutational status.***

*Unsupervised hierarchical clustering was performed using a list of genes that have potential function in DNA damage repair. The list was obtained from (Wood et al., 2005). RNA expression dataset for indicated AML cell lines were obtained from (GSE126895) and normalized transcript values (Trimmed Mean of M-values, TMM values) were used to generate a heatmap. Each of the genes was annotated according to its role in DDR pathways as shown as a color palette in the figure legend. Co-clustering of genes of interest is indicated with an arrow and cell line clusters were enlarged to visualize two distinct groups with respect to TP53 mutational status within the heterogeneous expression patterns amongst the AML cell lines.*

We observed that AML cell lines segregated into two major clusters, *TP53*$^{wt}$ and *TP53*$^{mut}$. In line with recently published data demonstrating that *TP53*$^{mut}$ cells tend to depend on S/G2 phase of the cell cycle to repair DNA damage (Y. Fang et al., 2019; Moison et al., 2019); on the other hand, *TP53*$^{wt}$ cancers are highly regulated via TP53 activation. The identified gene expression signatures are consistent with our cell cycle profiles, as *TP53*-mutant cells undergo a slight S/G2 arrest upon Olaparib treatment, contrary to *TP53* wildtype cells. Interestingly, we observed a higher expression in XRCC6 (KU-70) and XRCC5 (KU-80) in MV4-11 and MOLM-13 cells, which are known proteins involved in NHEJ-mediated DSB repair.

## 7.3 PARP inhibition accumulates DSB in S and G2 phase in a time and dose dependent manner in MV4-11 cells

We observed accumulation of DSBs in a dose-dependent manner, however, the overall cell cycle profile remained unchanged in most *FLT3* wild-type cells. We therefore asked the question whether DSBs accumulate in all cell cycle phases equally or DNA damage was accumulated in any given cell cycle phase. For this purpose, we measured gH2AX expression in a cell cycle-dependent manner in AML cell lines using HCS technique to measure gH2AX in a single cell resolution and DAPI staining was used to quantify the amount of DNA content in a given cell cycle phase as shown in Figure 23.

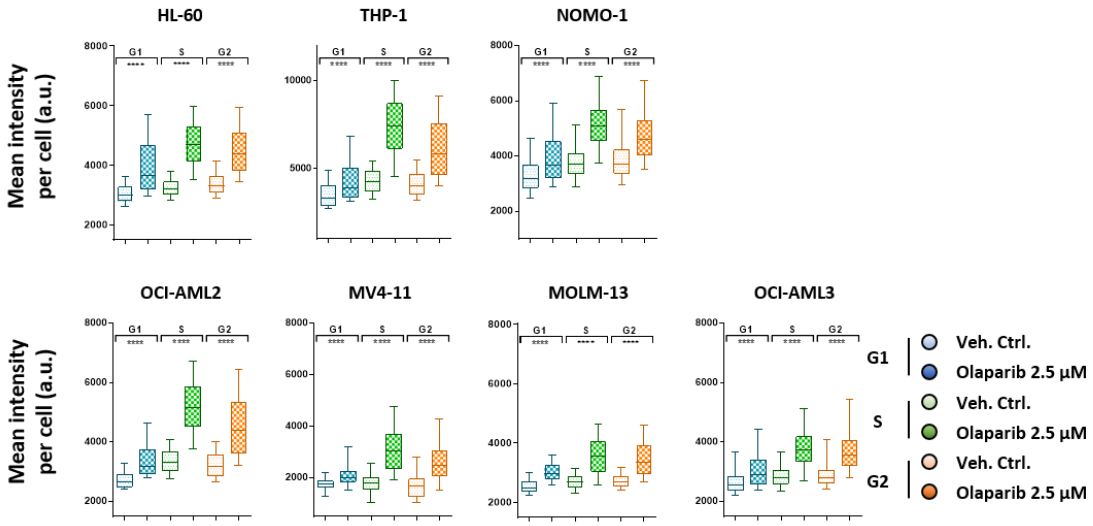


***Figure 23: PARP inhibition accumulates DNA damage in S/G2 phase in AML cell lines***

*Mean intensity for gH2AX was quantified in AML cell lines upon 2.5 µM concentration of Olaparib for 72 hr. p-values: **** indicate <0.0001, as assessed by t-test using Welch's correction.*

We observed that DSBs were accumulated throughout all cell cycle phases upon Olaparib treatment, but they were significantly enriched in the S and G2 phase. All the cell lines displayed a similar pattern in accumulation of DSBs in S phase upon Olaparib treatment. Although, all the cell lines have high levels of DSBs in G2 phase, they were slightly reduced in comparison to S-phase and interestingly, totally lowered DSBs in G1 phase.

We next questioned whether gH2AX accumulation increased in a time and dose dependent manner. For this reason, we next performed time kinetics upon Olaparib treatment in MV4-11 cells. We observed a significant increase in gH2AX levels at 72h compared to 4 h and 24 h (Figure 24A). Interestingly, gH2AX levels were highest in S phase, but declined in G2 and approached steady state levels in G1. We observed a similar pattern when we treated MV4-11 cells with different doses of Olaparib Figure 24B. The amount of gH2AX foci was dose dependent in all phases of the cell cycle, but highest levels of DNA damage were again observed in S phase. This indicates that Olaparib-induced DNA damage is repaired in a cell cycle dependent manner.

Based on time and dose kinetics, we next addressed a potential pathway of choice to mitigate accumulated damage in S and G2 phase of MV4-11 cells. In addition, considering un-detected protein levels of *BRCA-1* and *BRCA-2* as shown earlier, suggested that MV4-11 cells might have a dysfunctional HR-dependent DNA damage repair with most of alterations repaired in G1. To address this hypothesis, we performed cell cycle dependent analysis of 53BP1 foci and phosphorylated RPA (pRPA) foci formation upon Olaparib treatment for 72 h as shown in Figure 24C. We observed that pRPA foci were detected in all phases of the cell cycle at equal levels suggesting replicative stress upon Olaparib treatment. Interestingly, 53BP1 foci were higher in all the cell cycle phase. Enrichment of 53BP1 foci during S and G2 phase may indicate its reliance on NHEJ pathway to mitigate DNA damage.

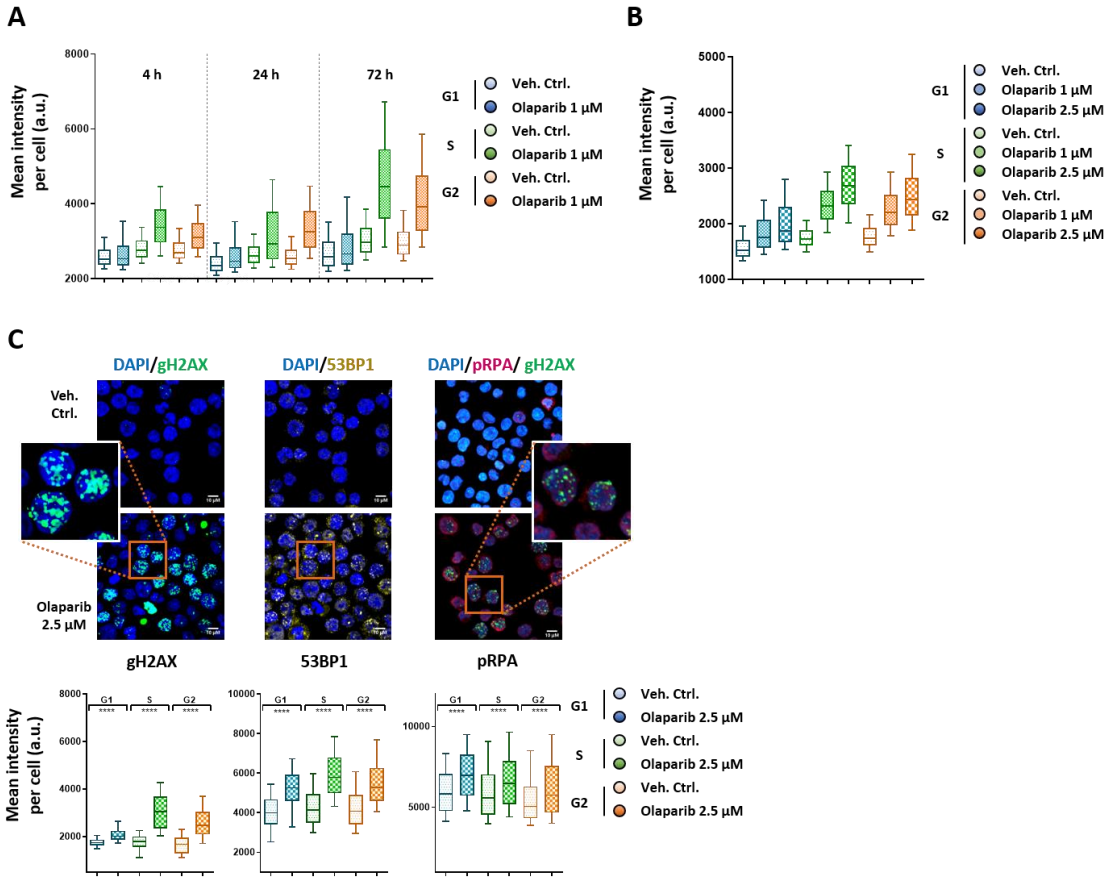


***Figure 24: PARP inhibitor- mediated DNA damage accumulation in a time and dose dependent manner in MV4-11 cells.***

*(A) Mean intensity for gH2AX was quantified in MV4-11 cells upon 1 µM concentration of Olaparib at various time points as indicated. (B) Mean intensity for gH2AX was quantified upon Olaparib treatment as indicated and measured after 72 hr. (C) Representative images and cell cycle dependent analysis of gH2AX (Ser 139), 53BP1 and pRPA (S4/S8) foci upon Olaparib treatment for 72 hr in MV4-11 cells. Scale bar, 10 µm. p-values: **** indicate <0.0001, as assessed by t-test using Welch's correction.*

## 7.4 PARP inhibition activates p53 in MV4-11 cells

As MV4-11 cells accumulated DSBs primarily in S/G2 phase of the cell cycle in a time and dose dependent manner upon Olaparib treatment, we explored whether this finding has any biological effect. We therefore treated MV4-11 cells in a time and dose

dependent manner with Olaparib and analyzed proliferation (Figure 25A), Annexin V- (Figure 25B) and CD11b expression (Figure 25C). In line with survival curve and cell cycle profile data shown earlier (Figure 18 and Figure 21), we observed no significant differences compared to vehicle-treated controls at low Olaparib concentrations (0.125 – 1 µM). We also treated MV4-11 cells with an extreme dose 10 µM, cell underwent a S/G2 arrest at 24 h, but most of the cells recovered over time with some cell dying, as demonstrated by an increased sub-G1 fraction at 72 hr. as shown in Figure 25D. This effect was likely due to p53 activation and p21 induction allowing cells to resolve DNA damage over time (Figure 25E) (Pan et al., 2017). Of note, p53 activation and p21 expression was also observed at lower concentrations.

We wondered if the remaining BRCA-1 in cells with low expression might still be enough for repairing Olaparib mediated DSBs. For this reason, we performed stable knockdown of BRCA-1 using a doxycycline (DOX) inducible system and still be did not observe any significant difference in proliferation (Figure 25F) measured after 72 h pre-induction with DOX knockdown efficiency shown in Figure 25G, suggesting MV4-11 cells might be BRCA-1 independent.

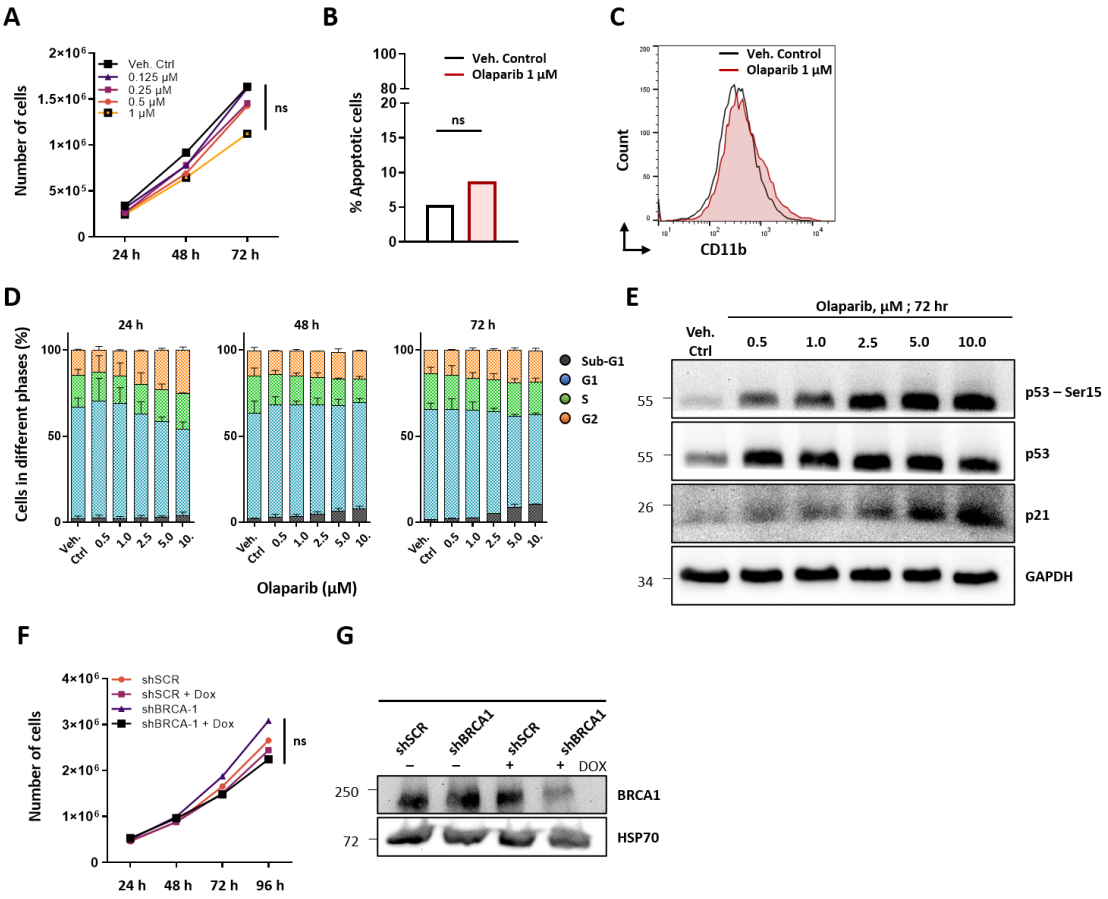


***Figure 25: PARP inhibition activates p53 in dose dependent manner in MV4-11 cells.***

*(A) Dose and time-dependent analysis of viable cells upon Olaparib treatment with concentrations as indicated. MV4-11 cells were treated with 1 µM Olaparib and the number of apoptotic cells were measured using Annexin-V expression (B) and the differentiation was measured CD11b staining. (D) MV4-11 cells were treated with Olaparib as indicated and cell cycle analysis was performed over time using DAPI-based flow cytometry analysis. (E) Immunoblot analysis of MV4-11 cells upon Olaparib treatment for 72 hr as indicated using antibodies directed against XXXX. For loading control the blot was stripped and stained with anit-GAPDH antibody. (F) Stable BRCA-1 knockdown (shBRCA-1) was obtained in MV4-11 cells using 1µg/mL doxycycline (DOX) for 72 hr. and the number of viable cells was compared to scramble control (shSCR). (G) Immunoblot analysis validating doxycycline induced BRCA-1 knockdown efficiency measured after 72 hr in MV4-11 cells. p-value, not significant (ns) assessed using Student t-test.*

## 7.5 AML cells evade apoptosis due to inherent high expression of anti-apoptotic proteins

p53 acts as a master regulator of apoptotic cell death and is inactivated in almost 50% for solid tumor. Interestingly, *TP53* is mutated or depleted in only a small fraction of AML patients (Prokocimer, Molchadsky, & Rotter, 2017). p53 activation promotes apoptotic cell death induced by activating BAK and BAX-mediated intrinsic apoptosis upon genotoxic insults and DNA damage (R. Singh et al., 2019). This intrinsic apoptosis is blocked by BCL2 family members, which are often highly expressed in AML patients and cell lines (Pan et al., 2014).

Hence, we first tested the endogenous expression patterns of anti-apoptotic proteins on the protein (Figure 26A) and transcript levels (Figure 26B). We found that THP-1 and OCI-AML-3 cells have a significant higher expression of MCL-1 at RNA level relative to BCL2 or BCL-xL, whereas no significant differences in expression were detected in other cell lines or other proteins. We next performed unsupervised hierarchical clustering for genes directly and associatively involved in regulating apoptosis (MD Anderson apoptosis gene list REF) as shown in Figure 26C. We could detect two major clusters: THP-1 and OCI-AML-3 cell lines formed one cluster, likely due to its high expression of MCL1; MV4-11, MOLM-13 and OCI-AML-2 cell lines represented the other cluster. This is consistent with clusters based on DNA damage gene expression shown in Figure 22 where AML cell lines with a *TP53*$^{wt}$ background showed a similar endogenous expression patterns in genes involved in DNA damage and apoptosis.

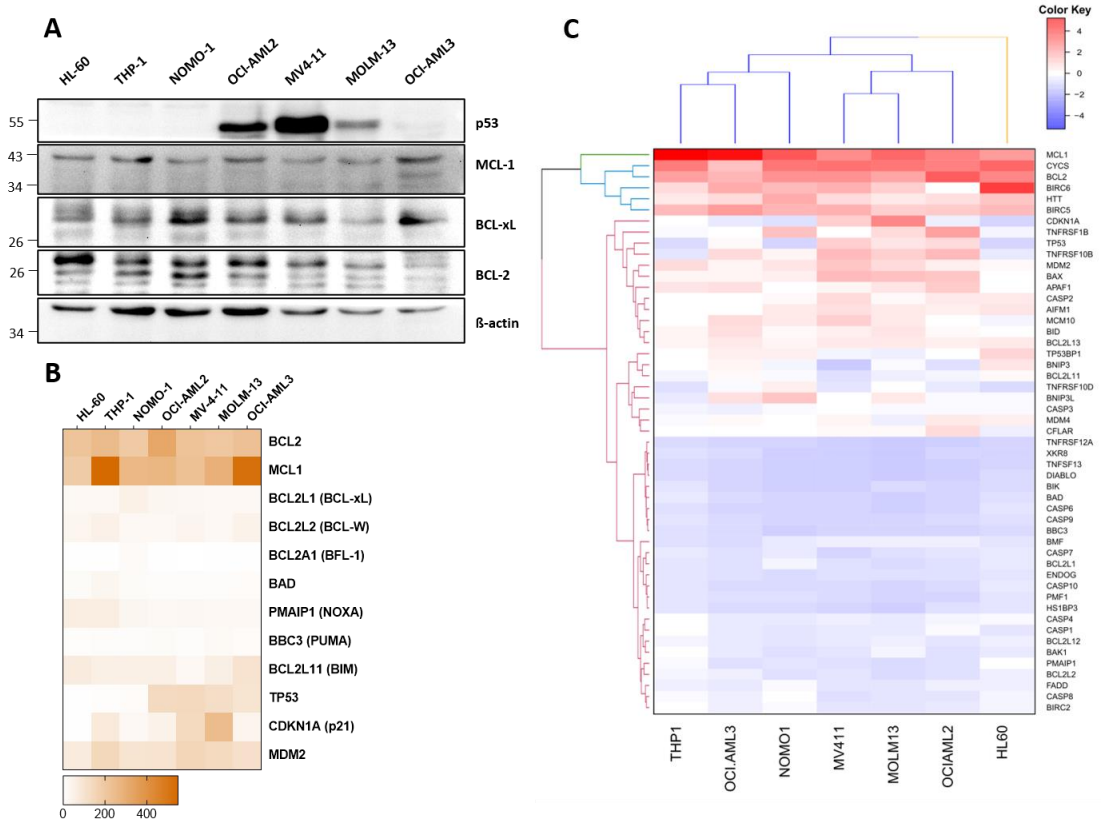


***Figure 26: AML cell lines have an inherent anti-apoptotic dependency.***

*(A) Heatmap for endogenous RNA transcript levels of key genes involved in apoptosis pathway as indicated. Transcript expression data was obtained from (GSE126895) and normalized transcript levels (trimmed mean of M values; TMM) were used to plot the heatmap. (B) Immunoblot analysis of endogenous expression of anti-apoptotic proteins in 7 AML cell lines as indicated. (C) Unsupervised hierarchical clusters using list of genes with potential functions in regulating apoptotic pathways. Apoptotic gene list was obtained from MD Anderson pathways database.*

OCI-AML-3 cells, which did not cluster with other *TP53*$^{wt}$ cell lines, were the exception in this analysis. This effect was likely due to higher expression of MCL1 and inherent resistance to BCL2 inhibition (Bogenberger et al., 2017; Pan et al., 2017), which makes OCI-AML3 cells similar to THP-1 cells. To test function dependencies, we treated all cell lines with specific inhibitors targeting MCL1, BCL2 or BCL-xL as shown Figure 27.

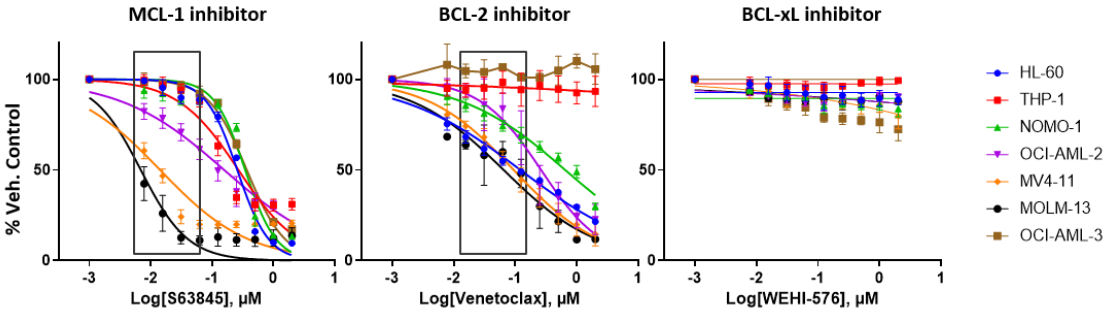


***Figure 27: BH3 inhibitor response in AML cell lines***

*Dose response curves of anti-apoptotic inhibitors S63845 (MCL-1 inhibitor), Venetoclax (BCL-2 inhibitor) and WEHI-576 (BCL-xL inhibitor) upon treatment for 72 hr in seven AML cell lines as indicated.*

Consistent with literature (Bogenberger et al., 2017; Pan et al., 2017), THP-1 and OCI-AML-3 cells were highly resistant to the BCL-2 inhibitor Venetoclax, but responded to S63845, a specific MCL1 inhibitor. Targeting BCL2 substantially inhibited cell growth of MV4-11, MOLM-13, OCI-AML2, but also of HL-60 and NOMO1 cells. On the other hand, none of the cell lines responded to the BCL-xL inhibitor WEHI-576 suggesting these cells might have a preferential dependency upon BCL2 and/or MCL1 proteins in evading apoptosis.

## 7.6 PARP and BCL-2 inhibition synergistically induces apoptosis in *TP53$^{wt}$ FLT3$^{mut}$* AML cell lines and primary AML patient samples

As we observed DNA damage upon Olaparib treatment, but no significant changes in survival, we speculated that increased levels of anti-apoptotic proteins compensate p53-mediated apoptosis and combined treatment of Olaparib and BCL-2 inhibitors will result in synergistic effects. To address this question, we treated MV4-11 cells with

Olaparib and Venetoclax in time and dose dependent manner and measured survival for single treatment and combinations as shown in Figure 28A.

Treatment with either agent alone caused a time and dose dependent decline in cell growth. Combined treatment further enhanced the effect and was highly synergistic as demonstrated by ZIP synergy score calculations (Figure 28B). We also tested the synergy upon combination using Annexin-V and 7AAD staining to measure cells in both early and late stage of apoptosis (indicated as "Apoptotic cells') using flow cytometry and found that the combination induced synergistic apoptosis as shown in Figure 28C.

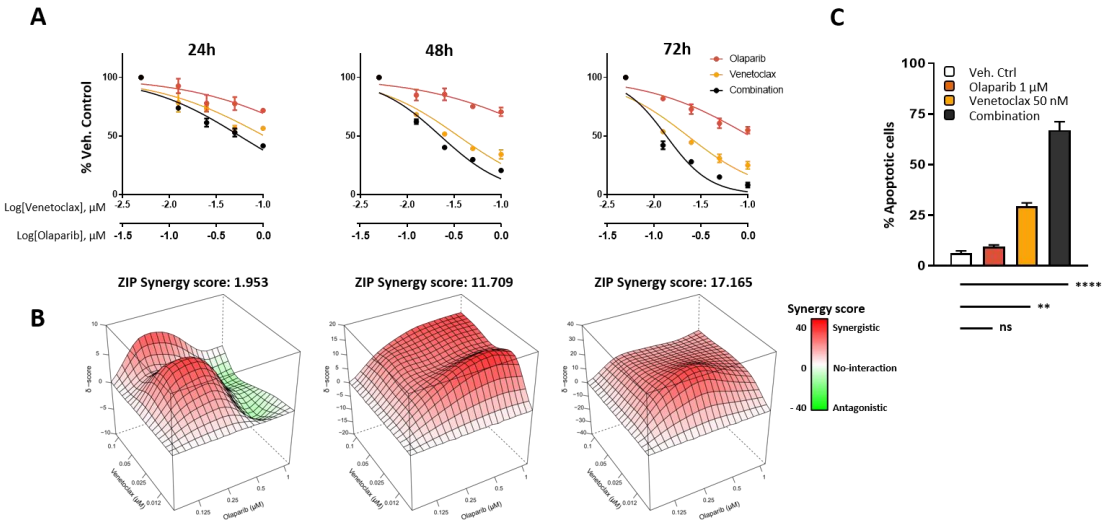


***Figure 28: PARP inhibition and BCL2 inhibition synergistically induces apoptosis in MV4-11 cells.***

*(A) Dose response plots of MV4-11 cells treated with a combination of Olaparib and Venetoclax and measured over time as indicated. (B) Synergy plots for the combination of Olaparib and Venetoclax measured over time in MV4-11 cells as indicated. Combination index was calculated using ZIP model-based synergy quantification. (C) Percent apoptotic cells were measured in MV4-11 cells upon combination treatment for 72 h with doses as indicated. p-values: **** indicate <0.0001, ** indicate <0.001, ns indicate not significant, as assessed by one-way ANOVA.*

We also tested if this combination is effective in other *TP53*$^{wt}$ cell lines like MOLM-13, OCI-AML-2 and OCI-AML-3 cells lines. As expected, MOLM-13 and OCI-AML-2 cells accumulated DSBs in S and G2 phase at 2.5 µM of (Figure 29A) and 1 µM (data not

shown) Olaparib treatment. At both concentrations, a subtle increase in p53 expression and activation as well as p21 expression (Figure 29B) was observed. The combination of Olaparib and Venetoclax induced synergistic inhibition of cell growth (Figure 29C) and apoptotic cell death (Figure 29D) in both cell lines.

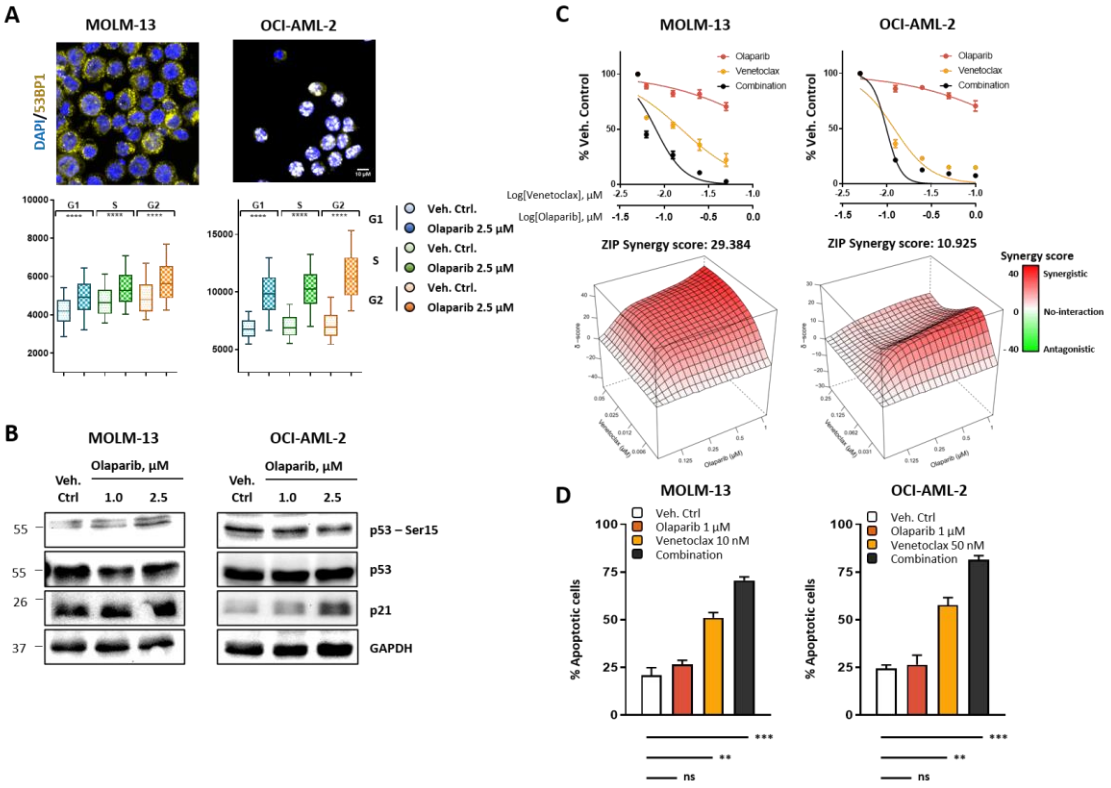


***Figure 29: Combined PARP and BCL2 inhibition synergistically induces apoptosis in TP53$^{wt}$ and FLT3$^{mut}$ AML cell lines.***

*(A) Representative images and cell cycle dependent accumulation of 53BP1 foci upon Olaparib treatment for 72 h in MOLM-13 and OCI-AML-2 cells. p-values: **** indicate <0.0001, assessed by t-test using Welch's correction (B) Immunoblot analysis for indicated proteins upon Olaparib treatment for 72 hr. in MOLM-13 and OCI-AML-3 cell lines. (C) Dose response plots and synergy plots for MOLM-13 and OCI-AML-2 cells upon combination treatment of Olaparib and Venetoclax for 72 hr as indicated. Combination index was calculated using ZIP model-based synergy quantification. (D) Percent apoptotic cells were measured in MOLM-13 and OCI-AML-2 cells upon combination treatment for 72 hr as indicated. p-values: **** indicate <0.0001, ** indicate <0.001, ns indicate not significant, assessed by one-way ANOVA.*

On the contrary *TP53*$^{wt}$ cell lines, OCI-AML-3 cells also accumulated DSBs in S and G2 phases upon Olaparib treatment but showed reduction in 53BP1 foci across cell cycle phases (Figure 30A). Although, Olaparib treatment activated p53, at concentrations of 2.5 µM and above (Figure 30B) combination of Olaparib with Venetoclax did not induce synergistic responses (Figure 30C-D). We evaluated OCI-AML-3 cells with MCL1 inhibitor, S63845 in combination with Olaparib but the combined treatment showed moderate to no significant synergy between S63845 alone and in combination with Olaparib.

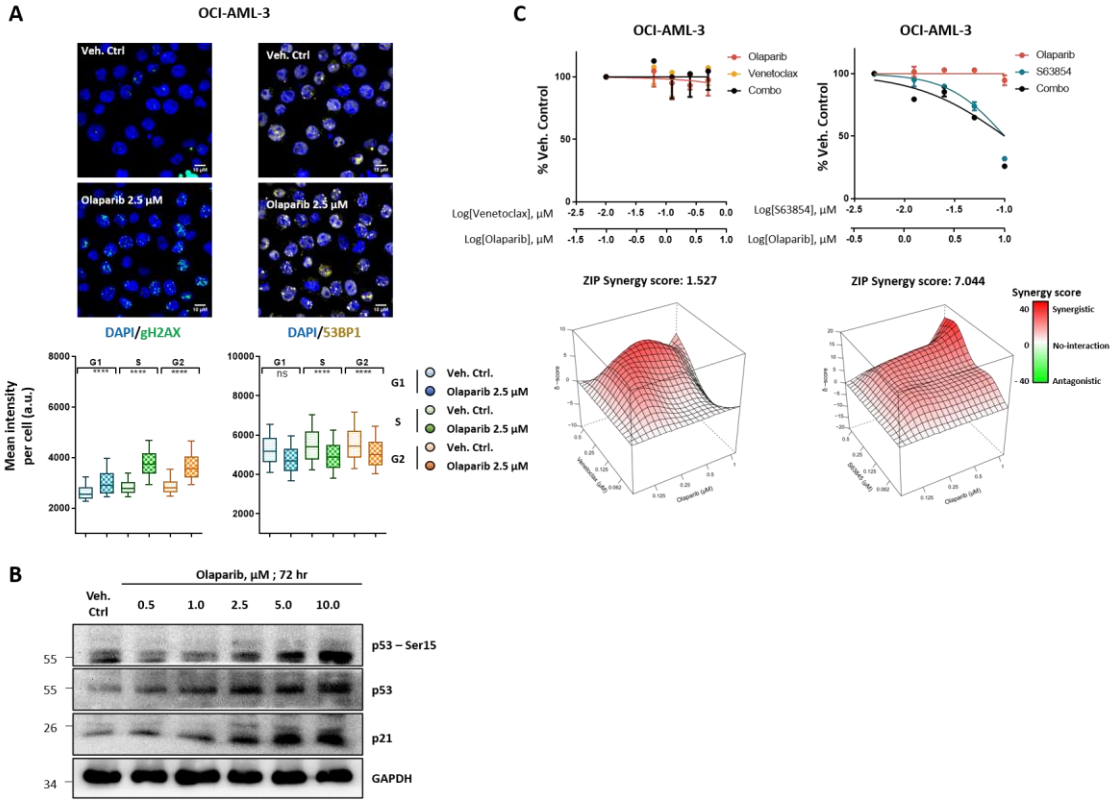


***Figure 30: OCI-AML-3 cells resistant to physiological Olaparib dose levels but are inherently dependent on MCL-1.***

*(A) Representative immunofluorescence of staining and cell cycle-dependent accumulation of gH2AX (Ser 139) and 53BP1 foci upon Olaparib treatment for 72 hr in OCI-AML-3 cells. p-values: **** indicate <0.0001; ns indicate not significant, assessed by t-test using Welch's correction. (B) Immunoblot analysis for indicated proteins upon Olaparib treatment for 72 h in OCI-AML-3 cells. (C) Dose response plots and (D) synergy plots for OCI-AML-3 cells upon combination treatment of Olaparib and Venetoclax in*

*comparison with Olaparib and S63845 for 72 hr as indicated. Combination index was calculated using ZIP model-based synergy quantification.*

We further evaluated the efficiency of Olaparib in combination with Venetoclax compared to FLT3 inhibitor (FLT3i) treatment in *FLT3$^{ITD}$* mutated cell lines MV4-11 and MOLM-13. Here, we tested two FLT3i, Midostaurin and Crenolanib in combination with Olaparib and compared survival against the combination of Olaparib and Venetoclax (Figure 31A-B). Although, both of these inhibitors are effective against *FLT3$^{ITD}$*-positive cells, both cell lines were already highly sensitive to Crenolanib alone and showed only marginal to no synergy in combination with Olaparib. The combination with Midostaurin showed synergistic effects in both the cell lines, however, the combination of Olaparib and Venetoclax demonstrated to be even more effective.

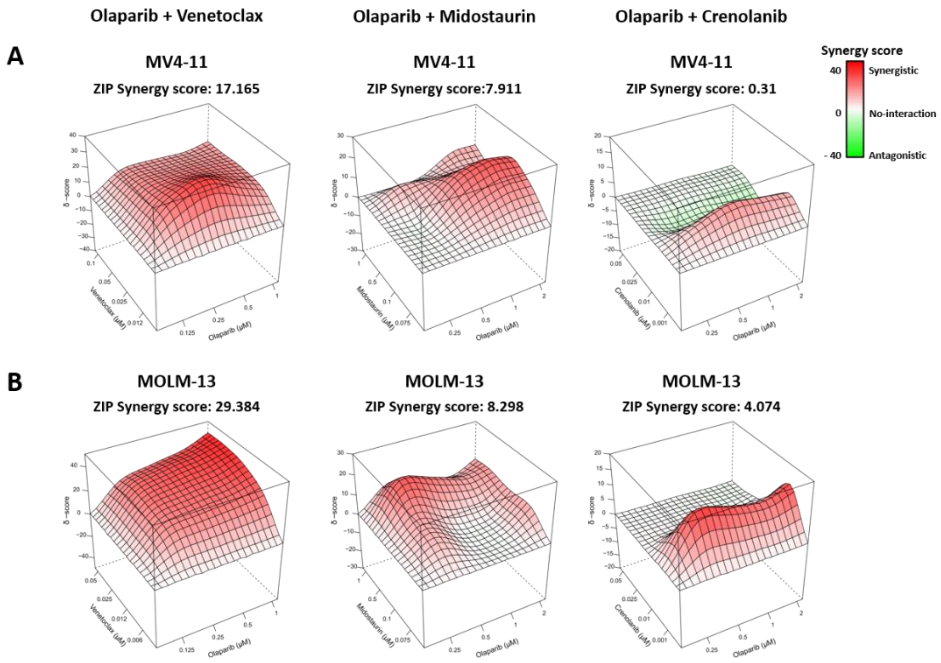


***Figure 31: Combined inhibition of PARP and BCL2 or FLT3 in FLT3$^{ITD}$-mutant cell lines.***

*Synergy plots for (A) MV4-11 and (B) MOLM-13 cells upon combination treatment with Olaparib and Venetoclax, Olaparib and Midostaurin, and Olaparib plus Crenolanib for 72 hr as indicated. Combination index was calculated using ZIP model-based synergy quantification.*

We also tested primary AML patient samples for BRCA1 expression in *FLT3*$^{wt}$ and *FLT3*$^{ITD}$ mutation backgrounds. AML patient sample number 7 (AML #7) resembled endogenous expression patters like MOLM-13 and MV4-11 cells with un-detectable BRCA1 protein expression as shown in Figure 32A. As reported that many AML samples were hypermethylated at *BRCA1* locus (Scardocci et al., 2006) and about 10-15% of AML samples have a "BRCA-low" phenotype (Dellomo et al., 2019), we evaluated the effectiveness of Olaparib and Venetoclax combination in primary AML sample (AML #7) using colony forming potential as shown in Figure 32B. We observed a modest reduction colony numbers upon in combination treatment compared to untreated controls.

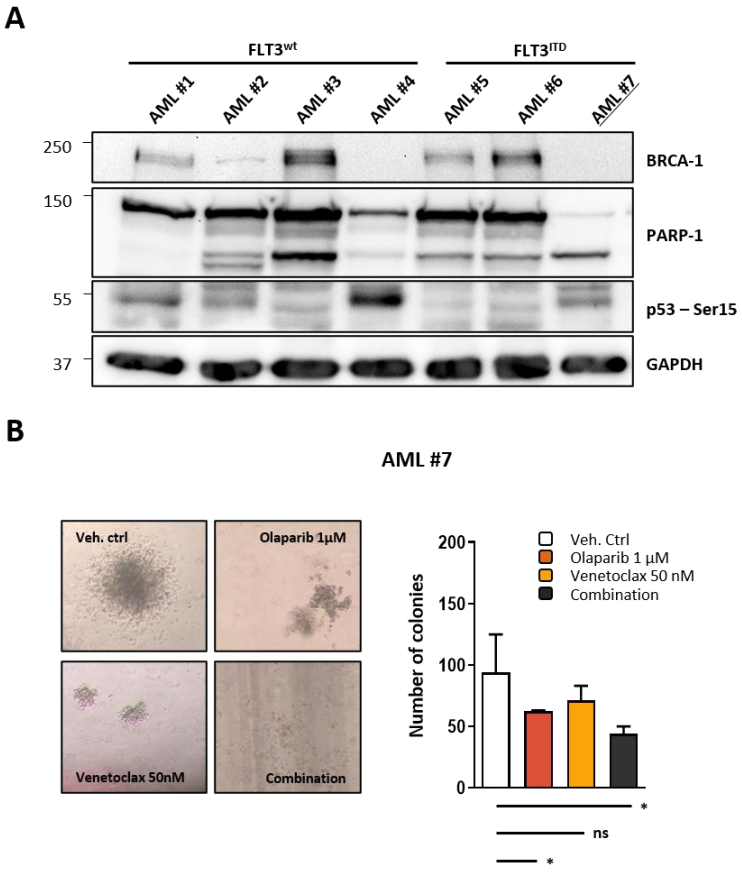


***Figure 32: Combined inhibition of PARP and BCL2 is effective in FLT3$^{ITD}$ primary patient sample***

*(A) Immunoblot analysis of endogenous expression levels of indicated proteins in primary patient samples. (B) Representative image and number of colonies upon combined inhibition of PARP and BCL2 in AML sample number 7 (AML #7). Colony forming potential was evaluated atl day 14 after start of treatment. p-values: * indicate <0.01; ns indicate not significant, assessed by one-way ANOVA.*

Taken together, our data demonstrate that AML cell lines accumulates DNA damage upon PARP inhibition irrespective of *BRCA1* or *BRCA2* status and combining PARP inhibition in *TP53$^{wt}$* and *FLT3$^{ITD}$* AML cell lines and primary samples along with anti-apoptotic BCL2 inhibitor showed promising response.

# 8. Discussion

AML is a heterogeneous disease and characterized by chromosomal abnormalities and/or recurrent mutations. Despite recent advances in molecular techniques, including sequencing of large patient cohorts, which has provided a better understanding of pathophysiology and resistance mechanisms, current treatment options are still limited with an overall survival of only 5-10 months in elder patients (Papaemmanuil et al., 2016). Heterogeneity in AML is increasingly well-defined with consistent updates in risk stratification and prognostic markers based on genetic alterations. Moreover, an increasing number of clinical trials is trying to target specific genetic alterations in defined AML sub-type specific. For instance, a number of inhibitors specifically target *IDH1/2* or *FLT3* mutations. Two FLT3 inhibitors, Midostaurin and Gliteritinib have already been approved by the FDA (Daver et al., 2019; Dellomo et al., 2019) as first line and maintenance therapy or as a salvage therapy for relapsed/refractory diseases, respectively. However, high relapse rates and limited success upon monotherapy approaches has urged the development of combination strategies to achieve improved outcomes and minimal side effects.

The goal of this study was to initially characterize the response of the PARP inhibitor Olaparib in various AML cell line models with heterogeneous mutational background and elucidate an effective response that could sensitize cells to targeted combination therapies. We also evaluated the inherent dependency on anti-apoptotic proteins such as BCL2 and MCl1 and postulate a combination strategy by utilizing PARP inhibitor mediated DNA damage and taking advantage of anti-apoptotic dependencies in AML cell lines and primary AML samples.

## 8.1 Relevance of PARP inhibition in AML

Exposure to genotoxic stress or DNA damaging agents cause DSBs. PARP1 plays an important role in mitigating the DNA lesions and in the restart of replication. PARP1 carries out this function by initial PARylating the DNA and acts as a sensor to recruit proteins involved in DDR pathways specific to the type of DNA damage. Once the DNA

damage/lesions are corrected, PARP1 orchestrates the removal of itself and other proteins from the site of damage by a process called PARylation (Luo & Kraus, 2012). PARP inhibition on the other hand leads to trapping of PARP1 at the site of damage, unable to auto-PARylate itself and therefore preventing its removal. These lesions require HR-mediated and error-free repair. Cancer cells, which lack essential genes capable of performing HR-mediated repair become selectively vulnerable to PARP inhibition. Breast and ovarian cancers are such cancer types in which "synthetic lethality" was first studies and led to the approval of PARP inhibitors such as Olaparib, Rucaparib and Talazoparib in germline *BRCA*-deficient cancers by the FDA (S. E. Caulfield et al., 2019).

PARP inhibitors have also been studied in AML cells with chromosomal translocations including AML1-ETO, KMT2A-AF9 and PML-RARα. Rearrangements like AML1-ETO and PML-RARα have been linked to dysfunctional HR activity by reduced expression of HR genes such as RAD-51, ATM, BRCA-1, and BRCA-2 and by an inability to recruit RAD51 to the site of DSBs (Esposito et al., 2015). On the contrary, KMT2A-AF9 (also known as MLL-AF9) leukemias have a more efficient HR, leading to PARP resistance (Esposito et al., 2015). Furthermore, epigenetic profiling has revealed "BRCA-low" phenotype due to deficiencies in BRCA-1 and BRCA-2 in 15-20% of AML patients making these cells ideal candidates for PARP inhibition. Additionally, recent work (Maifrede et al., 2018) has demonstrated PARP inhibition in combination with FLT3 inhibitors to act synergistically in FLT3-ITD mutated AML cell lines and in xenograft murine models suggesting PARP inhibition is a valid option in AML.

Hence in this study, we evaluated several AML cell lines with well-characterized genetic backgrounds as a model to evaluate and characterize PARP inhibitor sensitivity. We chose cell lines with MLL-AF9 translocations like THP-1 and MOLM13, the MLL-AF4 positive cell line MV4-11 and MLL wild-type cell lines like OCI-AML-2 and OCI-AML-3. We also considered other mutational backgrounds like FLT3-ITD mutations, which can be found in 25-30% of AML cases; MOLM-13 and MV4-11 are classical AML cell lines in order to study the FLT3-ITD phenotype. As another mutation we considered the *TP53* status, a common mutation in AML with about 8% in *de novo* AML cases and significant

accumulation in the adverse risk-group with extremely limited treatment options. Cell lines harboring TP53 mutations in our analysis were HL-60, THP-1, and NOMO-1 while TP53 wild-type cell lines were OCI-AML-2, MV4-11, MOLM-13, and OCI-AML-3.

### 8.1.1 "BRCA-low" phenotype in AML

In order to evaluate "BRCA-Low" phenotype in AML cell lines, we performed a immunoblot based endogenous protein expression of BRCA-1 and BRCA-2, and observed that MOLM-13, OCI-AML-3, and MV4-11 cells showed un-detectable BRCA-1 and BRCA-2 expression. OCI-AML-2 showed a moderate expression of BRCA-1, but un-detectable BRCA-2 expression. On the other hand, HL-60, THP-1, and NOMO-1 cell lines expression of both BRCA-1 and BRCA-1 proteins was detected. Of note, endogenous RNA expression levels were relatively low for all the cell lines.

We argued that these "BRCA-low" (low or un-detectable expression of both BRCA-1 and BRCA-2) might sensitize the cells to PARP inhibition. In our initial dose response screen with Olaparib, we observed heterogenous responses, OCI-AML-2 cells was the most sensitive cell line upon Olaparib treatment with an IC50 value of 1.42 µM followed by MOLM-13 with an IC50 value of 3.02 µM. HL-60 (IC50 value 28.56 µM), NOMO-1, and OCI-AML-3 cell lines represented the most resistant ones, with extrapolated IC50 values of more than 50 µM. THP-1 and MV4-11 showed moderate response to Olaparib treatment with IC50 values of 14.14 µM and 32.38 µM respectively. Most of the cell lines with low BRCA expression tolerated moderate doses of the PARP inhibitor Olaparib. Moreover, also other genetic marker did not predict sensitivity to PARP inhibition, which might be the result of the small sample size (N=7).

We further questioned, if lower expression level of BRCA-1 would result in inhibition of cell proliferation and survival, hence we performed stable inducible knockdown of BRCA-1 in MV4-11 cells (also for MOLM-13 and OCI-AML3 cells; data not shown) and evaluated differences in proliferation upon knockdown. To our surprise, there was no significant change in proliferation upon BRCA-1 knockdown, suggesting BRCA-1 independent response to PARP inhibition in these cell lines. On the other hand, OCI-

AML-2 cells with low BRCA-1 and no detectable expression of BRCA-2 was the most sensitive to Olaparib treatment, and THP-1 cells with high expression of both BRCA-1 and BRCA-2, showed dose dependent cell cycle arrest upon Olaparib treatment. These finding strongly suggest regulatory mechanism different from BRCA expression at the protein level.

### 8.1.2 PARP inhibition induces DNA damage

We next assessed accumulation of DNA damage mediated by PARP inhibition in AML cell lines, and therefore performed screens measuring DNA damage by comet assay and immunofluorescence-based gH2AX high content screening. Interestingly, we observed DNA damage upon Olaparib treatment in all AML cell lines at doses of 2.5 µM of Olaparib and below. These data indicated a dose-dependent response upon Olaparib treatment and validated the effectiveness of Olaparib treatment. We also screened all the AML cell lines for potential Olaparib-mediated cell cycle changes and cell cycle phase-specific DNA damage accumulation. We observed heterogenous cell cycle profiles, but all cell lines displayed a specific increase of gH2AX foci in S and G2 cell cycle phases. This damage accumulation was time and dose dependent.

Interestingly, *TP53*-mutated cell lines (HL-60, THP-1 and NOMO-1) accumulated slightly higher amounts of gH2AX foci compared to *TP53* wild-type and "BRCA-low" expressing cell lines (MOLM-13, MV4-11 and OCI-AML-3). This is in line with the characteristic function of p53 to regulate cell cycle and would argue that upon p53 loss these cell lines become genomic instable (Prokocimer et al., 2017). However, these effects were minor and likely do not explain the observed effects upon PARP inhibition. Moreover, *TP53* wild-type OCI-AML-2 cells was the best responder of all cell lines and also argues against a specific role of *TP53* mutational status.

### 8.1.3 AML cell lines tend towards NHEJ to mediate DNA damage

We next speculated whether DNA damage in *TP53* wild-type and "BRCA-low" cell lines mitigated was mediated by a given DNA repair pathway and/or replicative stress. In order to address this questions, we measured 53BP1 foci accumulation, a known biomarker for NHEJ pathway (Botuyan et al., 2018; Cseh, Fabian, Sumegi, & Scorrano, 2017; Cuella-Martin et al., 2016; Lord et al., 2015) and pRPA (known biomarker for replicative stress) in a cell cycle-dependent manner (Branzei & Foiani, 2008) upon Olaparib treatment.

DSBs during the G1-phase need to be repaired before the onset of replication, which is triggered by the activation kinases like DNA-PK, ATM and ATR depending on the type of damage (Branzei & Foiani, 2008). In NHEJ, the Ku-proteins (Ku70 and Ku80) bind to both ends of a DSB and recruit DNA-PK catalytic subunit and LIG4–XRCC4 to ligate and subsequently complete DNA repair. As a lack of the sister chromatid and the presence of highly compacted chromatin, NHEJ is therefore preferentially performed in G1 phase. The increased recruitment of 53BP1 at the site of damage, is a surrogate for active NHEJ as 53BP1 inhibits DNA resection and thereby promotes NHEJ in G1-phase of cell cycle (Botuyan et al., 2018; Branzei & Foiani, 2008; Cuella-Martin et al., 2016). On the other hand, during S and G2 phase of cell cycle, preferentially activate cyclin-dependent kinase (CDK) promoting DSB resection, exposing 3' overhangs of ssDNA. These ssDNA overhangs are coated with RPA and replaced by RAD51 forming presynaptic filaments that initiate HR by invading the homologous region of sister chromatid (Branzei & Foiani, 2008; Diamant et al., 2012; Escribano-Diaz et al., 2013).

In our screen, we found that all cell lines accumulated gH2AX and 53BP1 foci in all the cell cycle phases but particularly enriched in S and G2 phases. Additionally, Olaparib treatment induced replicative stress with higher pRPA foci across all cycle phases in AML cells. Observing higher 53BP1 foci in S and G2 phases suggested that these cells might have a dysfunctional HR-based repair and are dependent on NHEJ pathways to repair PARP inhibitor-mediated DNA damage.

A time-kinetics treatment with Olaparib performed in MV4-11 cells, showed an increasing pattern of S and G2 phase accumulation of gH2AX foci. But intriguingly gH2AX foci was moderately diminished in G2 compared to S phase and significantly lowered in G1 phase. Taken together with increased 53BP1 and pRPA in S and G2 phase along with incremental accumulation gH2AX overtime suggest that these cells might be employing DNA damage tolerance or bypass pathways such as translesion synthesis (TLS) and/or template switch (TS) in order to repair in the late replicative stage (Branzei & Foiani, 2008).

Nucleotide-excision repair (NER) is mainly responsible in removing bulky DNA lesions (O'Connor, 2015) caused by UV, IR or trapped PARP during the G1 phase. Unrepaired bulky lesions from G1 carried forward into S phase and newly accumulated DSBs in S phase can hinder the ongoing replication fork leading to a S-G2 phase accumulation. Alternatively, absence or unavailability of adequate HR repair proteins ongoing replication proceeds by bypassing these lesions using error prone TLS polymerases like, Y-family of DNA polymerases (POLH, POLI, POLK and Rev1) and on the B-family member, POLZ for complete bypass of DNA lesions (Bertolin, Mansilla, & Gottifredi, 2015; Bi, 2015; Ghosal & Chen, 2013). On the other hand, TS pathway utilizes undamaged information from sister chromatid and repairs DNA lesions post replication, in an error-free manner. Both TLS and TS pathways are carried out post replication in late S-phase to G2 phase making sure cells do not transition from G2 to mitotic phase with accumulated damage by the means of covalent modifications of proliferating cell nuclear antigen (PCNA) (Bertolin et al., 2015; Branzei & Foiani, 2008).

This potential mechanism of DNA damage bypass and cell cycle progression is poorly understood and warrants the need to be validated in our model. Although the direct validation of TLS-dependent damage bypass is not possible with the currently available methods, it is possible to infer indirectly by measuring ubiquitinated-PCNA in the chromatin fraction, and expression of negative regulators such as PRLD1 (*PRELID1*), p21 and DVC1/SPTRN (SprT-Like Domain-Containing Protein Spartan) specifically in S and G2 cell cycle phase (Bertolin et al., 2015; Bi, 2015).

OCI-AML-3 cell lines did not show any effects of cell growth or cell death upon PARP inhibition, even though these cells accumulated gH2AX foci upon Olaparib treatment. Interestingly, these cells had very low numbers of 53BP1 foci in all the cell cycle phase, which could argue for a classical PARP-resistance phenotype by decreasing 53BP1 recruitment to the site of damage, and thereby enforcing HR-mediated DNA repair pathway (Mateo et al., 2019). Another marker for PARP resistance would be rescue of HR-mediated repair by RAD-51 (Mateo et al., 2019). We tried to measure RAD-51 foci using high content screening, but most of the antibody staining was observed in the cytoplasm and no distinct foci formation within the nucleus. Further experiments are required to answer this important question.

## 8.2 Role of p53 in regulation of DNA damage and apoptosis

p53 plays an important role in maintaining genomic integrity, thereby preventing tumorigenesis. Upon DNA damage, kinases like ATM, ATR are activated and further activate p53 and downstream proteins, such as p21 and regulate cell cycle progression. In normal cells, when DNA damage occurs, p53 and p21 regulate the cell cycle by inhibiting or slowing down on-going replicative outburst in S-phase (Branzei & Foiani, 2008; Maya-Mendoza et al., 2018). This S-phase conditional arrest potentially provides cells with vital time to repair accumulated damage by HR pathways which is the preferred pathway in S and G2 cell cycle phase. Once the damage is repaired, p21 is degraded and cells are released into the G2-M transition phase. If the cells were not able to repair all the damage, activated p53 employs and activates the pro-apoptotic downstream effectors such as NOXA and PUMA to activate the pro-apoptotic signals leading to eventual cell death (Bock & Tait, 2020; Ray Chaudhuri & Nussenzweig, 2017).

PARP1 plays an essential role in deciding cell fate, as it PARylates p53 and is sequestered in the nucleus and furthermore enhances p53 mediated transcription of DDR genes. The model, that PARP inhibition leads to replicative fork stalling and collapse, was challenged by a recent work of … (Maya-Mendoza et al., 2018). They showed that, PARP inhibition leads to accelerated replicative fork progression at lower doses with an acceleration up to 40% compared to untreated cells. After 40% increase in fork speed,

cells face replicative stress induced DNA damage. Also, upon PARP inhibition replicative forks were not observed, suggesting that DNA damage sensing function of PARylation was lost upon PARP inhibition. This phenomenon might explain why DNA damage likely mediated by replication stress increases in some AML cell lines (MV4-11, MOLM-13, and OCI-AML-3 cells) but is bypassed during S- and G2 phases of the cell cycle and almost completely gone in G1 upon PARP inhibition.

Furthermore, PARP1 physically binds p21 and acts as a co-repressor at the *CDKN1A* (*p21*) gene promotor. Upon PARP inhibition trapped PARP causes bulky adducts that need to be repaired. Activated p53 transactivates p21 causing p21-mediated regulation ofcell cycle arrest, replicative fork speed and inhibition of DNA synthesis by binding of PCNA (Diamant et al., 2012; Maya-Mendoza et al., 2018; Sheng et al., 2019). Interestingly, cyclin dependent kinase (CDK) and PCNA binding domains of p21 are involved in regulating TLS. This regulation is essential as in the absence of DNA damage, p21 hinders the loading of error-prone TLS polymerases like POLE (polymerase eta), but in case of un-repaired bulky adducts, where TLS plays a crucial role mitigating damage, p21 progressively degrades and gradually releases replication fork blockade (Livneh, 2006; Roos, Thomas, & Kaina, 2016; Sheng et al., 2019).

## 8.3 Relevance of BH3 inhibitors in AML

p53 acts as a master regulator of apoptotic cell death and is inactivated in 50% of solid tumors (Prokocimer et al., 2017). Interestingly, *TP53* is mutated or depleted only in a small fraction of AML patients. p53 promotes apoptotic cell death induced by genotoxins or replicative stress. This effect is executed in part by activating BAK- and BAX-mediated intrinsic apoptosis (Bock & Tait, 2020). As most of the AML cell lines accumulate DNA damage in a time- and dose-dependent manner and manage to evade apoptosis, we speculated that anti-apoptotic proteins might be an interesting target to overcome resistance to apoptosis. In line with literature, anti-apoptotic proteins like BCL2 are highly expressed in AML cells (Konopleva & Letai, 2018; Pullarkat & Newman, 2016) compared to normal blood and somatic cells.

Therefore, we evaluated a potential dependency of AML cell lines on anti-apoptotic proteins by using specific small molecule inhibitors. We treated all AML cell lines with Venetoclax, a potent BCL2 inhibitor and observed substantial responses in most of the cell lines except THP-1 and OCI-AML-3 cells. It was recently reported (Bogenberger et al., 2017) that both cell lines are resistant to Venetoclax, hence we speculated they might be dependent on other anti-apoptotic protein such as MCL1 or BCL-xL. Hence, we screened AML cell lines by using a dose response-based dependency screen and found that cell lines responded to MCL1 inhibitor (S63854) at varying doses but none of them responded to BCL-xL inhibitor (WEHI-576). Interestingly, THP-1 and OCI-AML-3 cells responded well to MCL1 inhibition.

## 8.4 Combining PARP inhibition and BCL2 inhibition

To overcome tolerance to PARP inhibition-mediated DNA damage, in particular in *TP53* wild type but also mutant cell lines, we speculated that targeting anti-apoptotic BH3 proteins could sensitize AML cell lines to PARP inhibition, indicating that there might be an inherent dependency on anti-apoptotic proteins essential to tolerate genotoxins. Therefore, we performed combinatorial intervention of Olaparib and Venetoclax to proof synergistic effects with respect to the induction of apoptosis. Indeed, we observed strong synergistic effects upon combining Olaparib and Venetoclax in MV4-11, MOLM-13, and OCI-AML-2 cell lines. We also observed a similar activation of p53 upon Olaparib treatment, which could further contribute to the observed synergistic effects, but p53 activation alone is not able to induce cell death.

Olaparib was also evaluated in combination with the FLT3 inhibitors Midostaurin and Quizartinib (Daver et al., 2019; Maifrede et al., 2018) in FLT3-mutant MV4-11 and MOLM-13 cells. Combined treatment showed a promising result in enhancing the efficacy of FLT3 inhibitors. This might be due to a FLT3 inhibition-mediated reduction of key DNA repair proteins such as BRCA1, BRCA2, RAD-51 and LIG4 (Dellomo et al., 2019; Maifrede et al., 2018). We further evaluated the effectiveness of Olaparib in combination with Venetoclax in comparison to FLT3 inhibitors in FLT3-ITD mutated cell lines MV4-11 and MOLM-13. Both of these inhibitors were effective against FLT3-ITD

mutant cells but the combination of Olaparib and Venetoclax outcompeted the Olaparib - FLT3-inhibitor combinations.

OCI-AML-3 cell lines did not respond to a combination of Olaparib and Venetoclax. These cells demonstrated p53 activation upon Olaparib treatment, but its reduced 53BP1 foci likely reinforcing HR mediated repair suggests a potential resistance mechanism to Olaparib treatment. On the other hand, p53 activation was minor at all dose levels. Recently, it was demonstrated (Pan et al., 2017), that p53 expression in OCI-AML-3 cells is low, but upon strong activation of p53 by MDM2 inhibition (idasanutlin), OCI-AML-3 cell regained BCL2 sensitively. In this work it was also demonstrated that inhibition of the Ras/Raf/MEK/ERK pathway resulted in proteasomal degradation of MCL1. Interestingly, increased levels of MCl1 is characterized as a potential resistance factor to evade apoptosis upon BCL2 inhibition. This finding is very insightful, as it hints towards a potential switch in anti-apoptotic dependency based on p53 expression and activation. As we demonstrated that OCI-AML-3 cells were resistant to Venetoclax but responsive to S63845, our data suggest that reduced expression of p53 might indicate MCL1 dependency. Therefore, we treated OCI-AML-3 cells with Olaparib and S63845 and observed a moderate response upon combination. As a proof of concept, we tested Olaparib treatment with and without Venetoclax or S63845 in THP-1 cells harboring a *TP53* mutation. Single Olaparib treatment caused a moderate response whereas the combination with S63845 but not Venetoclax was highly synergistic Figure 34

Taken together, our data indicate that inhibition of PARP causes substantial DNA damage but targeting of anti-apoptotic BH3-proteins might be required to overcome the anti-apoptotic threshold in AML cells causing cell death. Our data also indicate that effective combination therapy required the selection of the correct BH3 protein to target.

# 9. Conclusion

Based on our findings, we postulate a model schematically represented in Figure 33. FLT3 is mutated in about one third of cytogenetically normal karyotype AML. These cells are characterized increased cell proliferation and replicative stress. Targeting of FLT3 with Midostaurin (PKC 412) and Crenolanib often results in cell cycle arrest, diminishing replicative stress. In our model we take advantage of the endogenous high replicative rate and induce further DNA damage by PARP inhibition. As a next step we evaluate the inherent dependency of specific BH3 inhibitor targeting specific anti-apoptotic protein and utilizing the combinatorial synergy to induce cell death. Targeting these dependences might be an efficient alternative and an additional tool in the arsenal in AML therapeutics.

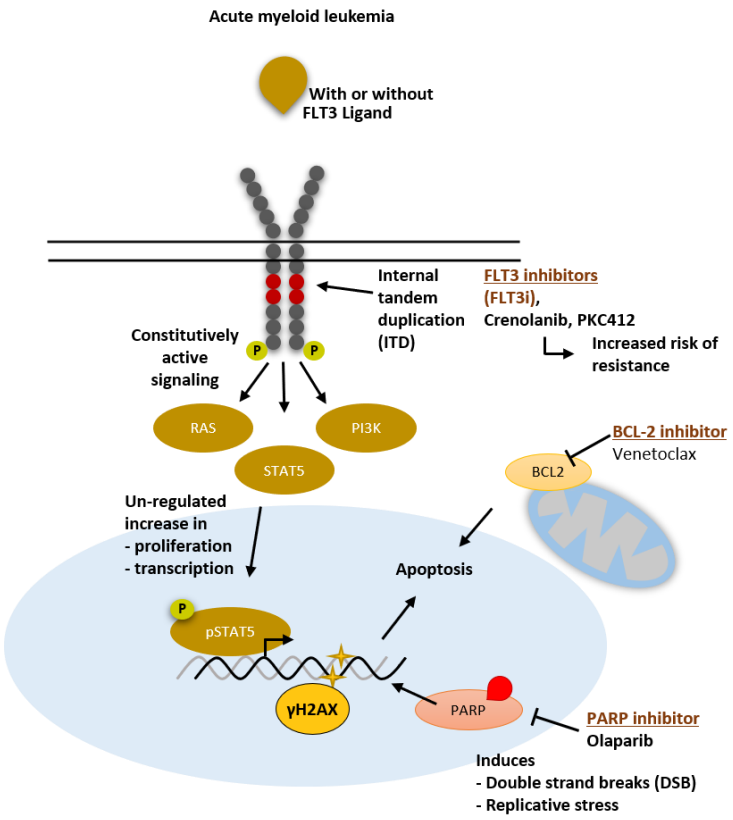


***Figure 33: Rationale for combining PARP and BCL2 inhibition.***

*Schematic representation of proposed model by which combined PARP and BCL2 inhibition is an effective strategy in targeting FLT3$^{mut}$ AML.*

# 10. Supplementary Figure

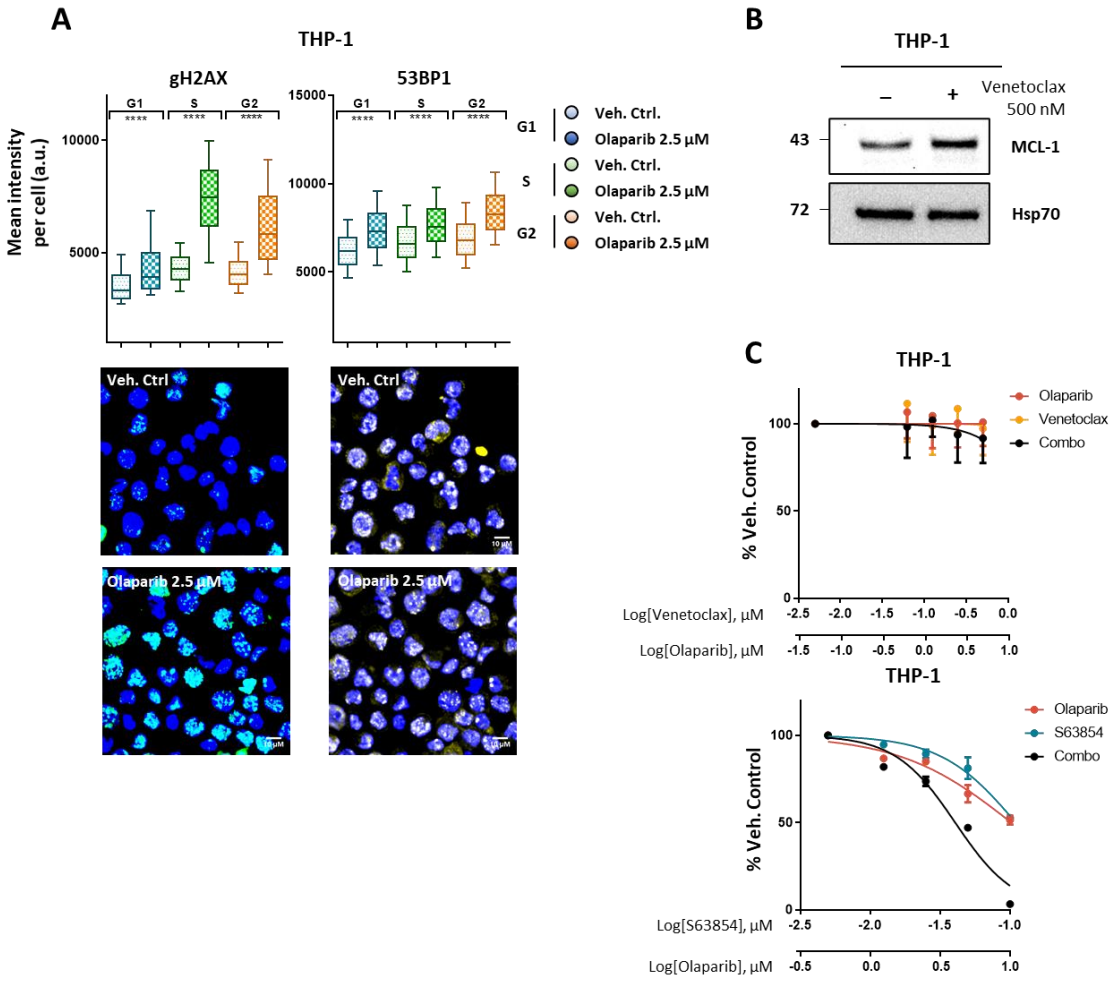


***Figure 34: Olaparib induces DNA damage in THP-1 cells and is sensitive for MCL1 inhibition***

*(A) Representative immunofluorescence of staining and cell cycle-dependent accumulation of gH2AX (Ser 139) and 53BP1 foci upon Olaparib treatment for 72 hr in THP-1 cells. p-values: **** indicate <0.0001; assessed by t-test using Welch's correction. (B) Immunoblot analysis for indicated proteins upon Venetoclax treatment for 24 h in THP-1 cells. (C) Dose response plots and for THP-1 cells upon combination treatment of Olaparib and Venetoclax in comparison with Olaparib and S63845 for 72 hr as indicated.*

# 11. List of Figures

# 12. List of Tables

# 13. Appendix

## 13.1 Material

### 13.1.1 Reagents for cell culture

| Media and Additives | Manufacturer |
|---|---|
| Dimethylsulfoxide | Sigma-Aldrich Corp. St. Louis, MO, USA |
| Fetal bovine serum (FBS) | Biochrome AG, Merck KGaA, Darmstadt |
| L-Glutamin (200mM) | GE Healthcare, PAA Laboratories GmbH, Pasching, Austria |

### 13.1.2 List of inhibitors

| Inhibitor | Target | Manufacturer |
|---|---|---|
| Olaparib | PARP1/2 | AstraZeneca, UK |
| Talazoparib | PARP1 | Pfizer, USA |
| Venetoclax | BCL2 | AbbVie Inc., USA |
| Navitoclax | BCL2, BCL-xL, BCL-W | AbbVie Inc., USA |
| S63845 | MCL1 | Servier LLC, France |
| WEHI-539 | BCL-xL | Cayman Chemicals |
| Midostaurin | FLT3-ITD | Novartis, Switzerland |
| Crenolanib | FLT3-ITD | Arog Pharmaceuticals, LLC |

### 13.1.3 Chemicals

| Chemical | Manufacturer |
|---|---|
| Acrylamide/Bisacrylamide | CarlRoth GmbH & Co. KG, Karlsruhe |

| | |
|---|---|
| Ammoniumpersulfate (APS) | Sigma-Aldrich Corp., St. Louis, MO, USA |
| Annexin V Apoptosis Detection Kit PE | Invitrogen by Thermo Fisher Scientific, Waltham, MA, USA |
| BD Facst Clean Solution | Becton Dickinson Bioscience, Heidelberg |
| β-Mercaptoethanol | Sigma-Aldrich Corp., St. Louis, MO, USA |
| Bovine Serum Albumin | Sigma-Aldrich Corp., St. Louis, MO, USA |
| Bradford-Solution | BioRad, Munich |
| Cell Proliferation Kit I (MTT) | Roche Diagnsotics GmbH, Mannheim |
| Pierce™ ECL Western Blotting Substrate | Thermo Scientific™ |
| 4′,6-diamidino-2-phenylindole (DAPI) | CarlRoth GmbH & Co. KG, Karlsruhe |
| Ethanol | CarlRoth GmbH & Co. KG, Karlsruhe |
| Ethylenediaminetetraacetic acid (EDTA) | CarlRoth GmbH & Co. KG, Karlsruhe |
| FACSFlow™ | Becton Dickinson Bioscience, Heidelberg |
| Gelatin | Sigma-Aldrich Corp., St. Louis, MO, USA |
| Glycin | AppliChem GmbH, Darmstadt |
| Hoechst 33342 | Invitrogen, Life Technologies, Carlsbad, CA, USA |
| Hydrochloric acid | CarlRoth GmbH & Co. KG, Karlsruhe |
| Isopropanol | Hedinger Aug. GmbH & Co. KG, Stuttgart |
| Methanol | AppliChem GmbH, Darmstadt |
| N,N,N′,N′-Tetramethylethane-1,2-diamine (TEMED) | Sigma-Aldrich Corp. St. Louis, MO, USA |
| PageRuler™ Prestained Protein Ladder | Thermo Scientific Waltham, MA, USA |
| Phosphate buffered saline (PBS) sterile | Sigma-Aldrich Corp. St. Louis, MO, USA |
| Poly-L-Lysine | Sigma-Aldrich Corp. St. Louis, MO, USA |
| Potassium chloride | Merck KGaA, Darmstadt |
| Potassium phospate | Merck KGaA, Darmstadt |
| Powdered milk | CarlRoth GmbH & Co. KG, Karlsruhe |
| Propidium iodide | Sigma-Aldrich Corp., St. Louis, MO, USA |
| Proteaseinhibitor | Roche Lifescience, Mannheim |

| | |
|---|---|
| Rinse Solution | Becton Dickinson Bioscience, Heidelberg |
| Shutdown Solution | Becton Dickinson Bioscience, Heidelberg |
| Sodium azide | CarlRoth GmbH & Co. KG, Karlsruhe |
| Sodium bicarbonate | Merck KGaA, Darmstadt |
| Sodium chloride | CarlRoth GmbH & Co. KG, Karlsruhe |
| Sodium citrate | Sigma-Aldrich Corp. St. Louis, Mo, USA |
| Sodium dihydrogen phosphate monohydrate | Merck KGaA, Darmstadt |
| Sodium dodecylsulfate (SDS) | CarlRoth GmbH & Co. KG, Karlsruhe |
| Sodium hydroxide | Merck KGaA, Darmstadt |
| Tris(hydroxymethyl)aminomethane (Tris) | CarlRoth GmbH & Co. KG, Karlsruhe |
| Triton-X-100 | Sigma-Aldrich Corp. St. Louis, MO, USA |
| Trypan blue | Sigma-Aldrich Corp. St. Louis, MO, USA |
| Tween®-20 | AppliChem GmbH, Darmstadt |

### 13.1.4 Solutions and buffers

| Name | Contents |
|---|---|
| Ammoniumpersulfate (APS) | 10% Ammoniumpersulfate in A. dest. |
| Blocking Solution (immunofluorescence) | 3% Bovine serum albumin (BSA) in PBS |
| Gel buffers (SDS-Page) | 1.5 M Tris (pH 8.8), Storage at 4 °C<br>1 M Tris (pH 6.8), Storage at 4 °C |
| Loading buffer 4x (laemmli buffer) | 250 mM Tris-HCl (pH 6.8)<br>8% (w/v) SDS<br>40 % (v/v) Glycerol<br>10 % (v/v) β-Mercaptoethanol<br>0.4 % (v/v) Bromphenol blue |
| Blocking buffer (Western blotting) | 5% (w/v) Milk powder in PBS |
| 10x Net-G | 0.5 M Tris<br>1.5 M NaCl<br>50 mM EDTA (pH 7,5) |

| | |
|---|---|
| | 0.4 % Gelantine<br>0.5 % Tween |
| 10x PBS | 1.37 M NaCl<br>27 mM KCl<br>100mM $Na_2HPO_4$<br>20mM $KH_2PO_4$<br>pH=7.8 |
| PBS/Tween (PBST) | PBS<br>0.1 % (v/v) Tween-20 |
| Complete™ Protease Inhibitor Cocktail (25x) | 1 Tablet (Roche) in 2 ml $H_2O$ |
| RIPA-Buffer – Protein lysis buffer | 50 mM Tris / HCl<br>150 mM NaCl<br>1% NP-40<br>0.1% Sodiumdesoxycholate<br>0.1 % SDS<br>1 mM EDTA<br>pH = 7.5 |
| Running buffer (SDS-Page) | 50 mM Tris<br>192 mM Glycerin<br>0.1 % (w/v) SDS |
| Transfer buffer (SDS-Page) | 50 mM Tris<br>192 mM Glycin<br>0.1 % (w/v) SDS<br>20 % (v/v) Methanol |
| Stripping solution (SDS-Page) | 62.5 mM Tris-HCl (pH 6.8)<br>2 % (w/v) SDS<br>100 mM β-Mercaptoethanol |
| Solubilization buffer (MTT) | 20 % (w/v) SDS<br>0.01 M HCl |
| High throughput Screening (HTS) buffer | 2.2 mM EDTA in PBS<br>0.1% DAPI |
| Lysis Buffer | 2.5 M NaCl |

| | |
|---|---|
| | 100 nM EDTA<br>10 nM Tris<br>1% Na-Laurylsarcosinat |
| 10x Neutral Electrophoresis buffer | 1 M Tris<br>3M Sodium Acetate<br>pH 9.0 |
| DNA precipitation buffer | 7.5 M Ammonium Acetate (in $ddH_2O$)<br>95% Ethanol |
| Staining buffer | 50 µg/mL (in $ddH_2O$) |

### 13.1.5 Antibody list

#### 13.1.5.1 Western blotting

| Primary Antibody | Size (kDa) | Host | Dilution | Catalogue number | Manufacturer |
|---|---|---|---|---|---|
| GAPDH | 35 | Rabbit | 1:1000 | cs-2118 | Abcam |
| p21 | 21 | Rabbit | 1:1000 | ab109520 | Abcam |
| p53 (DO-1) | 53 | Mouse | 1:200 | 2524 | Cell signalling |
| phospho-p53 (Ser15) | 55 | Rabbit | 1:1000 | 9284 | Cell signalling |
| BCL-2 | 26 | Rabbit | 1:1000 | 2872 | Cell Signalling |
| MCL-1 | 32/40 | Mouse | 1:200 | sc-12756 | Santa Cruz |
| BCL-xL | 38 | Rabbit | 1:200 | 2764 | Cell Signalling |
| PARP-1 | 89/116 | Rabbit | 1:1000 | 9532 | Cell Signalling |
| BRCA-1 | 220 | Mouse | 1:500 | OP92-100µg | Millipore |
| BRCA-2 | 380 | Mouse | 1:200 | sc-293185 | Santa Cruz |
| KU-70 | 70 | Mouse | 1:200 | sc-17789 | Santa Cruz |
| KU-80 | 86 | Rabbit | 1:200 | sc-9034 | Santa Cruz |
| HSP-70 | 70 | Mouse | 1:500 | HSP01 | Oncogene |

| Secondary Antibody | Host | Dilution | Catalogue number | Manufacturer |
|---|---|---|---|---|
| Anti-Mouse IgG HRP-conjugated | Goat | 1:2500 | 7076 | Cell Signaling. |
| IgG anti-rabbit (H+L) | Goat | 1:10000 | 074-1516 | KPL, Kirkegaard & Perry Laboratories Inc., Gaithersburg, MD, USA |
| Pierce™ ECL Western Blotting Substrate | Not applicable (na) | na | 32106 | Thermo Scientific™ |

### 13.1.5.2 Immunofluorescence

| Primary Antibody | Host | Dilution | Catalogue number | Manufacturer |
|---|---|---|---|---|
| phospho-Histone H2A.X (Ser139) | Mouse | 1:1000 | 05-636 | Millipore |
| phospho-Histone H2A.X (Ser139) | Rabbit | 1:1000 | 9717 | Cell signalling |
| 53BP1 | Rabbit | 1:1000 | NB100-304 | Novusbio |
| Phosphor-RPA (S4/S8) | Rabbit | 1:2000 | A300-245A | Bethyl Laboratories |
| RAD51 | Rabbit | 1:100 | sc-8349 | Santa Cruz |
| RAD51 | Rabbit | 1:500 | 70-001 | Bio Academica |

| Secondary Antibody | Host | Dilution | Catalogue number | Manufacturer |
|---|---|---|---|---|
| Hoechst 33342 | Not applicable | 1:2000 | 11534886 | Invitrogen™ H3570 |
| Anti-Mouse Alexa 488 | Donkey | 1:1000 | A21202 | Invitrogen |
| Anti-Rabbit Alexa 568 | Goat | 1:2000 | A11011 | Invitrogen |

### 13.1.6 shRNA sequences

| Target | label | Sequence | Reference |
|---|---|---|---|
| BRCA-1 | shBRCA1_#1 | CAATATGGAACTCGAATTAAA | TRCN0000244985 |
| BRCA-1 | **shBRCA1_#2*** | ACTGATACTGCTGGGTATAAT | TRCN0000244987 |
| Scramble control | **shSCR*** | Not available | TRIPZ inducible lentiviral control RHS4743 |

*shBRCA1_#2 and shSCR data is shown in Figure 25 F-G.

### 13.1.7 Primer list

| Target | Forward sequence | Reverse sequence |
|---|---|---|
| NOXA | ATGAATGCACCTTCACATTCCTCT | TCCAGCAGAGCTGGAAGTCGAGTGT |
| PUMA | GACTGTGAATCCTGTGCTCGTC | CGTCGCTCTCTCTAAACCTATGC |
| BCL-2 | ATGTGTGTGGAGAGCGTCAA | TTCAGAGACAGCCAGGAGAAA |
| MCL-1 | AAGCCAATGGGCAGGTCT | TGTCCAGTTTCCGAAGCAT |
| BCL-xL | GGCTGGGATACTTTTGTGGA | TGTCTGGTCATTTCCGACTG |
| GAPDH | GCTCTCTGCTCCTCCTGTTC | ACGACCAAATCCGTTGACTC |

### 13.1.8 Devices

| Device | Manufacturer |
|---|---|
| ELISA reader | Dynex Technologies |
| Photometer | GE Healthcare „GeneQuant Pro |
| Chemiluminescence Imager | Intas |
| Flow Cytometer | Becton Dickinson (BD) FACS Canto,<br>Becton Dickinson (BD) FACS Canto II |

| | |
|---|---|
| Cell irradiator | Buchler „CDCK 4905“ |
| Incubator | |
| Electrophoresis system | Biorad |
| Magnetic stirrer | Heidolph „MR3001“ |
| Microscope | Olympus „CHT“ |
| Microscope (Immunofluorescence imaging) | Zeiss LSM 710 |
| High content screening (HCS) | OperaPhenix™ |
| pH meter | Hanna-Instruments „pH211“ |
| Pipets | Eppendorf, Gilson, Integra Biosciences „Pipetboy accu“ |
| Protein transfer system | Biorad „Mini Trans-Blot Cell“ |
| Sterile bench | Thermo Scientific „HeraSafe KS18“ |
| Liquid nitrogen tank | Air Liquid, „Espace 151 Liquide” |
| Vortex | Neolab |
| Thermomixer (for reaction tubes) | Eppendorf |
| Waterbath | Köttermann |
| Scales | VWR International |
| Neubauer chamber | Paul Marienfeld GmbH & Co.KG |
| Centrifuges | Roth, „Micro Centrifuge“<br>Thermo Scientific “Heraeus Fresco 17” |

### 13.1.9 Disposables

| Disposable | Manufacturer |
|---|---|

| | |
|---|---|
| 6-, 12-, 24-, 96-well-plates | Greiner Bio-One GmbH, Kremsmünster, Austria |
| T-75 flasks, T-25 flasks | Greiner Bio-One GmbH, Kremsmünster, Austria |
| Serological Pipets 5 ml, 10 ml, 25 ml | Corning Inc., Corning, NY, USA |
| Desinfectant | Schülke & Mayr GmbH, Norderstedt |
| Cryo vials 1 ml | Greiner Bio-One GmbH, Kremsmünster, Austria |
| Cryo vials | Nunc, Roskilde, Denmark |
| Cuvettes 1,6 ml | Ratiolab GmbH, Dreieich |
| Nitrocellulose membrane | GE Healthcare UK Limited, Amersham Place, Buckinghamshire, UK |
| Pasteur pipets | CarlRoth GmbH & Co. KG, Karlsruhe |
| Pipet tips 10 µl, 200 µl, 1000 µl | Starlab GmbH, Hamburg |
| Pipet tips 10 µl, 200 µl, 1000 µl | Greiner Bio-One GmbH, Kremsmünster, Austria |
| Reaction tubes 1,5 ml, 2 ml | Greiner Bio-One GmbH, Kremsmünster, Austria |
| Tubes 15 ml, 50 ml | Cellstar, Greiner Bio-One GmbH, Kremsmünster, Austria |

### 13.1.10 Software and databases

| Software | Origin |
|---|---|
| EndNote X9 | Clarivate Analytics |
| ImageJ/Fiji | Wayne Rasband, National Institutes of Health, USA |
| FlowJo (version 10.6.1) | Tree Star Inc |
| Inkscape (1.0) | Inkscape.org |
| Harmony Software | Pelkin Elmer |
| R studio (version 3.6.3) | RStudio, Inc. |
| R-packages | |
| Pheatmaps (1.0.12) | cran.r-project.org |
| Synergyfinder | bioconductor |
| Graph Pad Prism (v8.4) | Graphpad Software, Inc. |
| FACS Diva | Becton-Dickinson |
| Microsoft Office 365 | Microsoft |

## 13.2 Gene lists

### 13.2.1 DNA damage gene list

| Gene symbol | Activity |
|---|---|
| Base excision repair (BER) | DNA glycosylases: major altered base released |
| UNG | U |
| SMUG1 | U |
| MBD4 | U or T opposite G at CpG sequences |
| TDG | U, T or ethenoC opposite G |

| | |
|---|---|
| OGG1 | 8-oxoG opposite C |
| MUTYH (MYH) | A opposite 8-oxoG |
| NTHL1 (NTH1) | Ring-saturated or fragmented pyrimidines |
| MPG | 3-meA, ethenoA, hypoxanthine |
| NEIL1 | Removes thymine glycol |
| NEIL2 | Removes oxidative products of pyrimidines |
| NEIL3 | Removes oxidative products of pyrimidines |

### Other BER and strand break joining factors

| | |
|---|---|
| APEX1 (APE1) | AP endonuclease |
| APEX2 | AP endonuclease |
| LIG3 | DNA Ligase III |
| XRCC1 | LIG3 accessory factor |
| PNKP | Converts some DNA breaks to ligatable ends |
| APLF (C2ORF13) | Accessory factor for DNA end-joining |

### Poly(ADP-ribose) polymerase enzymes that bind to DNA

| | |
|---|---|
| PARP1 (ADPRT) | Protects strand interruptions |
| PARP2 (ADPRTL2) | PARP-like enzyme |
| PARP3 (ADPRTL3) | PARP-like enzyme |

### Direct reversal of damage

| | |
|---|---|
| MGMT | O6-meG alkyltransferase |
| ALKBH2 (ABH2) | 1-meA dioxygenase |
| ALKBH3 (DEPC1) | 1-meA dioxygenase |

### Repair of DNA-topoisomerase crosslinks

| | |
|---|---|
| TDP1 | Removes 3'-tyrosylphosphate and 3'-phosphoglycolate from DNA; human disorder SCAN1 |
| TDP2 (TTRAP) | 5'- and 3'-tyrosyl DNA phosphodiesterase |

### Mismatch excision repair (MMR)

| | |
|---|---|
| MSH2 | Mismatch (MSH2-MSH6) and loop (MSH2-MSH3) recognition |

| | |
|---|---|
| MSH3 | |
| MSH6 | MSH2, MSH3, MSH6 |
| MLH1 | MutL homologs, forming heterodimer |
| | |
| PMS2 | MLH1, PMS2 |
| MSH4 | MutS homologs specialized for meiosis |
| | |
| MSH5 | MSH4, MSH5 |
| MLH3 | MutL homologs of unknown function |
| PMS1 | |
| PMS2L3 | MLH3, PMS1, PMS2L3 |

Nucleotide excision repair (NER)

| | |
|---|---|
| XPC | Binds DNA distortions |
| RAD23B | |
| CETN2 | XPC, RAD23B, CETN2 |
| RAD23A | Substitutes for RAD23B |
| XPA | Binds damaged DNA in preincision complex |
| DDB1 | Complex defective in XP group E |
| | |
| DDB2 (XPE) | DDB1, DDB2 |
| RPA1 | Binds DNA in preincision complex |
| RPA2 | |
| RPA3 | RPA1, RPA2, RPA3 |
| TFIIH | Catalyzes unwinding in preincision complex |
| ERCC3 (XPB) | 3' to 5' DNA helicase |
| ERCC2 (XPD) | 5' to 3' DNA helicase |
| GTF2H1 | Core TFIIH subunit p62 |
| GTF2H2 | Core TFIIH subunit p44 |
| GTF2H3 | Core TFIIH subunit p34 |
| GTF2H4 | Core TFIIH subunit p52 |
| GTF2H5 (TTDA) | Core TFIIH subunit p8 |
| CDK7 | Kinase subunits of TFIIH |
| CCNH | |
| MNAT1 | CDK7, CCNH, MNAT1 |

| | |
|---|---|
| TFIIH | Catalyzes unwinding in preincision complex |
| ERCC5 (XPG) | 3' incision |
| ERCC1 | 5' incision DNA binding subunit |
| ERCC4 (XPF) | 5' incision catalytic subunit |
| LIG1 | DNA ligase |
| | |
| NER-related | |
| ERCC8 (CSA) | Cockayne syndrome and UV-Sensitive Syndrome; Needed for transcription-coupled NER |
| ERCC6 (CSB) | |
| UVSSA (KIAA1530) | ERCC8, ERCC6, UV-sensitive syndrome |
| XAB2 (HCNP) | XAB2 |
| MMS19 | Iron-sulfur cluster loading and transport |
| | |
| Homologous recombination | |
| RAD51 | Homologous pairing |
| RAD51B | Rad51 homolog |
| RAD51D | Rad51 homolog |
| DMC1 | Rad51 homolog, meiosis |
| XRCC2 | DNA break and crosslink repair |
| | |
| XRCC3 | XRCC2, XRCC3 |
| RAD52 | Accessory factors for recombination |
| RAD54L | |
| RAD54B | RAD52, RAD54L, RAD54B |
| BRCA1 | Accessory factor for transcription and recombination, E3 Ubiquitin ligase |
| SHFM1 (DSS1) | BRCA2 associated |
| RAD50 | ATPase in complex with MRE11A, NBS1 |
| MRE11A | 3' exonuclease, defective in ATLD (ataxia-telangiectasia-like disorder) |
| NBN (NBS1) | Mutated in Nijmegen breakage syndrome |
| RBBP8 (CtIP) | Promotes DNA end resection |
| MUS81 | Subunits of structure-specific DNA nuclease |

| | |
|---|---|
| EME1 (MMS4L) | |
| EME2 | MUS81, EME1, EME2 |
| GIYD1 (SLX1A) | subunit of SLX1-SLX4 structure-specific nuclease, two identical tandem genes in the human genome |
| GIYD2 (SLX1B) | |
| GEN1 | Nuclease cleaving Holliday junctions |

Fanconi anemia

| | |
|---|---|
| FANCA | FANCA |
| FANCB | FANCB |
| FANCC | FANCC |
| BRCA2 (FANCD1) | Cooperation with RAD51, essential function |
| FANCD2 | target for monoubiquitination |
| FANCE | FANCE |
| FANCF | FANCF |
| FANCG (XRCC9) | FANCG |
| FANCI (KIAA1794) | target for monoubiquitination |
| BRIP1 (FANCJ) | DNA helicase, BRCA1-interacting |
| FANCL | FANCL |
| FANCM | helicase/translocase |
| PALB2 (FANCN) | co-localizes with BRCA2 (FANCD1) |
| RAD51C (FANCO) | Rad51 homolog FANCO |
| BTBD12 (SLX4) (FANCP) | nuclease subunit/scaffold BTBD12 (SLX4) FANCP |
| FAAP20 (C1orf86) | FANCA - associated |
| FAAP24 (C19orf40) | FAAP24 |

Non-homologous end-joining

| | |
|---|---|
| XRCC6 (Ku70) | DNA end binding subunit |
| XRCC5 (Ku80) | DNA end binding subunit |
| PRKDC | DNA-dependent protein kinase catalytic subunit |

| | |
|---|---|
| LIG4 | Ligase |
| XRCC4 | Ligase accessory factor |
| DCLRE1C (Artemis) | Nuclease |
| NHEJ1 (XLF, Cernunnos) | End-joining factor |

### Modulation of nucleotide pools

| | |
|---|---|
| NUDT1 (MTH1) | 8-oxoGTPase |
| DUT | dUTPase |
| RRM2B (p53R2) | p53-inducible ribonucleotide reductase small subunit 2 homolog |

### DNA polymerases (catalytic subunits)

| | |
|---|---|
| POLB | BER in nuclear DNA |
| POLG | BER in mitochondrial DNA |
| POLD1 | NER and MMR |
| | |
| POLE | POLD1, POLE1 |
| PCNA | Sliding clamp for pol delta and pol epsilon |
| REV3L (POLZ) | DNA pol zeta catalytic subunit, essential function |
| MAD2L2 (REV7) | DNA pol zeta subunit |
| REV1L (REV1) | dCMP transferase |
| POLH | xeroderma pigmentosum (XP) variant |
| POLI (RAD30B) | Lesion bypass |
| POLQ | Sensitivity to ionizing radiation |
| POLK (DINB1) | Lesion bypass and NER |
| POLL | Gap-filling during non-homologous end-joining |
| POLM | Gap filling during non-homologous end-joining |
| POLN (POL4P) | DNA crosslink repair |

### Editing and processing nucleases

| | |
|---|---|
| FEN1 (DNase IV) | 5' nuclease |
| FAN1 (MTMR15) | 5' nuclease interacting with FANCD2 |
| TREX1 (DNase III) | 3' exonuclease |

| | |
|---|---|
| TREX2 | 3' exonuclease |
| EXO1 (HEX1) | 5' exonuclease |
| APTX (aprataxin) | Processing of DNA single-strand interruptions |
| SPO11 | endonuclease |
| ENDOV | incision 3' of hypoxanthine and uracil in DNA and inosine in RNA |

Ubiquitination and modification

| | |
|---|---|
| UBE2A (RAD6A) | Ubiquitin-conjugating enzyme |
| UBE2B (RAD6B) | Ubiquitin-conjugating enzyme |
| RAD18 | E3 ubiquitin ligase |
| SHPRH | E3 ubiquitin ligase, SWI/SNF related, homolog of S. cerevisiae Rad5 |
| HLTF (SMARCA3) | E3 ubiquitin ligase, SWI/SNF related, homolog of S. cerevisiae Rad5 |
| RNF168 | E3 ubiquitin ligase for DSB repair; ATM-like and RIDDLE syndrome |
| SPRTN (c1orf124) | Reads ubiquitylation |
| RNF8 | E3 ubiquitin ligase for DSB repair |
| RNF4 | E3 ubiquitin ligase |
| UBE2V2 (MMS2) | Ubiquitin-conjugating complex |
| UBE2N (UBC13) | UBE2V2, UBE2N |

Chromatin Structure and Modification

| | |
|---|---|
| H2AFX (H2AX) | Histone, phosphorylated after DNA damage |
| CHAF1A (CAF1) | Chromatin assembly factor |
| SETMAR (METNASE) | DNA damage-associated histone methylase and nuclease |

Genes defective in diseases associated with sensitivity to DNA damaging agents

| | |
|---|---|
| BLM | Bloom syndrome helicase |
| WRN | Werner syndrome helicase / 3' - exonuclease |
| RECQL4 | Rothmund-Thompson syndrome |
| ATM | ataxia telangiectasia |
| TTDN1 (C7orf11) | non-photosensitive form of trichothiodystrophy |

| Other identified genes with known or suspected DNA repair function | |
|---|---|
| DCLRE1A (SNM1) | DNA crosslink repair |
| DCLRE1B (SNM1B) | Related to SNM1 |
| RPA4 | Similar to RPA2 |
| PRPF19 (PSO4) | DNA crosslink repair; binding to SETMAR |
| RECQL (RECQ1) | DNA helicase |
| RECQL5 | DNA helicase |
| HELQ (HEL308) | DNA helicase |
| RDM1 (RAD52B) | Similar to RAD52 |
| OBFC2B (SSB1) | Single-stranded DNA binding protein |

| Other conserved DNA damage response genes | |
|---|---|
| ATR | ATM- and PI-3K-like essential kinase |
| ATRIP | ATR-interacting protein |
| MDC1 | Mediator of DNA damage checkpoint |
| RAD1 | subunits of PCNA-like sensor of damaged DNA |
| RAD9A | |
| HUS1 | RAD1, RAD9, HUS1 |
| RAD17 (RAD24) | RFC-like DNA damage sensor |
| CHEK1 | Effector kinases |
| CHEK2 | CHEK1, CHEK2 |
| TP53 | Regulation of the cell cycle |
| TP53BP1 (53BP1) | chromatin-binding checkpoint protein |
| RIF1 | suppressor of 5'-end-resection |
| TOPBP1 | DNA damage checkpoint control |
| CLK2 | S-phase check point and biological clock protein |
| PER1 | S-phase check point and biological clock protein |

### 13.2.2 Apoptosis gene list

| Gene symbol | Alias |
|---|---|
| **Extrinsic apoptosis pathway** | |
| FAS | TNFRSF6 |
| FASLG | FASL/TNFSF6 |
| TNFRSF10A | TRAILR1/DR4 |
| TNFRSF10B | TRAILR2/DR5 |
| TNFRSF10C | DCR1 |
| TNFRSF10D | DCR2 |
| TNFRSF11B | Osteoprotegerin |
| TNFSF10 | TRAIL |
| TNFRSF1A | TNFR1 |
| TNF | TNF-ALPHA |
| FADD | |
| CFLAR | FLIP |
| **Caspases** | |
| CASP1 | CASPASE 1 |
| CASP2 | CASPASE 2 |
| CASP3 | CASPASE 3 |
| CASP4 | CASPASE 4 |
| CASP5 | CASPASE 5 |
| CASP6 | CASPASE 6 |
| CASP7 | CASPASE 7 |
| CASP8 | CASPASE 8 |

| | |
|---|---|
| CASP9 | CASPASE 9 |
| CASP10 | CASPASE 10 |
| CASP14 | CASPASE 14 |
| **IAPs family** | |
| NAIP | BIRC1 |
| BIRC2 | CIAP1 |
| BIRC3 | CIAP2 |
| XIAP | BIRC4 |
| BIRC5 | SURVIVIN |
| BIRC6 | APOLLON |
| BIRC7 | LIVIN |
| **Mitochondrial apoptosis pathway** | |
| **Bcl-2 family** | |
| **Antiapoptotic members** | |
| BCL2 | Bcl-2 |
| MCL1 | Mcl-1 |
| BCL2L1 | BCLX; Bcl-x |
| BCL2L2 | BCL-W; Bcl-w |
| BCL2A1 | BFL1/A1 |
| BCL2L10 | BCL-B; Bcl-B |
| **Proapoptotic members** | |
| **BH Multidomain members** | |
| BAX | |
| BAK1 | BAK |
| BOK | |
| **BH3-only members** | |

| | |
|---|---|
| BID | |
| BCL2L11 | BIM |
| BMF | |
| BAD | |
| BIK | |
| HRK | |
| PMAIP1 | NOXA |
| BNIP3 | |
| BNIP3L | |
| BCL2L14 | BCLG; Bcl-G |
| BBC3 | PUMA |
| BCL2L12 | |
| BCL2L13 | BCL-RAMBO |
| **Other proteins** | |
| APAF1 | |
| CYCS | Cytochrome C |
| DIABLO | SMAC/DIABLO |
| HTRA2 | OMI; PRSS25 |
| AIFM1 | AIF; PDCD8 |
| ENDOG | Endonuclease G |

# 14. Bibliography


Al-Lazikani, B., Banerji, U., & Workman, P. (2012). Combinatorial drug therapy for cancer in the post-genomic era. *Nature Biotechnology, 30*(7), 679-692. doi:10.1038/nbt.2284

Arai, H., Wada, R., Ishino, K., Kudo, M., Uchida, E., & Naito, Z. (2018). Expression of DNA damage response proteins in gastric cancer: Comprehensive protein profiling and histological analysis. *International Journal of Oncology, 52*(3), 978-988. doi:10.3892/ijo.2018.4238

Barretina, J., Caponigro, G., Stransky, N., Venkatesan, K., Margolin, A. A., Kim, S., . . . Garraway, L. A. (2012). The Cancer Cell Line Encyclopedia enables predictive modelling of anticancer drug sensitivity. *Nature, 483*(7391), 603-607. doi:10.1038/nature11003

Bertolin, A. P., Mansilla, S. F., & Gottifredi, V. (2015). The identification of translesion DNA synthesis regulators: Inhibitors in the spotlight. *DNA Repair (Amst), 32*, 158-164. doi:10.1016/j.dnarep.2015.04.027

Bi, X. (2015). Mechanism of DNA damage tolerance. *World Journal of Biological Chemistry, 6*(3), 48-56. doi:10.4331/wjbc.v6.i3.48

Binz, S. K., Lao, Y., Lowry, D. F., & Wold, M. S. (2003). The phosphorylation domain of the 32-kDa subunit of replication protein A (RPA) modulates RPA-DNA interactions. Evidence for an intersubunit interaction. *Journal of Biological Chemistry, 278*(37), 35584-35591. doi:10.1074/jbc.M305388200

BLISS, C. I. (1939). THE TOXICITY OF POISONS APPLIED JOINTLY1. *Annals of Applied Biology, 26*(3), 585-615. doi:10.1111/j.1744-7348.1939.tb06990.x

Bock, F. J., & Tait, S. W. G. (2020). Mitochondria as multifaceted regulators of cell death. *Nature Reviews: Molecular Cell Biology, 21*(2), 85-100. doi:10.1038/s41580-019-0173-8

Bogenberger, J., Whatcott, C., Hansen, N., Delman, D., Shi, C. X., Kim, W., . . . Tibes, R. (2017). Combined venetoclax and alvocidib in acute myeloid leukemia. *Oncotarget, 8*(63), 107206-107222. doi:10.18632/oncotarget.22284

Botuyan, M. V., Cui, G., Drane, P., Oliveira, C., Detappe, A., Brault, M. E., . . . Mer, G. (2018). Mechanism of 53BP1 activity regulation by RNA-binding TIRR and a designer protein. *Nature Structural & Molecular Biology, 25*(7), 591-600. doi:10.1038/s41594-018-0083-z

Branzei, D., & Foiani, M. (2008). Regulation of DNA repair throughout the cell cycle. *Nature Reviews: Molecular Cell Biology, 9*(4), 297-308. doi:10.1038/nrm2351

Brown, J. S., O'Carrigan, B., Jackson, S. P., & Yap, T. A. (2017). Targeting DNA Repair in Cancer: Beyond PARP Inhibitors. *Cancer Discovery, 7*(1), 20-37. doi:10.1158/2159-8290.CD-16-0860

Bryant, H. E., Schultz, N., Thomas, H. D., Parker, K. M., Flower, D., Lopez, E., . . . Helleday, T. (2005). Specific killing of BRCA2-deficient tumours with inhibitors of poly(ADP-ribose) polymerase. *Nature, 434*(7035), 913-917. doi:10.1038/nature03443

Cassier, P. A., Castets, M., Belhabri, A., & Vey, N. (2017). Targeting apoptosis in acute myeloid leukaemia. *British Journal of Cancer, 117*(8), 1089-1098. doi:10.1038/bjc.2017.281

Caulfield, S. E., Davis, C. C., & Byers, K. F. (2019). Olaparib: A Novel Therapy for Metastatic Breast Cancer in Patients With a BRCA1/2 Mutation. *Journal of the advanced practitioner in oncology, 10*(2), 167-174.

Caulfield, S. E., Davis, C. C., & Byers, K. F. (2019). Olaparib: A Novel Therapy for Metastatic Breast Cancer in Patients With a BRCA1/2 Mutation. *Journal of the advanced practitioner in oncology, 10*(2), 167-174.

Ceredig, R., Rolink, A. G., & Brown, G. (2009). Models of haematopoiesis: seeing the wood for the trees. *Nature Reviews: Immunology, 9*(4), 293-300. doi:10.1038/nri2525

Certo, M., Del Gaizo Moore, V., Nishino, M., Wei, G., Korsmeyer, S., Armstrong, S. A., & Letai, A. (2006). Mitochondria primed by death signals determine cellular addiction to antiapoptotic BCL-2 family members. *Cancer Cell, 9*(5), 351-365. doi:10.1016/j.ccr.2006.03.027

Chang, H. H. Y., Pannunzio, N. R., Adachi, N., & Lieber, M. R. (2017). Non-homologous DNA end joining and alternative pathways to double-strand break repair. *Nature Reviews: Molecular Cell Biology, 18*(8), 495-506. doi:10.1038/nrm.2017.48

Chao, H. X., Poovey, C. E., Privette, A. A., Grant, G. D., Chao, H. Y., Cook, J. G., & Purvis, J. E. (2017). Orchestration of DNA Damage Checkpoint Dynamics across the Human Cell Cycle. *Cell Syst, 5*(5), 445-459 e445. doi:10.1016/j.cels.2017.09.015

Chou, T. C. (2006). Theoretical basis, experimental design, and computerized simulation of synergism and antagonism in drug combination studies. *Pharmacological Reviews, 58*(3), 621-681. doi:10.1124/pr.58.3.10

Ciccarone, F., Zampieri, M., & Caiafa, P. (2017). PARP1 orchestrates epigenetic events setting up chromatin domains. *Seminars in Cell and Developmental Biology, 63*, 123-134. doi:10.1016/j.semcdb.2016.11.010

Costanzo, V. (2011). Brca2, Rad51 and Mre11: performing balancing acts on replication forks. *DNA Repair (Amst), 10*(10), 1060-1065. doi:10.1016/j.dnarep.2011.07.009

Crane, G. M., Jeffery, E., & Morrison, S. J. (2017). Adult haematopoietic stem cell niches. *Nature Reviews: Immunology, 17*(9), 573-590. doi:10.1038/nri.2017.53

Cseh, A. M., Fabian, Z., Sumegi, B., & Scorrano, L. (2017). Poly(adenosine diphosphate-ribose) polymerase as therapeutic target: lessons learned from its inhibitors. *Oncotarget, 8*(30), 50221-50239. doi:10.18632/oncotarget.16859

Cuella-Martin, R., Oliveira, C., Lockstone, H. E., Snellenberg, S., Grolmusova, N., & Chapman, J. R. (2016). 53BP1 Integrates DNA Repair and p53-Dependent Cell Fate Decisions via Distinct Mechanisms. *Molecular Cell, 64*(1), 51-64. doi:10.1016/j.molcel.2016.08.002

Daver, N., Cortes, J., Ravandi, F., Patel, K. P., Burger, J. A., Konopleva, M., & Kantarjian, H. (2015). Secondary mutations as mediators of resistance to targeted therapy in leukemia. *Blood, 125*(21), 3236-3245. doi:10.1182/blood-2014-10-605808

Daver, N., Schlenk, R. F., Russell, N. H., & Levis, M. J. (2019). Targeting FLT3 mutations in AML: review of current knowledge and evidence. *Leukemia, 33*(2), 299-312. doi:10.1038/s41375-018-0357-9

De Kouchkovsky, I., & Abdul-Hay, M. (2016). 'Acute myeloid leukemia: a comprehensive review and 2016 update'. *Blood Cancer Journal, 6*(7), e441. doi:10.1038/bcj.2016.50

Dellomo, A. J., Baer, M. R., & Rassool, F. V. (2019). Partnering with PARP inhibitors in acute myeloid leukemia with FLT3-ITD. *Cancer Letters, 454*, 171-178. doi:10.1016/j.canlet.2019.03.048

Diamant, N., Hendel, A., Vered, I., Carell, T., Reissner, T., de Wind, N., . . . Livneh, Z. (2012). DNA damage bypass operates in the S and G2 phases of the cell cycle and exhibits differential mutagenicity. *Nucleic Acids Research, 40*(1), 170-180. doi:10.1093/nar/gkr596

Dohner, H., Weisdorf, D. J., & Bloomfield, C. D. (2015). Acute Myeloid Leukemia. *New England Journal of Medicine, 373*(12), 1136-1152. doi:10.1056/NEJMra1406184

Escribano-Diaz, C., Orthwein, A., Fradet-Turcotte, A., Xing, M., Young, J. T., Tkac, J., . . . Durocher, D. (2013). A cell cycle-dependent regulatory circuit composed of 53BP1-RIF1 and BRCA1-CtIP controls DNA repair pathway choice. *Molecular Cell, 49*(5), 872-883. doi:10.1016/j.molcel.2013.01.001

Esposito, M. T., Zhao, L., Fung, T. K., Rane, J. K., Wilson, A., Martin, N., . . . So, C. W. (2015). Synthetic lethal targeting of oncogenic transcription factors in acute leukemia by PARP inhibitors. *Nature Medicine, 21*(12), 1481-1490. doi:10.1038/nm.3993

Fang, J., Ying, H., Mao, T., Fang, Y., Lu, Y., Wang, H., . . . Gu, J. (2017). Upregulation of CD11b and CD86 through LSD1 inhibition promotes myeloid differentiation and suppresses cell proliferation in human monocytic leukemia cells. *Oncotarget, 8*(49), 85085-85101. doi:10.18632/oncotarget.18564

Fang, Y., McGrail, D. J., Sun, C., Labrie, M., Chen, X., Zhang, D., . . . Mills, G. B. (2019). Sequential Therapy with PARP and WEE1 Inhibitors Minimizes Toxicity while Maintaining Efficacy. *Cancer Cell, 35*(6), 851-867 e857. doi:10.1016/j.ccell.2019.05.001

Faraoni, I., Compagnone, M., Lavorgna, S., Angelini, D. F., Cencioni, M. T., Piras, E., . . . Lo-Coco, F. (2015). BRCA1, PARP1 and gammaH2AX in acute myeloid leukemia: Role as biomarkers of response to the PARP inhibitor olaparib. *Biochimica et Biophysica Acta, 1852*(3), 462-472. doi:10.1016/j.bbadis.2014.12.001

Farmer, H., McCabe, N., Lord, C. J., Tutt, A. N., Johnson, D. A., Richardson, T. B., . . . Ashworth, A. (2005). Targeting the DNA repair defect in BRCA mutant cells as a therapeutic strategy. *Nature, 434*(7035), 917-921. doi:10.1038/nature03445

Fraser, C., Ryan, J., & Sarosiek, K. (2019). BH3 Profiling: A Functional Assay to Measure Apoptotic Priming and Dependencies. *Methods in Molecular Biology, 1877*, 61-76. doi:10.1007/978-1-4939-8861-7_4

Frisch, B. J., & Calvi, L. M. (2014). Hematopoietic stem cell cultures and assays. *Methods in Molecular Biology, 1130*, 315-324. doi:10.1007/978-1-62703-989-5_24

Fuss, I. J., Kanof, M. E., Smith, P. D., & Zola, H. (2009). Isolation of whole mononuclear cells from peripheral blood and cord blood. *Current Protocols in Immunology, Chapter 7*, Unit7.1. doi:10.1002/0471142735.im0701s85

Garg, M., Nagata, Y., Kanojia, D., Mayakonda, A., Yoshida, K., Haridas Keloth, S., . . . Koeffler, H. P. (2015). Profiling of somatic mutations in acute myeloid leukemia with FLT3-ITD at diagnosis and relapse. *Blood, 126*(22), 2491-2501. doi:10.1182/blood-2015-05-646240

Ghosal, G., & Chen, J. (2013). DNA damage tolerance: a double-edged sword guarding the genome. *Transl Cancer Res, 2*(3), 107-129. doi:10.3978/j.issn.2218-676X.2013.04.01

Gogola, E., Rottenberg, S., & Jonkers, J. (2019). Resistance to PARP Inhibitors: Lessons from Preclinical Models of BRCA-Associated Cancer. *Annual Review of Cancer Biology, 3*(1), 235-254. doi:10.1146/annurev-cancerbio-030617-050232

Gong, F., Fahy, D., Liu, H., Wang, W., & Smerdon, M. J. (2008). Role of the mammalian SWI/SNF chromatin remodeling complex in the cellular response to UV damage. *Cell cycle (Georgetown, Tex.), 7*(8), 1067-1074. doi:10.4161/cc.7.8.5647

Hanahan, D., & Weinberg, R. A. (2011). Hallmarks of cancer: the next generation. *Cell, 144*(5), 646-674. doi:10.1016/j.cell.2011.02.013

He, L., Kulesskiy, E., Saarela, J., Turunen, L., Wennerberg, K., Aittokallio, T., & Tang, J. (2018). Methods for High-throughput Drug Combination Screening and Synergy Scoring. In L. von Stechow (Ed.), *Cancer Systems Biology: Methods and Protocols* (pp. 351-398). New York, NY: Springer New York.

Hoeijmakers, J. H. (2009). DNA damage, aging, and cancer. *New England Journal of Medicine, 361*(15), 1475-1485. doi:10.1056/NEJMra0804615

Hottiger, M. O., Hassa, P. O., Lüscher, B., Schüler, H., & Koch-Nolte, F. (2010). Toward a unified nomenclature for mammalian ADP-ribosyltransferases. *Trends in Biochemical Sciences, 35*(4), 208-219. doi:10.1016/j.tibs.2009.12.003

Hunt, S. E., McLaren, W., Gil, L., Thormann, A., Schuilenburg, H., Sheppard, D., . . . Cunningham, F. (2018). Ensembl variation resources. *Database, 2018*. doi:10.1093/database/bay119

Ianevski, A., He, L., Aittokallio, T., & Tang, J. (2017). SynergyFinder: a web application for analyzing drug combination dose-response matrix data. *Bioinformatics (Oxford, England), 33*(15), 2413-2415. doi:10.1093/bioinformatics/btx162

Jachimowicz, R. D., Goergens, J., & Reinhardt, H. C. (2019). DNA double-strand break repair pathway choice - from basic biology to clinical exploitation. *Cell cycle (Georgetown, Tex.), 18*(13), 1423-1434. doi:10.1080/15384101.2019.1618542

Jiricny, J. (2006). The multifaceted mismatch-repair system. *Nature Reviews: Molecular Cell Biology, 7*(5), 335-346. doi:10.1038/nrm1907

Jonas, B. A., & Pollyea, D. A. (2019). How we use venetoclax with hypomethylating agents for the treatment of newly diagnosed patients with acute myeloid leukemia. *Leukemia, 33*(12), 2795-2804. doi:10.1038/s41375-019-0612-8

Kim, M. Y., Zhang, T., & Kraus, W. L. (2005). Poly(ADP-ribosyl)ation by PARP-1: 'PAR-laying' NAD+ into a nuclear signal. *Genes and Development, 19*(17), 1951-1967. doi:10.1101/gad.1331805

Konopleva, M., & Letai, A. (2018). BCL-2 inhibition in AML: an unexpected bonus? *Blood, 132*(10), 1007-1012. doi:10.1182/blood-2018-03-828269

Konopleva, M., Pollyea, D. A., Potluri, J., Chyla, B., Hogdal, L., Busman, T., . . . Letai, A. (2016). Efficacy and Biological Correlates of Response in a Phase II Study of Venetoclax Monotherapy in Patients with Acute Myelogenous Leukemia. *Cancer Discovery, 6*(10), 1106-1117. doi:10.1158/2159-8290.CD-16-0313

Kotschy, A., Szlavik, Z., Murray, J., Davidson, J., Maragno, A. L., Le Toumelin-Braizat, G., . . . Geneste, O. (2016). The MCL1 inhibitor S63845 is tolerable and effective in diverse cancer models. *Nature, 538*(7626), 477-482. doi:10.1038/nature19830

Krause, D. S., & Van Etten, R. A. (2007). Right on target: eradicating leukemic stem cells. *Trends in Molecular Medicine, 13*(11), 470-481. doi:10.1016/j.molmed.2007.09.003

Lashgari, A., Fauteux, M., Marechal, A., & Gaudreau, L. (2018). Cellular Depletion of BRD8 Causes p53-Dependent Apoptosis and Induces a DNA Damage Response in Non-Stressed Cells. *Scientific Reports, 8*(1), 14089. doi:10.1038/s41598-018-32323-3

Le Pen, J., Maillet, L., Sarosiek, K., Vuillier, C., Gautier, F., Montessuit, S., . . . Juin, P. P. (2016). Constitutive p53 heightens mitochondrial apoptotic priming and favors cell death induction by BH3 mimetic inhibitors of BCL-xL. *Cell Death & Disease, 7*, e2083. doi:10.1038/cddis.2015.400

Lee, E. K., & Konstantinopoulos, P. A. (2019). Combined PARP and Immune Checkpoint Inhibition in Ovarian Cancer. *Trends Cancer, 5*(9), 524-528. doi:10.1016/j.trecan.2019.06.004

Leverson, J. D., Sampath, D., Souers, A. J., Rosenberg, S. H., Fairbrother, W. J., Amiot, M., . . . Letai, A. (2017). Found in Translation: How Preclinical Research Is Guiding the Clinical Development of the BCL2-Selective Inhibitor Venetoclax. *Cancer Discovery, 7*(12), 1376-1393. doi:10.1158/2159-8290.Cd-17-0797

Li, A., Yi, M., Qin, S., Chu, Q., Luo, S., & Wu, K. (2019). Prospects for combining immune checkpoint blockade with PARP inhibition. *Journal of Hematology & Oncology, 12*(1), 98. doi:10.1186/s13045-019-0784-8

Lin, K. H., Rutter, J. C., Xie, A., Pardieu, B., Winn, E. T., Bello, R. D., . . . Wood, K. C. (2020). Using antagonistic pleiotropy to design a chemotherapy-induced evolutionary trap to target drug resistance in cancer. *Nature Genetics, 52*(4), 408-417. doi:10.1038/s41588-020-0590-9

Livak, K. J., & Schmittgen, T. D. (2001). Analysis of relative gene expression data using real-time quantitative PCR and the 2(-Delta Delta C(T)) Method. *Methods, 25*(4), 402-408. doi:10.1006/meth.2001.1262

Livneh, Z. (2006). Keeping mammalian mutation load in check: regulation of the activity of error-prone DNA polymerases by p53 and p21. *Cell cycle (Georgetown, Tex.), 5*(17), 1918-1922. doi:10.4161/cc.5.17.3193

Loewe, S. (1953). The problem of synergism and antagonism of combined drugs. *Arzneimittel-Forschung, 3*(6), 285-290.

Lord, C. J., & Ashworth, A. (2013). Mechanisms of resistance to therapies targeting BRCA-mutant cancers. *Nature Medicine, 19*(11), 1381-1388. doi:10.1038/nm.3369

Lord, C. J., & Ashworth, A. (2016). BRCAness revisited. *Nature Reviews: Cancer, 16*(2), 110-120. doi:10.1038/nrc.2015.21

Lord, C. J., Tutt, A. N., & Ashworth, A. (2015). Synthetic lethality and cancer therapy: lessons learned from the development of PARP inhibitors. *Annual Review of Medicine, 66*, 455-470. doi:10.1146/annurev-med-050913-022545

Lowenberg, B., & Rowe, J. M. (2016). Introduction to the review series on advances in acute myeloid leukemia (AML). *Blood, 127*(1), 1. doi:10.1182/blood-2015-10-662684

Luo, X., & Kraus, W. L. (2012). On PAR with PARP: cellular stress signaling through poly(ADP-ribose) and PARP-1. *Genes and Development, 26*(5), 417-432. doi:10.1101/gad.183509.111

Maifrede, S., Nieborowska-Skorska, M., Sullivan-Reed, K., Dasgupta, Y., Podszywalow-Bartnicka, P., Le, B. V., . . . Skorski, T. (2018). Tyrosine kinase inhibitor-induced defects in DNA repair sensitize FLT3(ITD)-positive leukemia cells to PARP1 inhibitors. *Blood, 132*(1), 67-77. doi:10.1182/blood-2018-02-834895

Malyutina, A., Majumder, M. M., Wang, W., Pessia, A., Heckman, C. A., & Tang, J. (2019). Drug combination sensitivity scoring facilitates the discovery of synergistic and efficacious drug combinations in cancer. *PLoS Computational Biology, 15*(5), e1006752. doi:10.1371/journal.pcbi.1006752

Mateo, J., Lord, C. J., Serra, V., Tutt, A., Balmaña, J., Castroviejo-Bermejo, M., . . . de Bono, J. S. (2019). A decade of clinical development of PARP inhibitors in perspective. *Annals of Oncology, 30*(9), 1437-1447. doi:10.1093/annonc/mdz192

Maya-Mendoza, A., Moudry, P., Merchut-Maya, J. M., Lee, M., Strauss, R., & Bartek, J. (2018). High speed of fork progression induces DNA replication stress and genomic instability. *Nature, 559*(7713), 279-284. doi:10.1038/s41586-018-0261-5

Maynard, S., Schurman, S. H., Harboe, C., de Souza-Pinto, N. C., & Bohr, V. A. (2009). Base excision repair of oxidative DNA damage and association with cancer and aging. *Carcinogenesis, 30*(1), 2-10. doi:10.1093/carcin/bgn250

Michelena, J., & Altmeyer, M. (2017). Cell Cycle Resolved Measurements of Poly(ADP-Ribose) Formation and DNA Damage Signaling by Quantitative Image-Based Cytometry. *Methods in Molecular Biology, 1608*, 57-68. doi:10.1007/978-1-4939-6993-7_5

Michelena, J., Lezaja, A., Teloni, F., Schmid, T., Imhof, R., & Altmeyer, M. (2018). Analysis of PARP inhibitor toxicity by multidimensional fluorescence microscopy reveals

mechanisms of sensitivity and resistance. *Nat Commun, 9*(1), 2678. doi:10.1038/s41467-018-05031-9

Moison, C., Lavallée, V. P., Thiollier, C., Lehnertz, B., Boivin, I., Mayotte, N., . . . Sauvageau, G. (2019). Complex karyotype AML displays G2/M signature and hypersensitivity to PLK1 inhibition. *Blood Adv, 3*(4), 552-563. doi:10.1182/bloodadvances.2018028480

Montero, J., & Letai, A. (2018). Why do BCL-2 inhibitors work and where should we use them in the clinic? *Cell Death and Differentiation, 25*(1), 56-64. doi:10.1038/cdd.2017.183

Muvarak, N. E., Chowdhury, K., Xia, L., Robert, C., Choi, E. Y., Cai, Y., . . . Rassool, F. V. (2016). Enhancing the Cytotoxic Effects of PARP Inhibitors with DNA Demethylating Agents - A Potential Therapy for Cancer. *Cancer Cell, 30*(4), 637-650. doi:10.1016/j.ccell.2016.09.002

O'Connor, M. J. (2015). Targeting the DNA Damage Response in Cancer. *Molecular Cell, 60*(4), 547-560. doi:10.1016/j.molcel.2015.10.040

Pabst, C., Krosl, J., Fares, I., Boucher, G., Ruel, R., Marinier, A., . . . Sauvageau, G. (2014). Identification of small molecules that support human leukemia stem cell activity ex vivo. *Nat Methods, 11*(4), 436-442. doi:10.1038/nmeth.2847

Pan, R., Hogdal, L. J., Benito, J. M., Bucci, D., Han, L., Borthakur, G., . . . Letai, A. G. (2014). Selective BCL-2 inhibition by ABT-199 causes on-target cell death in acute myeloid leukemia. *Cancer Discovery, 4*(3), 362-375. doi:10.1158/2159-8290.CD-13-0609

Pan, R., Ruvolo, V., Mu, H., Leverson, J. D., Nichols, G., Reed, J. C., . . . Andreeff, M. (2017). Synthetic Lethality of Combined Bcl-2 Inhibition and p53 Activation in AML: Mechanisms and Superior Antileukemic Efficacy. *Cancer Cell, 32*(6), 748-760 e746. doi:10.1016/j.ccell.2017.11.003

Pant, S., Maitra, A., & Yap, T. A. (2019). PARP inhibition - opportunities in pancreatic cancer. *Nature Reviews: Clinical Oncology, 16*(10), 595-596. doi:10.1038/s41571-019-0257-6

Papaemmanuil, E., Gerstung, M., Bullinger, L., Gaidzik, V. I., Paschka, P., Roberts, N. D., . . . Campbell, P. J. (2016). Genomic Classification and Prognosis in Acute Myeloid Leukemia. *New England Journal of Medicine, 374*(23), 2209-2221. doi:10.1056/NEJMoa1516192

Pelayo, R., Dorantes-Acosta, E., Vadillo, E., & Fuentes-P, E. (2012). From HSC to B-Lymphoid Cells in Normal and Malignant Hematopoiesis. In *Advances in Hematopoietic Stem Cell Research*.

Pentimalli, F. (2017). BCL2: a 30-year tale of life, death and much more to come. *Cell Death and Differentiation, 25*(1), 7-9. doi:10.1038/cdd.2017.189

Pinho, S., & Frenette, P. S. (2019). Haematopoietic stem cell activity and interactions with the niche. *Nature Reviews: Molecular Cell Biology, 20*(5), 303-320. doi:10.1038/s41580-019-0103-9

Polo, S. E., & Jackson, S. P. (2011). Dynamics of DNA damage response proteins at DNA breaks: a focus on protein modifications. *Genes and Development, 25*(5), 409-433. doi:10.1101/gad.2021311

Prabst, K., Engelhardt, H., Ringgeler, S., & Hubner, H. (2017). Basic Colorimetric Proliferation Assays: MTT, WST, and Resazurin. *Methods in Molecular Biology, 1601*, 1-17. doi:10.1007/978-1-4939-6960-9_1

Prokocimer, M., Molchadsky, A., & Rotter, V. (2017). Dysfunctional diversity of p53 proteins in adult acute myeloid leukemia: projections on diagnostic workup and therapy. *Blood, 130*(6), 699-712. doi:10.1182/blood-2017-02-763086

Pullarkat, V. A., & Newman, E. M. (2016). BCL2 Inhibition by Venetoclax: Targeting the Achilles' Heel of the Acute Myeloid Leukemia Stem Cell? *Cancer Discovery, 6*(10), 1082-1083. doi:10.1158/2159-8290.CD-16-0921

Radha, G., & Raghavan, S. C. (2017). BCL2: A promising cancer therapeutic target. *Biochim Biophys Acta Rev Cancer, 1868*(1), 309-314. doi:10.1016/j.bbcan.2017.06.004

Rasmussen, R. D., Gajjar, M. K., Tuckova, L., Jensen, K. E., Maya-Mendoza, A., Holst, C. B., . . . Hamerlik, P. (2016). BRCA1-regulated RRM2 expression protects glioblastoma cells from endogenous replication stress and promotes tumorigenicity. *Nat Commun, 7*, 13398. doi:10.1038/ncomms13398

Ray Chaudhuri, A., & Nussenzweig, A. (2017). The multifaceted roles of PARP1 in DNA repair and chromatin remodelling. *Nature Reviews: Molecular Cell Biology, 18*(10), 610-621. doi:10.1038/nrm.2017.53

Reed, J. C. (2017). Bcl-2 on the brink of breakthroughs in cancer treatment. *Cell Death and Differentiation, 25*(1), 3-6. doi:10.1038/cdd.2017.188

Roberts, A. W., Davids, M. S., Pagel, J. M., Kahl, B. S., Puvvada, S. D., Gerecitano, J. F., . . . Seymour, J. F. (2016). Targeting BCL2 with Venetoclax in Relapsed Chronic Lymphocytic Leukemia. *New England Journal of Medicine, 374*(4), 311-322. doi:10.1056/NEJMoa1513257

Roos, W. P., Thomas, A. D., & Kaina, B. (2016). DNA damage and the balance between survival and death in cancer biology. *Nature Reviews: Cancer, 16*(1), 20-33. doi:10.1038/nrc.2015.2

Roukos, V., Pegoraro, G., Voss, T. C., & Misteli, T. (2015). Cell cycle staging of individual cells by fluorescence microscopy. *Nature Protocols, 10*(2), 334-348. doi:10.1038/nprot.2015.016

Ryan, J., & Letai, A. (2013). BH3 profiling in whole cells by fluorimeter or FACS. *Methods, 61*(2), 156-164. doi:10.1016/j.ymeth.2013.04.006

Sachdev, E., Tabatabai, R., Roy, V., Rimel, B. J., & Mita, M. M. (2019). PARP Inhibition in Cancer: An Update on Clinical Development. *Targeted Oncology, 14*(6), 657-679. doi:10.1007/s11523-019-00680-2

Scardocci, A., Guidi, F., D'Alo, F., Gumiero, D., Fabiani, E., Diruscio, A., . . . Voso, M. T. (2006). Reduced BRCA1 expression due to promoter hypermethylation in therapy-related acute myeloid leukaemia. *British Journal of Cancer, 95*(8), 1108-1113. doi:10.1038/sj.bjc.6603392

Schindelin, J., Arganda-Carreras, I., Frise, E., Kaynig, V., Longair, M., Pietzsch, T., . . . Cardona, A. (2012). Fiji: an open-source platform for biological-image analysis. *Nature Methods, 9*(7), 676-682. doi:10.1038/nmeth.2019

Schmid, C., Labopin, M., Socie, G., Daguindau, E., Volin, L., Huynh, A., . . . Bone Marrow, T. (2015). Outcome of patients with distinct molecular genotypes and cytogenetically normal AML after allogeneic transplantation. *Blood, 126*(17), 2062-2069. doi:10.1182/blood-2015-06-651562

Severson, T. M., Wolf, D. M., Yau, C., Peeters, J., Wehkam, D., Schouten, P. C., . . . van 't Veer, L. (2017). The BRCA1ness signature is associated significantly with response to PARP inhibitor treatment versus control in the I-SPY 2 randomized neoadjuvant setting. *Breast Cancer Research, 19*(1), 99. doi:10.1186/s13058-017-0861-2

Shen, Y., Aoyagi-Scharber, M., & Wang, B. (2015). Trapping Poly(ADP-Ribose) Polymerase. *Journal of Pharmacology and Experimental Therapeutics, 353*(3), 446-457. doi:10.1124/jpet.114.222448

Sheng, C., Mendler, I. H., Rieke, S., Snyder, P., Jentsch, M., Friedrich, D., . . . Loewer, A. (2019). PCNA-Mediated Degradation of p21 Coordinates the DNA Damage Response and Cell Cycle Regulation in Individual Cells. *Cell Reports, 27*(1), 48-58 e47. doi:10.1016/j.celrep.2019.03.031

Shouval, R., Labopin, M., Bomze, D., Baerlocher, G. M., Capria, S., Blaise, D., . . . Nagler, A. (2020). Risk stratification using FLT3 and NPM1 in acute myeloid leukemia patients autografted in first complete remission. *Bone Marrow Transplantation*. doi:10.1038/s41409-020-0936-z

Singh, H. R., Nardozza, A. P., Moller, I. R., Knobloch, G., Kistemaker, H. A. V., Hassler, M., . . . Ladurner, A. G. (2017). A Poly-ADP-Ribose Trigger Releases the Auto-Inhibition of a Chromatin Remodeling Oncogene. *Molecular Cell, 68*(5), 860-871 e867. doi:10.1016/j.molcel.2017.11.019

Singh, R., Letai, A., & Sarosiek, K. (2019). Regulation of apoptosis in health and disease: the balancing act of BCL-2 family proteins. *Nature Reviews: Molecular Cell Biology, 20*(3), 175-193. doi:10.1038/s41580-018-0089-8

Stein, E. M., & Tallman, M. S. (2016). Emerging therapeutic drugs for AML. *Blood, 127*(1), 71-78. doi:10.1182/blood-2015-07-604538

Swindall, A. F., Stanley, J. A., & Yang, E. S. (2013). PARP-1: Friend or Foe of DNA Damage and Repair in Tumorigenesis? *Cancers, 5*(3), 943-958. doi:10.3390/cancers5030943

Tate, J. G., Bamford, S., Jubb, H. C., Sondka, Z., Beare, D. M., Bindal, N., . . . Forbes, S. A. (2019). COSMIC: the Catalogue Of Somatic Mutations In Cancer. *Nucleic Acids Research, 47*(D1), D941-d947. doi:10.1093/nar/gky1015

Tyner, J. W., Tognon, C. E., Bottomly, D., Wilmot, B., Kurtz, S. E., Savage, S. L., . . . Druker, B. J. (2018). Functional genomic landscape of acute myeloid leukaemia. *Nature, 562*(7728), 526-531. doi:10.1038/s41586-018-0623-z

Vega-Avila, E., & Pugsley, M. K. (2011). An overview of colorimetric assay methods used to assess survival or proliferation of mammalian cells. *Proceedings of the Western Pharmacology Society, 54*, 10-14.

Wood, R. D., Mitchell, M., & Lindahl, T. (2005). Human DNA repair genes, 2005. *Mutation Research, 577*(1-2), 275-283. doi:10.1016/j.mrfmmm.2005.03.007

Ye, J., Coulouris, G., Zaretskaya, I., Cutcutache, I., Rozen, S., & Madden, T. L. (2012). Primer-BLAST: a tool to design target-specific primers for polymerase chain reaction. *BMC Bioinformatics, 13*, 134. doi:10.1186/1471-2105-13-134